Electrochemical and Magnetochemical Approaches for Neuronal Modulation

by

Jimin Park

B.S.,Materials Science and Engineering, Seoul National University, 2012
M.S.,Materials Science and Engineering, Seoul National University, 2014

Submitted to the Department of Materials Science and Engineering
in partial fulfillment of the requirements for the degree of

Ph. D. in Materials Science and Engineering

at the

MASSACHUSETTS INSTITUTE OF TECHNOLOGY

February 2022

Author .....
Department of Materials Science and Engineering
January 9, 2022

Certified by .....
Polina Anikeeva
Professor of Materials Science and Engineering
Thesis Supervisor

Accepted by .....
Frances M. Ross
Professor of Materials Science and Engineering
Chair, Departmental Committee on Graduate Studies

Electrochemical and Magnetochemical Approaches for Neuronal Modulation

by

Jimin Park

Submitted to the Department of Materials Science and Engineering
on January 9, 2022, in partial fulfillment of the
requirements for the degree of
Ph. D. in Materials Science and Engineering

Abstract

The development of tools to deliver chemical signals to specific neurons can enhance our understanding of chemical signaling in the nervous system and enable chemical therapies for neurological disorders. Existing technologies for chemical neuromodulation, including intracranial injection of chemicals through an implanted cannula, 1) do not apply in the case of transient and unstable chemical species and 2) require tethering of animal subjects to external hardware, which can limit the study of freely-behaving subjects. By employing nanomaterials chemistry, electrochemistry, and magnetism, this thesis seeks to develop in vivo chemical delivery systems with unprecedented capabilities. First, we design an electrochemical strategy that enables in situ synthesis and delivery of unstable chemical signals to targeted neuronal circuits with nanoscale electrocatalysts, biocompatible precursors, and electric fields. This electrochemical system is implemented in an implantable probe allowing for the investigation of neurophysiological processes mediated by unstable chemical species, such as nitric oxide and carbon monoxide, in the mouse brain. The second focus of this thesis is to design a magnetochemical system for wireless delivery and control of chemical signals without tethered hardware. By designing nanotransducers or molecular radicals capable of converting non-invasive magnetic field stimuli into chemical signals, such as protons and flavin cofactors, we remotely modulate activity of specific neurons and chemical signal-mediated behaviors in the mouse.

Thesis Supervisor: Polina Anikeeva
Title: Professor of Materials Science and Engineering

Acknowledgments

First I would like to express my deepest gratitude to my trusted advisor, Professor Polina Anikeeva. I appreciate you for your support, guidance, and encouragement throughout my Ph.D program at MIT. Your enthusiasm for research and open-mindness in scientific attitude have motivated me to develop my career in academia and will continue to inspire me during my upcoming journey. It has been a great pleasure to work with you on unusual and wild projects.

I owe special thanks to my committee members, Professor Yet-Ming Chiang, Professor Caroline A. Ross, and Professor Karthish Manthiram, who have guided and inspired me with valuable feedback and critical advice. They generously offered their resources and insight to help me solidify my scientific ideas. I would not be able to complete this degree without their support. In addition to my Ph.D advisor and committee members, I would like to give my gratitude to my previous advisors and mentors in South Korea, Professor Ki Tae Nam and Professor Kisuk Kang, and Professor Seungwu Han at Seoul National University (SNU). Thank you for introducing me to the world of materials science and engineering and giving me endless support in my personal and academic careers. I would also like to convey thanks to my wonderful team members (Dr. Hyun-Kwang Seok, Dr. Yu-Chan Kim, Dr. Hojeong Jeon, Dr. Myoung-Ryul Ok, Dr. Hyung-Seop Han) at Korea Institute of Science and Technology (KIST) for their assistance and support. I have experienced a lot of personal growth during my time in KIST.

I appreciate all members of the Bioelectronics group for their help. Thank you to Professor Po-Han Chiang and Professor Seongjun Park for teaching me how to approach neuroscience problems and perform biological experiments. I also want to thank Florian Koehler and Atharva Sahasrabudhe, who have worked closely with me on multiple projects and have emotionally supported me a lot during my Ph.D. Thank you to Professor Dekel Rosenfeld, Professor Siyuan Rao, Dr. Tomo Tanaka, Dr. Marc-Joseph Antonini, Georgios Varnavides, and Anthony Tabet, whose contributions to immunohistochemistry, device fabrication, and modeling, were foundational to this

thesis work. I really appreciate Florian Koehler and Hannah Field for giving valulable comments on this thesis and their friendship. Thank you to Dr. Jungsang Moon, Youngbin Lee, and Keisuke Nagao for being great collaborators and friends of mine. In addition, I thank all the group members and talented undergraduates for their assistance and fruitful discussions on this work: Dr. Marie Manthey, Dr. Noah Kent, Indie Garwood, Juliette Alain, Karen Pang, Rajib Mondal, Yeji Kim, Rebecca Gillette, Cindy Higgins, Alicia Yang, and Shauna Kwag.

This work would not have been possible without the help of many collaborators. I want to thank Professor Kyoungsuk Jin, who has taught me a lot since I was a very young researcher at SNU. It was a great pleasure to work with you at MIT and SNU. Thanks to Joseph H. Maalouf, Joy S. Zeng, Zachary J. Schiffer, Professor Yoel Fink, Professor Ofer Yizhar, and Professor Karthish Manthiram for their experct help and adivce on this work.

It has been a pleasant journey in the past four and half years. I am thankful to all members of the Korean Graduate Student Association in Materials Science and Engineering (KGMSE) and all friends I shared this time at MIT with. Especially, I would like to thank Iksung Kang, Donghwan Kim, Ukjin Kwon, Soonhyoung Kwon, Seo Woo Choi, So-Yoon Yang, Heejung Kim, Rafy Choi, Dongha Kim, Jiyun Kang, Andrew Song, and Jungmoon Ham for their emotional support and the guidance for my career.

I dedicate my thesis work to my parents, Song Park and Jangwon Suh, who have made me into the person I am today. I sincerely appreciate you for your fundamental support, endless dedication, and encouragement on my journey. Finally, I would like to thank to my sister, Seon Yeong Park, brother-in-law, Hyung Jin Ju, and lovely nephews Ejun Ju and Jaeho Ju for their love and support. I sincerely hope that our family is always happy and fulfilled.

Contents

List of Figures

Chapter 1

Introduction

1.1 Chemical Signaling in the Nervous System

Cells communicate by transmitting, receiving, and processing chemical signals produced by themselves or their surrounding environment. Chemical signals, referred to as ligands, bind to the receptors, which are located in the extracellular or intracellular space, altering the conformation of the receptors. These structural changes upon binding of ligands affect enzymatic or ion channel activities of the receptors and other proteins linked to the receptors. The chemical signal is then transmitted through a chain of molecular events inside a cell (signaling pathway), ultimately causing cellular responses including regulation of gene activities or modulation of metabolism [1].

Based on the distance of cell signaling, chemical signaling can be categorized as autocrine, paracrine, or endocrine. Autocrine signaling is the process where a cell releases ligands that bind to its own receptors, resulting in the alteration of its cellular functions. In the case of paracrine signaling, the behaviour of cells is altered in response to the ligands produced by neighboring cells. Generally, ligands involved in paracrine signaling travel short distances through diffusion processes. Ligands involved in endocrine signaling, referred to as endocrine signals or hormones, affect cells located at significantly larger distances from endocrine cells through the circulatory system (Figure 1-1) [1].

In the nervous system, chemical signals, generally referred to as neurotransmitters,

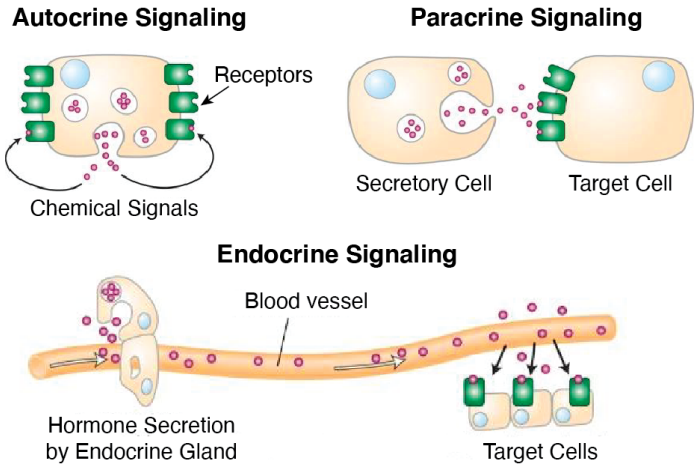

Figure 1-1: **Schematics illustrating various types of chemical signaling** Reprinted from [1].

are transmitted from the presynaptic neuron into the synaptic cleft, the gap between a presynaptic neuron and a postsynaptic cell. These chemical signals then bind to receptors on the postsynaptic target cells, such as postsynaptic neurons, gland cells, and muscle cells (Figure 1-2) [1, 2]. This process is called neurotransmission or synaptic signaling, one of the representative examples of paracrine signaling [1]. In humans, over 500 types of chemical signals (neurotransmitters) ranging from gaseous molecules (NO, CO, etc.) to monoamines (dopamine, serotonin, etc.) to peptides (oxytocin, opioid peptides, etc.) have been identified [3–5].

One of the direct actions of neurotransmitters is to change the ion permeability and membrane potential of the postsynaptic target cells. In this way, neurotransmitters can either excite or inhibit postsynaptic cells by triggering or inhibiting the formation of action potentials (nerve impulses). For example, when neurotransmitters bind to the excitatory receptors of postsynpatic target cells, Na^+ or Ca^{2+} influxes through ion channels results in depolarization of postsynaptic membranes and generation of action potentials. The generated action potentials propagate towards the axon terminals of postsyanptic neurons, causing the release of neurotransmitters into the synaptic cleft [6]. Glutamate is an example of an excitatory neurotransmitter in the central nervous system is glutamate [7]. Glutamate released from the presynaptic neuron activates glutamate receptors, such as N-methyl-D-aspartate receptor (NDMA) and

α-amino-3-hydroxy-5-methyl-4- isoxazole propionic acid (AMPA) receptors on the postsynpatic neurons. Upon binding of the glutamate, cations (Na^+ or Ca^{2+}) flow through these receptors having ion channels into the postsynaptic neuron, inducing new action potentials to fire. On the other hand, when neurotransmitters bind to inhibitory receptors of target cells, membrane hyperpolarization occurs through Cl^- influx and K^+ efflux, inhibiting the formation of action potentials in postsynaptic cells. Gamma-aminobutyric acid (GABA) is a well-characterized inhibitory neurotransmitter in the nervous system. Generally, GABA binds to the $GABA_A$ receptors, Cl^--selective ion channels, and induces Cl^- entry into neurons [8].

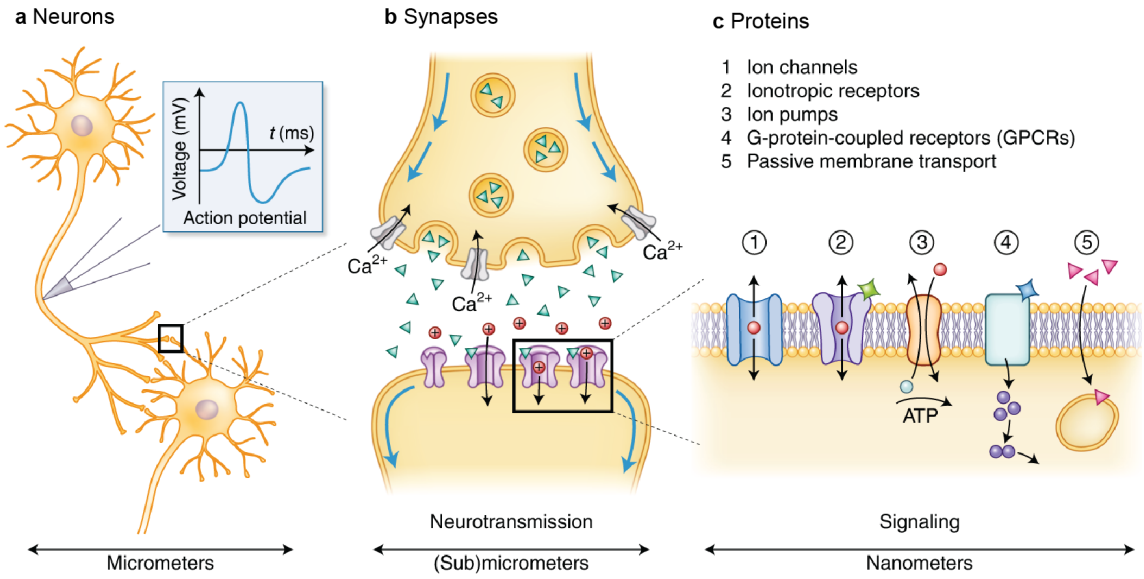

Figure 1-2: **Chemical Signaling through the synaptic cleft** a, Communications of Neurons through chemical signals. Action Potentials induce the release of the chemical signals at the synapses. b, Neurotransmitters released from the presynpatic neuron bind receptors expressed on the postsynaptic cell through the synaptic cleft. c, Representative examples of membrane receptors during chemical signaling. Reprinted from [2].

1.2 Importance of Delivering Chemical Signals in the Nervous System

By influencing the electrical excitability of target cells, neurotransmitters ultimately affect diverse physiological events related to their target cells in the nervous system. One of the representative physiological events influenced by neurotransmitters is synaptic plasticity, which has been proposed as the origin of memory and learning abilities in the mammalian brain. Synaptic plasticity is the ability of preexisting synapses to modify the strength of their synaptic signaling over time. For example, when glutamate binds to NMDA and AMPA receptors in postsynaptic neurons, strong neuronal depolarization displaces NMDA receptor-blocking Mg^{2+}, allowing Ca^{2+} entry inside the postsynaptic neurons (Figure 1-3a). Increase in the intracellular Ca^{2+} concentration induces the activation of Ca^{2+}-dependent signaling cascades, including calcium/calmodulin (CaM)-dependent protein kinase II (CaMKII). Activation of CaMKII results in 1) phosphorylation of AMPA receptors enhancing the permeability of these ion channels, 2) recruitment of AMPA receptors into the membranes of postsynaptic neurons, thereby strengthening synaptic signaling (Figure 1-3b) [9]. NO also affects synaptic plasticity as a retrograde messenger. Whereas glutamate is released from the presynaptic neuron, NO is produced by the postsynaptic neuron and diffuses towards presynaptic terminals. Ca^{2+} influx via NMDA receptor causes NO synthase to produce NO inside the postsynaptic neuron. The generated NO binds to the NO receptor, a soluble guanylate cyclase, in the presynaptic neuron through a diffusion process. Once soluble guanylate cyclase is activated by NO, a second messenger molecule, cGMP, is accumulated, ultimately changing the glutamate release rate from the presynaptic neuron and the strength of synaptic plasticity (Figure 1-4) [10].

Furthermore, neurotransmitters play a crucial role in pathological phenomena in the nervous system. For example, Parkinson's disease, a neurodegenerative disorder affecting the motor system, is related to the destruction of dopamine-releasing neurons in the basal ganglia. Dopamine depletion results in an imbalance between the

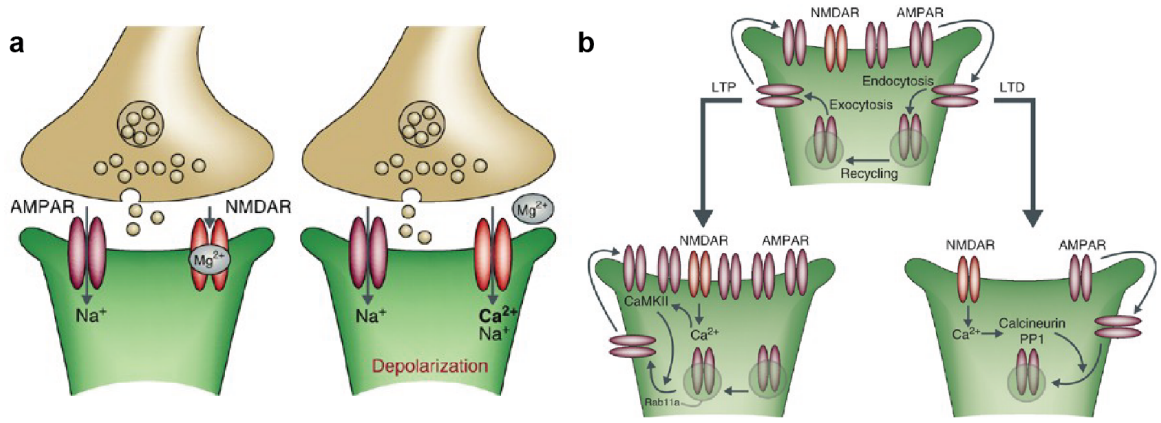

Figure 1-3: **Schematics illustrating synaptic plasticity mediated by neurotransmitters** a, A schematic illustrating the synaptic plasticity at excitatory synapses. Glutamate released from postsynaptic neuron binds to AMPA and NMDA receptors. Depolarization of the postsynaptic cell induces the removal of Mg^{2+} ions blocking the NMDA ion channel, allowing Ca^{2+} influxes into the cell. b,Long-term potentiation (LTP) and long-term depression (LTD) processes driven by Ca^{2+} - CaMKII mediated signaling. In the case of LTP, Ca^{2+} responses result in the enhancement of receptor exocytosis. Reprinted from [9]

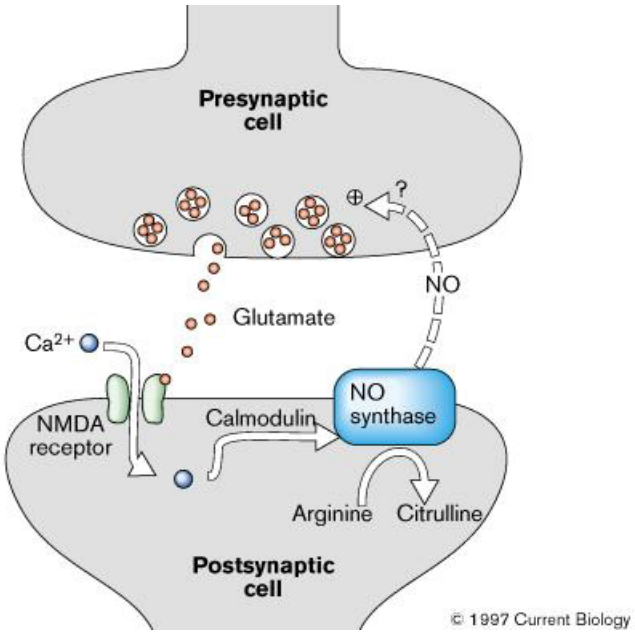

Figure 1-4: **An illustration describing the role of NO as a retrograde messenger in long-term potentiation** Reprinted from [10].

direct and indirect projection systems of the striatum, ultimately giving rise to the movement disorder (Figure 1-5) [4, 11]. As another example, previous studies have found that depression could be related to low levels of serotonin caused by the depletion of serotonin precursor, reabsorption of the released serotonin, and enhanced

activity of monoamine oxidase degrading the serotonin [12].

Together, chemical signals affect numerous physiological and pathological processes in the nervous system. In this way, delivery or control of chemical signals in targeted regions 1) allows mechanistic studies of chemical signaling and 2) enables chemical therapies for several neurological diseases and disorders. For example, by delivering gaseous molecules, NO and CO, to hippocampal slices in vitro, studies have found these molecules to play an important role in the long-term synaptic enhancement of this brain region [3]. As another example, based on findings that depletion of serotonin and norepinepherine neurotransmitter can be related to depression, numerous antidepressants have been developed to restore the levels of these neurotransmitters by modulating their diverse biochemical pathways, such as re-absorption of these molecules into the presynaptic cell or activation of receptors acting on these molecules [13].

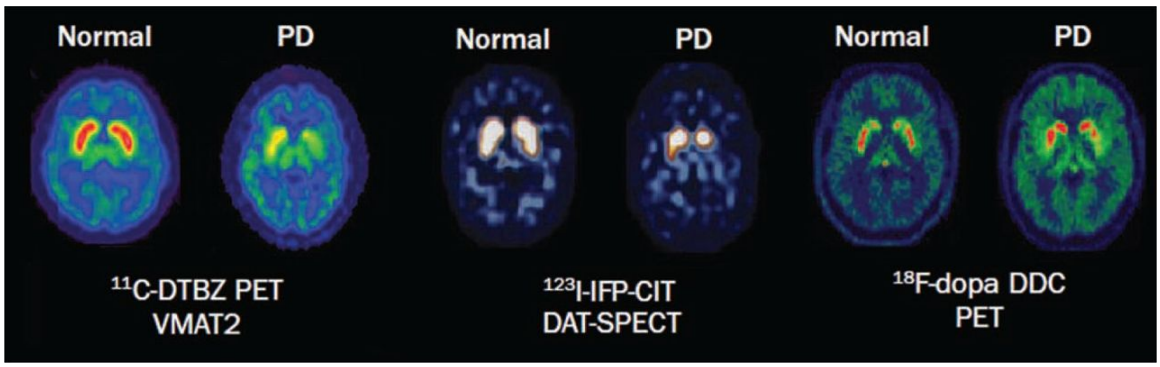

Figure 1-5: **Dysfunction of dopaminergic system in Parkinson's disease** Positron emission tomography and single photon emission computed tomography images showed decreased activity of dopamine (VMAT2: type2 vesicular monoamine transporter, DAT : dopamine transporter, and DDC: dopa decarboxylase) in Parkinson's disease patients. Reprinted from [11].

1.3 Current Tools for Delivering Chemical Signals and Their Limitations

Not surprisingly, numerous technologies for delivering chemical signals to the nervous system have been developed. Generally, the ways to deliver chemical signals in the nervous system, especially in the brain, can be categorized into 1) invasive methods and 2) non-invasive methods [14].

Invasive methods can be further grouped into intracranial injection and intrathecal administration. Intracranial injection is one of the most extensively used methods in neuroscience studies. During intracranial injection, chemical signals are directly infused into targeted brain regions through a permanently implanted cannula or a syringe with relatively high spatial resolution (Figure 1-6) [15]. To further increase the spatial resolution of chemical delivery, recent studies have applied microfluidic channels ($<$100 μm) instead of cannula or syringes (Figure 1-7). The fluid inside the reservoirs can be precisely delivered through these microfluidic channels by external stimuli [16,17]. However, this method relies on invasive surgery (craniotomy), in which a small piece of skull is removed to directly infuse chemicals, causing side-effects such as immune responses or damage to normal brain tissue and blood vessels. Furthermore, tethered hardware, such as a permanently implanted cannula or microfluidic channel, limits the study of freely moving subjects. In addition, this method is not applicable to the delivery of unstable or transient chemical signals, such as gaseous neurotransmitters, due to the degradation of these molecules during delivery. Compared to intracranial injection, intrathecal administration is a less-invasive method, since chemical signals are delivered through the spinal canal without the need to remove the skull. Once injected through the spinal canal, chemicals can flow into the cerebrospinal fluid and then diffuse into the brain [18]. However, this method has relatively poor spatial resolution, causing off-target release of chemical signals.

To avoid invasive surgery, previous studies have designed non-invasive platforms based on nanotechnology [14]. However, the main issue for non-invasive delivery is to deliver chemicals beyond the blood-brain-barrier (BBB), a multicellular interface that

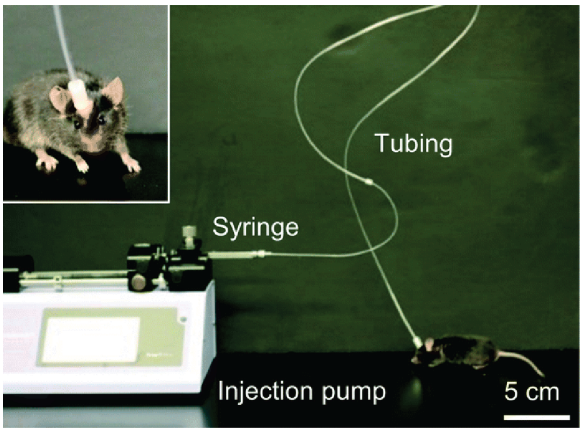

Figure 1-6: **Conventional intracranial injection method for chemical delivery** A photo showing the conventional intracranial injection method with permanently implanted cannula. The mouse connected to the conventional intracranial injection system (inset). Reprinted from [15].

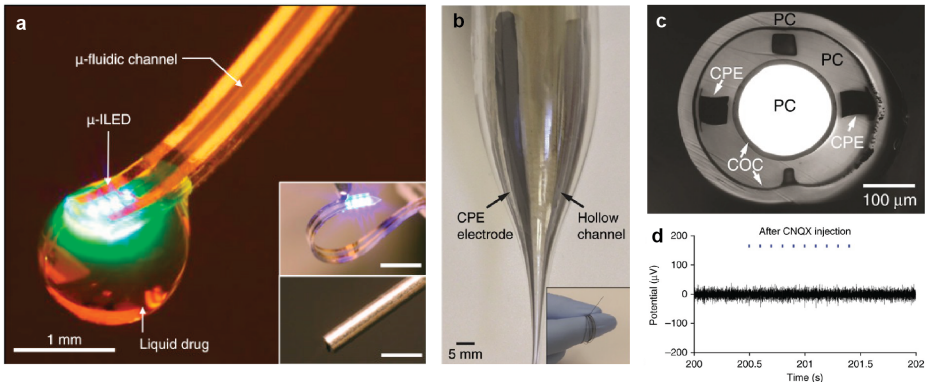

Figure 1-7: **Chemical delivery through soft, microfluidic probes** a, A photo showing the drug delivery through a soft microfluidic probe. b, A photograph of the preform for the fabrication of the neural probe with microfluidic channels. c, A cross-sectional image of the neural probe with microfluidic channels (PC: polycarbonate, COC: cyclic olefin copolymer, CPE : conductive polyethylene). d, Diminished neural activities after delivering CNQX (AMPA receptor antagonist) through the microfluidic channel. Reprinted from [16, 17].

controls the passage of nutrients from the vasculature to the cerebrospinal fluid and also prevents the passage of toxic molecules. To overcome this challenge, prior studies functionalized nanoscale carriers with cationic molecules binding to the negatively-charged molecules on BBB cells, brain permeability enhancers transiently loosening the BBB, and ligands that bind to receptors expressed on the BBB cells (Figure 1-8). As another option, coupled with focused ultrasound, which can transiently open the BBB, microbubbles have been shown to allow chemical delivery beyond the

BBB. Despite these recent advances, the BBB has remained a main hurdle for the development of non-invasive delivery platforms [14, 19]. Furthermore, since chemical signals are generally delivered to brain tissue through diffusion process after crossing the BBB, these methods have limited spatial resolution compared to intracranial injection.

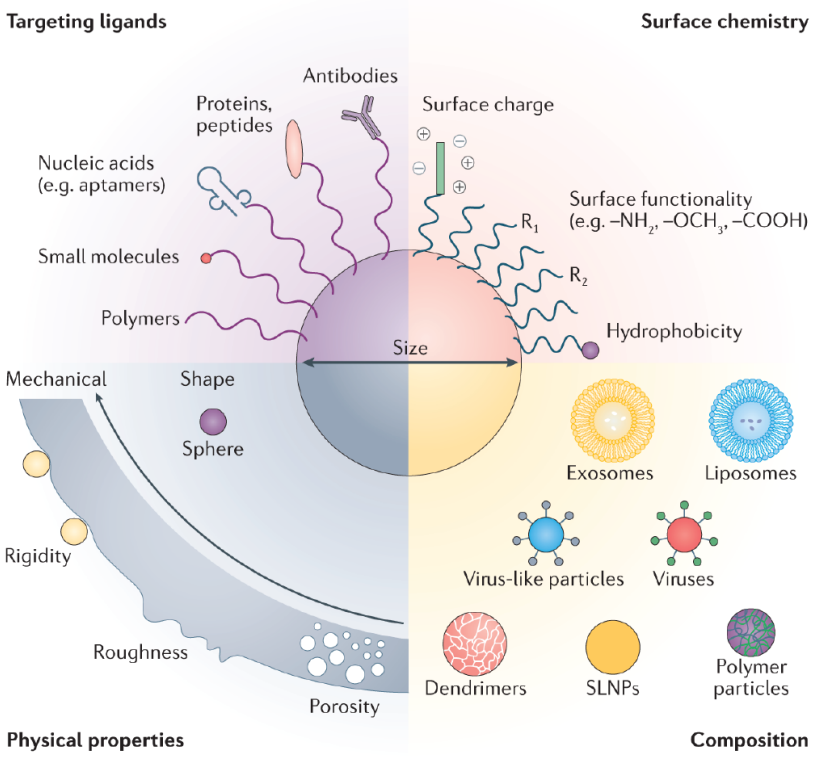

Figure 1-8: **Non-invasive, nanoscale chemical delivery platforms** Strategies for nanoscale chemical delivery systems to increase targeting of the BBB. Reprinted from [14].

1.4 Thesis Structure

With the goal of understanding chemical signal transduction in the nervous system, this thesis focuses on the development of new methodologies for delivering chemical signals to targeted cells. By combining nanomaterials chemistry, electrochemistry, and magnetism, we design new electrochemical (Chapter 2-3) and magnetochemical (Chapter 4-5) approaches for on-demand synthesis of diverse chemical signals and demonstrate their utility for chemical neuromodulation.

In Chapter 2, we present an approach to electrochemically synthesize and deliver a gaseous signaling molecule, NO, which has been difficult to study with conventional, chemical delivery method due to its transient nature. By employing biocompatible NO precursors, nanocatalysts, and modest electric fields, NO can be generated in a spatiotemporally controlled manner, enabling mechanistic studies of NO-mediated neuronal signaling in vitro and in the mouse brain. In Chapter 3, we generalize this electrochemical approach for on-demand generation of other gaseous signaling molecules. Through the rational design of precursors and nanocatalysts, this electrochemical approach allows in situ generation of CO, an important neurobiological messenger molecule, at the microscale.

In Chapter 4-5, we design magnetochemical methodologies to remotely produce chemical signals without the use of tethered hardwares, which have limited the study of live subjects during conventional chemical delivery to subjects. In Chapter 4, we design nanotransducers capable of converting non-invasive magnetic fields into protons by integrating ferrite nanoparticles with polymeric scaffolds. Under magnetic fields, heat dissipated by ferrite nanoparticles through a magnetothermal effect accelerates the hydrolysis of surrounding polymeric scaffolds, resulting in the release of acidic hydrolysis products into the extracellular space. This enables remotely controlled modulation of acid-sensing neurons and acid-related behaviors in mice. In Chapter 5, we explore the potential ability of magnetic fields to remotely control reaction chemistry of redox cofactor solutions by influencing its spin symmetry.

In Chapter 6, we summarize these findings and provide an outlook.

Chapter 2

In Situ Electrochemical Generation of Nitric Oxide (NO) for Neuronal Modulation

2.1 Summary

This Chapter is based on J. Park et al., *Nat. Nanotechnol.*, 2020 [20].

Understanding the function of NO, a lipophilic messenger in physiological processes across nervous, cardiovascular, and immune systems, is currently impeded by the dearth of tools to deliver this gaseous molecule in situ to specific cells. To address this need, we developed iron sulfide nanoclusters that catalyse NO generation from benign sodium nitrite in the presence of modest electric fields. Locally generated NO activates the NO-sensitive cation channel, transient receptor potential vanilloid family member 1 (TRPV1), and latency of TRPV1-mediated Ca^{2+} responses can be controlled by varying the applied voltage. Integrating these electrocatalytic nanoclusters with multimaterial fibers allows NO-mediated neuronal interrogation in vivo. In situ generation of NO within the ventral tegmental area via the electrocatalytic fibers evoked neuronal excitation in the targeted brain region and its excitatory projections

(Figure 2-1). This NO generation platform may advance mechanistic studies of the role of NO in the nervous system and other organs.

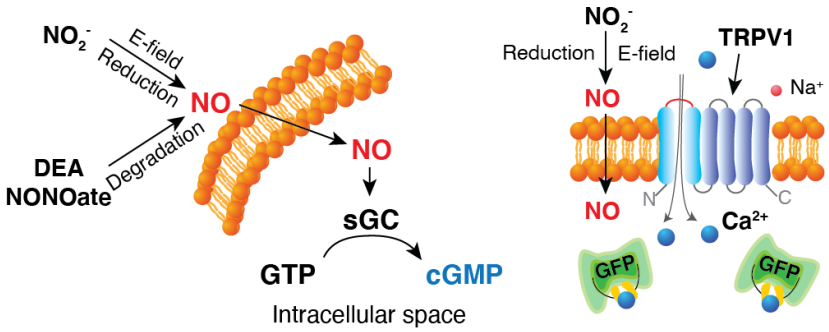

Figure 2-1: **A schematic illustrating electrochemical generation of NO for neuronal modulation**

2.2 Background and Motivation

2.2.1 Mammalian NO cycle and S-nitrosylation

Recently, it has been discovered that inorganic anions, such as nitrite (NO_2^-) or nitrate (NO_3^-), could be reduced into NO through several enzymatic or non-enzymatic pathways in biological systems [21–23](Figure 2-2). For example, ferrous deoxyhemoglobin, xanthine oxidoreductase, and cytochrome P450s utilized nitrite as a precursor for NO [22]. This nitrite-NO pathway in the mammalian nitrogen cycle complemented the classical NOS-dependent pathway, where NO is produced from L-arginine and molecular oxygen. The biological importance of the nitrite-NO pathway as an alternative source of NO has been highlighted, especially in the hypoxic state, and the therapeutic use of nitrite has been proposed [22, 24].

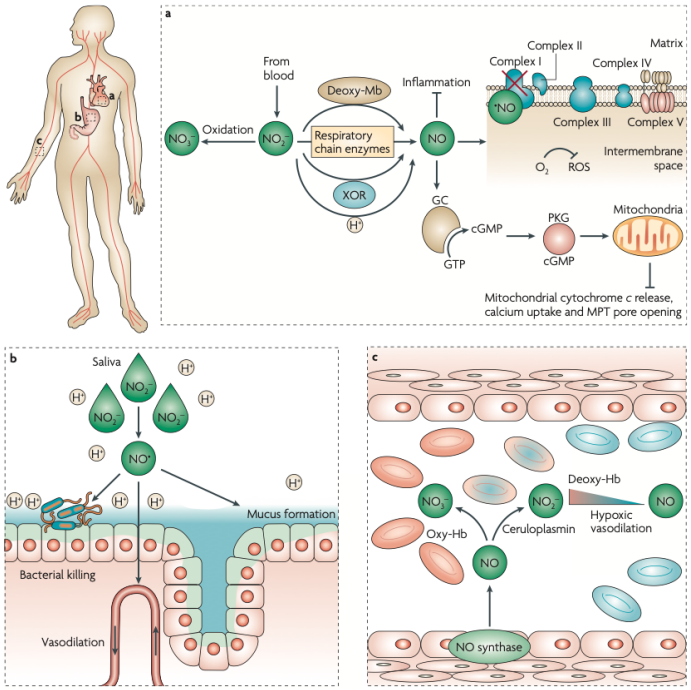

Figure 2-2: **Diverse pathways for nitrate/nitrite reduction to NO** Reprinted from [22].

NO generated from either the classical NOS-dependent pathway or the nitrite-NO pathway regulates diverse biological processes in vivo [25–27]. NO-mediated signaling processes were initially understood by their interaction with soluble guanylyl cyclase (sGC) to increase the intracellular level of the second messenger cyclic guanosine monophosphate (cGMP). In addition to the NO-cGMP pathway, emerging studies suggested that NO regulates cell signaling through S-nitrosylation of cysteine residues within proteins and nonprotein molecules, where it could covalently bind to modify their functions [28–32]. Mechanistic investigations on S-nitrosylation have revealed that this process is initiated by autoxidation of NO followed by the formation of nitrosating agent, ONOONO [33, 34], which can be written by the following equation (Equation2.1):

$$\begin{aligned} NO + O_2 &\longleftrightarrow ONOO \\ ONOO + NO &\longleftrightarrow ONOONO \end{aligned} \tag{2.1}$$

Then, ONOONO nitrosylates cysteine residues (RSH) according to the following equations (Equation2.2):

$$\begin{aligned} ONOONO + RSH &\longleftrightarrow RSNO + ONOO^- + H^+ \\ ONOO^- + RSH &\longleftrightarrow RS + NO_2 + OH^- \\ NO_2 + RSH &\longleftrightarrow RS + NO_2^- + H^+ \\ 2RS + 2NO &\longleftrightarrow 2RSNO \end{aligned} \tag{2.2}$$

The overall reaction is as follows (Equation2.3):

$$4NO + O_2 + 3RSH \longleftrightarrow NO_2^- + 3RSNO + H^+ + H_2O \tag{2.3}$$

These nitrosylated cysteine residues induce conformational changes of proteins by altering their intramolecular hydrogen bonding and electrostatic interactions [29, 32]. Moreover, in the case when S-nitrosylation occurs in the active cysteine site, enzymatic activity could be inhibited [28, 32]. Through these processes, the functions of proteins and nonprotein molecules could be significantly altered. For example, it

has been reported that the activities of transient receptor potential proteins, olfactory cyclic nucleotide-gated channels, and glyceraldehyde-3-phosphate dehydrogenase are significantly affected by NO through S-nitrosylation [32].

2.2.2 Electrochemical Nitrite Reduction and Nitrite Reductase

The biological nitrite-NO pathway suggests a potential way to artificially generate NO by reducing nitrite. However, under physiological conditions at pH 7.4, nitrite can be reduced into diverse forms other than NO, including N_2O, N_2, NH_2OH, and NH_3 [35]. Possible reduction pathways of nitrite and their corresponding thermodynamic reduction potentials are summarized below (Equation2.4):

$$\begin{aligned} NO_2^- + 2H^+ + e^- &\longleftrightarrow NO(g) + H_2O \\ 2NO_2^- + 6H^+ + 4e^- &\longleftrightarrow N_2O(g) + 3H_2O \\ 2NO_2^- + 8H^+ + 6e^- &\longleftrightarrow N_2(g) + 4H_2O \\ NO_2^- + 6H^+ + 4e^- &\longleftrightarrow NH_3OH^+ + H_2O \\ NO_2^- + 8H^+ + 6e^- &\longleftrightarrow NH_4^+ + 2H_2O \end{aligned} \tag{2.4}$$

Depending on the type of electrocatalysts used, the Faradaic efficiency for NO generation could be changed. It has been proposed that transition metals having a strong binding affinity to NO, such as Rh, would generate less NO compared to those having weak binding affinity to NO, such as Fe and Cu. Strong binding affinity to NO prevents desorption of NO from the metal surface to the solution and consequently adsorbed NO could be further reduced into other chemical forms before desorption [36]. Unfortunately, the role of transition metals on nitrite reduction reaction has not yet been systematically understood.

Biological nitrite reductase could give a hint for designing nitrite reduction reaction electrocatalysts for efficient NO generation. One well-known nitrite reductase in human is ferrous deoxyhemoglobin and nitrite reduction reaction driven by deoxyhe-

moglobin as summarized below [23] (Equation2.5):

$$NO_2^- + deoxyhemoglobin(Fe^{2+}) + H^+ \longleftrightarrow NO + methaemoglobin(Fe^{3+}) + OH^- \tag{2.5}$$

The key motif in the deoxyhemoglobin is the heme group where one ferrous ion (Fe^{2+}) is coordinated by five nitrogen atoms. (Here, four nitrogen atoms are from pyrrol groups in a porphyrin ring, whereas the other nitrogen atom is from an imidazole group in the globular protein). Nitrite could bind to the last coordination site of ferrous ions in the heme group and be reduced into NO [23]. Other examples of nitrite reductases can be found in plant, fungi, and bacteria [37–39]. The reduced form of Fe and S-based ferredoxin-nitrite reductase in plants could transfer electrons to nitrite by transforming into its oxidized form. In fungi and bacteria, there is a Cu-based nitrite reductase where two copper atoms are linked by a pair of amino acids. One Cu center serves the site where nitrite could bind and be reduced, whereas another Cu center transfers electrons for nitrite reduction reaction. Likewise, the existence of biological Fe- or Cu-based nitrite reductases implies the importance of Fe or Cu ions as key elements in the electrocataylsis of nitrite reduction reaction.

2.2.3 Thermal Drawing Process to Fabricate Multifunctional Probes

Recent advances in the development of multifunctional, flexible probes with thermal drawing process has allowed the modulation and probing of neuronal activity while minimizing the damage to the surrounding tissue [17, 40]. Generally, the thermal drawing process starts with the production of a macroscopic structure (preform) that incorporates materials and architectures of the desired probe. The preform is drawn into a miniature fiber by applying heat and tension with vertical furnace and capstan, respectively. During this process, the cross-sectional geometry can be maintained; however, the linear dimensions of the preform are reduced by 1–2 orders of magnitude. Moreover, by conservation of volume, the length of the resulting minia-

ture fiber becomes larger by 2–4 orders of magnitude compared to that of the preform. Through this process, a microscale fiber that shares a similar cross-sectional geometry with the preform can be fabricated in a scalable way [17].

2.2.4 Motivation

NO is a gaseous signaling molecule involved in multiple biological processes, including neurotransmission, cardiovascular homeostasis, and immune response [22, 28, 41, 42]. In the central nervous system, NO is involved in mediating synaptic plasticity and neurosecretion [43]. The essential role of NO across multiple signaling pathways has evoked a demand for regulating its levels in vitro and in vivo. Early studies have targeted endogenous NO synthase enzymes via genetic knock-out strategies or systemic delivery of pharmacological inhibitors [44–46]. More recently, NO-releasing materials (NORMs), triggered by non-enzymatic or enzymatic processes, have been designed to achieve more controlled and localized delivery of this molecule [47–49]. However, as the tuning of the NO-release kinetics in a single NORM has been challenging [47, 50], multiple injections of different NORMs were necessary to study the biological effects of NO [50, 51]. Furthermore, degradation of NORMs during delivery has often resulted in the off-target release of this molecule [52, 53]. Consequently, there remains a need for techniques enabling the local release of NO at the cells and tissues of interest with tuneable release kinetics.

2.3 Electrochemical NO Generation by Iron-Sulfide Nanocatalysts

To address the need for new NO-delivery techniques, we propose an electrocatalytic route to generate NO (Figure 2-3a). This approach draws inspiration from enzymatic denitrification reaction of nitrite (NO_2^-) or nitrate (NO_3^-) substrates in biological systems [54–56]. Although the detailed mechanism of NO generation by enzymes remains an area of active study, it has been demonstrated that metal atoms such as copper and iron in these enzymes serve as active catalytic sites for NO_2^- reduction processes [56]. We aim to mimic this biological NO generation by employing nanoscale iron sulfide-based catalysts for the electrochemical denitrification reaction (Equation2.6) [57]:

$$NO_{2\,((aq))}^- + 2H^+ + e^- \longleftrightarrow NO_{(g)} + H_2O_{(aq)} \qquad E_0 = 1.202\ V\ vs\ NHE \qquad (2.6)$$

Where NHE indicates normal hydrogen electrode. In the presence of an electric field, NO_2^- can be reduced by iron sulfide-based catalysts at the cathode allowing for the localized generation of NO. Furthermore, the NO release kinetics can be quantitatively controlled by varying the applied voltage. We applied this strategy to control NO-dependent neuronal signaling in vitro and in the mouse brain.

2.3.1 Design and Synthesis of Iron-Sufide Nanocatalysts

Fe_3S_4 nanocatalysts with diameters of 3 nm were prepared through a hot injection method [58]. To achieve increased catalytic activity and selectivity toward NO, we also explored Pt, a widely studied NO_2^- reduction catalyst [59, 60], as a hetero-atom dopant on the surface of the Fe_3S_4 nanoclusters. Pt decoration was conducted via a galvanic replacement method (Figure 2-3b-d) [61]. High-resolution high-angle annular dark-field scanning transmission electron microscopy (HAADF-STEM) images and bright-field STEM images revealed the presence of single Pt atoms and their clusters on the Fe_3S_4 nanocatalysts following the galvanic replacement (Figure 2-3d).

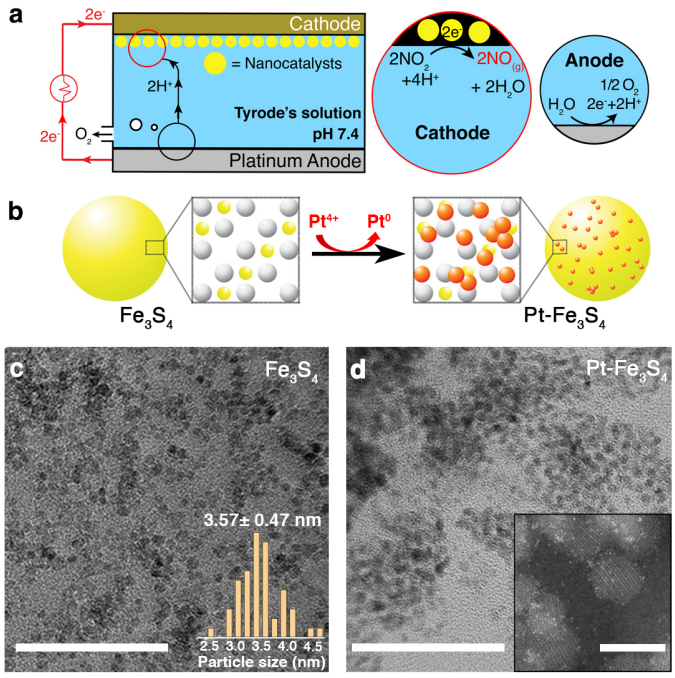

Figure 2-3: **Fe_3S_4 and Pt-Fe_3S_4 nanocatalysts for electrochemical reduction of NO_2^- into NO** a, An illustration of the electrochemical NO-delivery system. b, A schematic of the galvanic replacement method for decoration on the Fe_3S_4 nanocatalysts with Pt. Fe, S, and Pt atoms are marked in yellow, white, and red, respectively. c-d, Transmission electron microscope (TEM) images of the Fe_3S_4 (c) and the Pt-Fe_3S_4 (d) nanocatalysts. Scale bar: 50 nm. Insets show the size distribution of the Fe_3S_4, obtained from 50 randomly chosen nanoparticles (c) and high-resolution scanning TEM images of the Pt-Fe_3S_4 nanocatalysts (d). Scale bar: 5 nm. The experiment was repeated three times independently with similar results.

2.3.2 Electrocatalytic Activities of Iron-Sufide Nanocatalysts

Electrocatalytic activity of the Fe_3S_4 and Pt-decorated Fe_3S_4 nanocatalysts (Pt-Fe_3S_4) was assessed by loading them onto cathodes in a one-compartment electrochemical cell with a two-electrode configuration. In the absence of NO_2^-, cyclic voltammetry (CV) curves of the nanocatalysts exhibited only broad redox features appearing at approximately –2.0 V vs Pt, followed by hydrogen evolution reaction at approximately –2.3 V vs Pt. In the presence of 0.1 M $NaNO_2$, threshold voltages were positively shifted, and significant Faradaic currents appeared in the CV curves of Fe_3S_4 and Pt-Fe_3S_4 nanocatalysts. We found that these Faradaic currents increased as the concentration of NO_2^- or supporting electrolyte in the Tyrode's solution increased, confirming that NO_2^- was electrochemically reduced. As anticipated, Pt-Fe_3S_4 nanocatalysts showed higher activity as compared to Fe_3S_4 counterparts (Figure 2-4a,b).

The identity of the products in electrocatalytic cells with the Fe_3S_4 and Pt-Fe_3S_4 loaded cathodes was examined via chronoamperometry between –1.5 and –2.5 V and –1.25 V and –2.0 V vs Pt, respectively (Figure 2-4c,d). The amount of generated NO was quantified by using 4-amino-5-methylamino-2',7'-difluorofluorescein (DAF-FM), a NO capturing reagent [62], which reacts with NO to form a fluorescent benzotriazole derivative [63]. The measured NO concentration likely presents a lower-bound value due to the expected loss of this unstable molecule [34, 64]. The analysis thus only provided voltage-dependent electrochemical NO generation kinetics for each nanocatalyst. In the case of the Fe_3S_4 nanocatalysts, the amounts of captured NO monotonically increased with electrolysis time, implying that some of the generated NO could be accumulated despite its decay. Additionally, more NO was detected at greater negative voltages, consistent with CV and chronoamperometry results (Figure 2-4e). Similar electrokinetic trends were observed in the Pt-Fe_3S_4 nanocatalysts (Figure 2-4f). Consistent with CV measurements, the amount of captured NO produced at the Pt-Fe_3S_4 containing cathodes was higher than that produced at the cathodes loaded with Fe_3S_4 nanocatalysts. Based on the captured amount of NO, Faradaic efficiency

toward NO (FE_{NO}) was plotted versus the applied voltage. Due to the NO decay, 10-20 % of FE_{NO} was obtained and the FE_{NO} decreased over time during electrolysis.

In addition to NO, we also quantified undesirable side products at the cathode, such as molecular hydrogen (H_2(g)), ammonium ions (NH_4^+(aq)), and hydrogen peroxide (H_2O_2(aq)) and confirmed that negligible quantities of side products were generated (Figure 2-4g,h) [57]. At the anode, predominantly oxygen evolution was observed with minor evolution of chlorine (Figure 2-5). Taken together, these findings indicated that NO was the major NO_2^- reduction product for both nanocatalysts.

2.3.3 NO Generation Kinetics

To further understand the generation, diffusion, and decay of NO, we calculated the time- and distance-dependent NO concentration profiles with respect to the cathodes. Our calculations indicated that NO concentration rapidly decreased in the first 1000 μm from the cathode and the concentration profile reached steady state within a short period of time (< 1 s), due to autooxidation (Figure 2-6). These results indicated that the effects of electrochemically generated NO are spatially restricted due to its short half-life. Similarly, the type of electrocatalyst was shown to influence the equilibrium NO profiles .

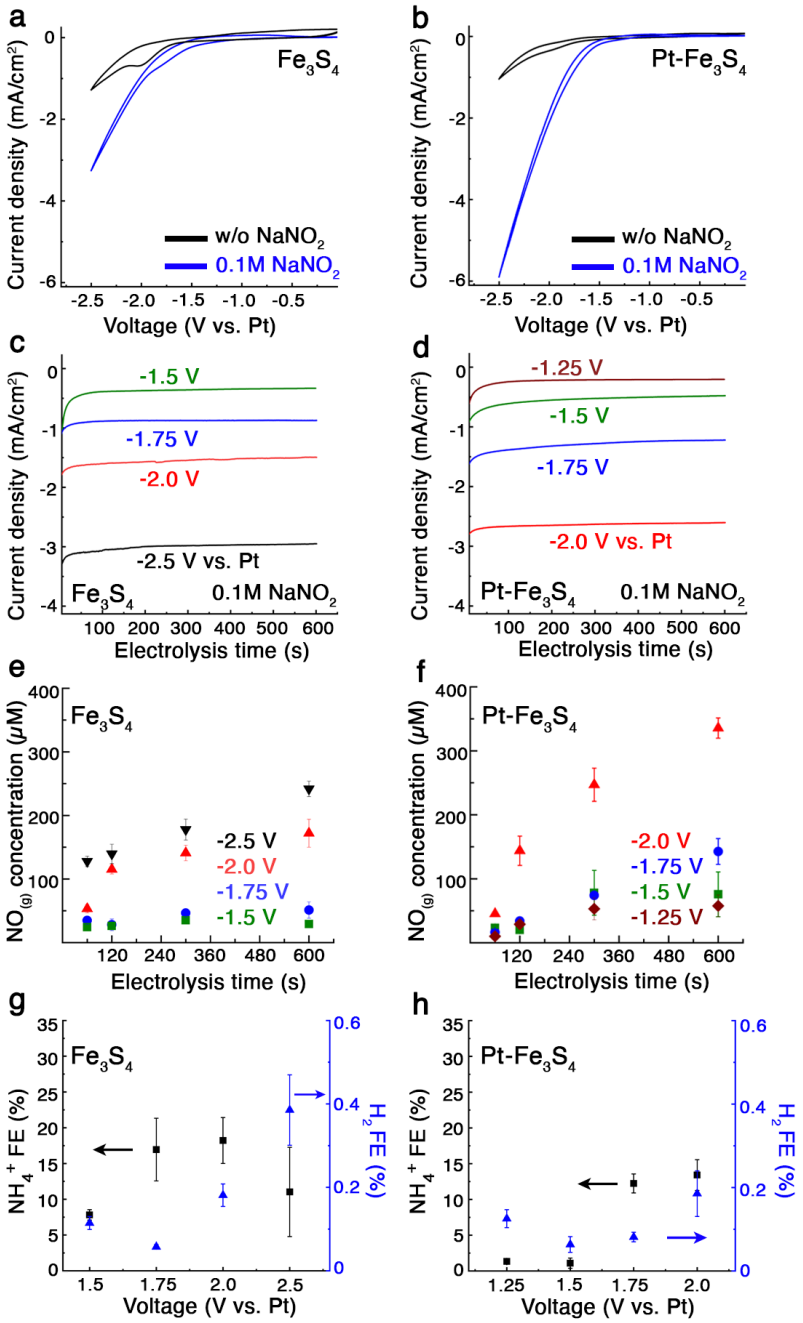

Figure 2-4: **Electrocatalytic activities of Fe_3S_4 and Pt-Fe_3S_4 nanocatalysts** a-b, CV curves of the Fe_3S_4 (a) and the Pt-Fe_3S_4 (b) nanocatalysts in the presence and absence of NO_2^-. Scan rate: 50 mV/s. c-d, Chronoamperometry profiles of the Fe_3S_4 (c) and the Pt-Fe_3S_4 (d) nanocatalysts. e-f, Voltage-dependent NO generation (mean ± standard deviation (s.d.)) from the Fe_3S_4 (e) and the Pt-Fe_3S_4 (f) nanocatalysts (n=3 independent experiments for each group). g-h, The Faradaic efficiency (FE) for NH_4^+ and H_2 (mean ± s.d.) from the Fe_3S_4 (g) and the Pt-Fe_3S_4 (h) nanocatalysts (n=3 independent experiments for each group). Voltage ranges of –1.5 V to –2.5 V and –1.25 V to –2.0 V vs Pt were chosen for the Fe_3S_4 and the Pt-Fe_3S_4 nanocatalysts, respectively.

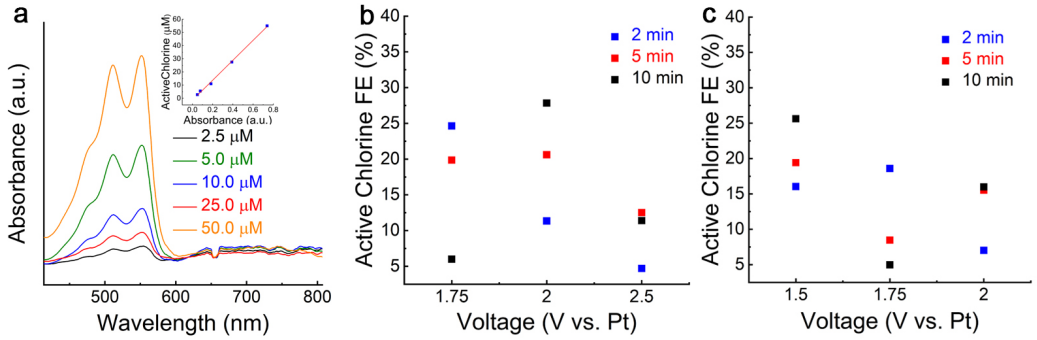

Figure 2-5: **Active chlorine N,N-diethyl-p-phenylenediamine (DPD) assay** a, Absorption spectra obtained for concentrations between 2.5 μM and 500 μM. The inset shows the calibration curve obtained from absorption at 515 nm. To quantify the active chlorine during electrolysis, we conducted chronoamperometry measurements. b-c, Voltage-dependent active chlorine Faradaic efficiency (FE) in electrolytic cells containing Fe_3S_4 (b) and the Pt-Fe_3S_4 nanocatalysts (c) at cathodes. These measurements indicate that oxygen evolution is likely the major counter-reaction. All experiments were conducted in Tyrode's solution.

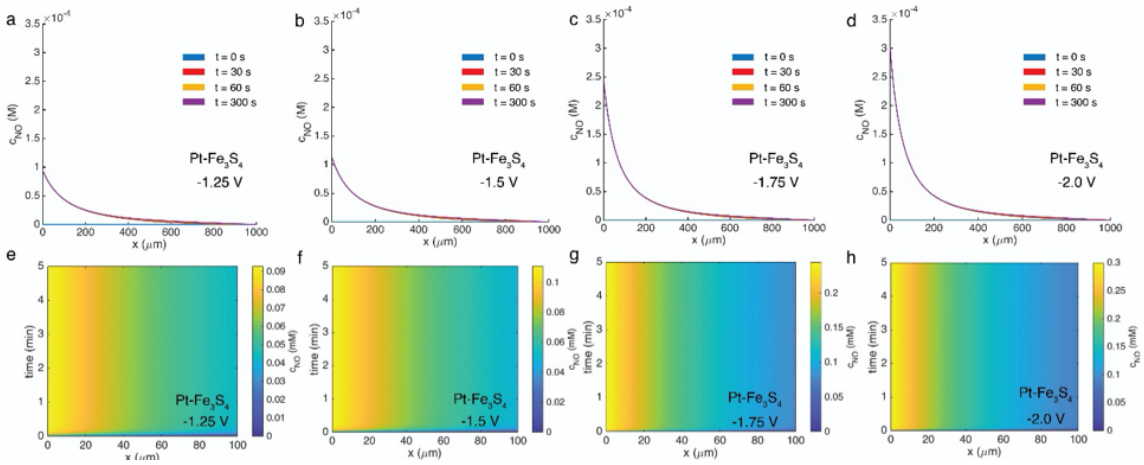

Figure 2-6: **Diffusion profile of electrochemically generated NO by Pt-Fe_3S_4 nanocatalysts** a-d, Voltage-dependent NO concentration distribution vs. the distance from the cathodes. e-h, Color map images display time and distance-dependent NO distribution.

2.4 Electrochemical Modulation of NO-mediated Cell Signaling In Vitro

2.4.1 Ca^{2+} Influx through Exogenous NO Sensor: TRPV1

To illustrate the utility of our electrocatalytic approach for controlling NO-mediated biological signaling, we first applied it to trigger NO-sensitive ion channels in vitro. Among the diversity of ion channels that react with NO, cation channels from the transient receptor potential vanilloid (TRPV) family were shown to be triggered by this molecule via S-nitrosylation of the cysteine residues within their pores [28, 65]. Consequently, we adopted TRPV family member 1 (TRPV1), a well-characterized receptor of thermal and chemical stimuli broadly expressed in the central and peripheral nervous system, as a test bed for NO-mediated signaling.

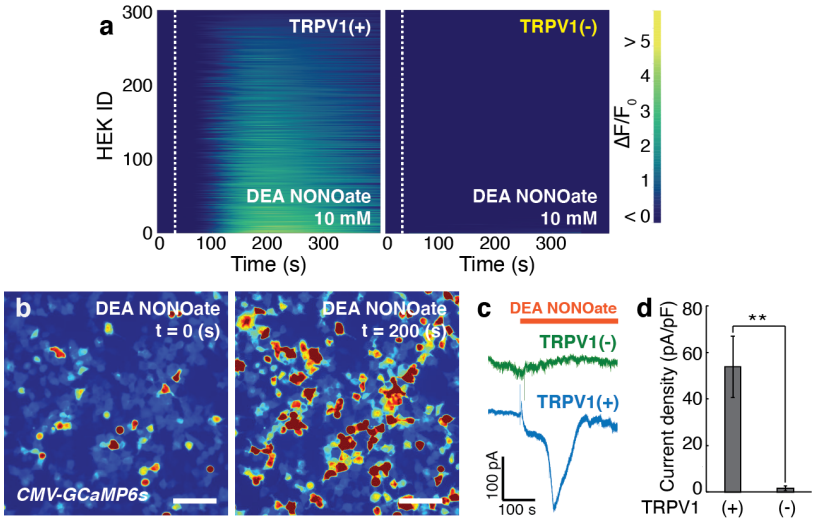

Figure 2-7: **NO donor triggers TRPV1** a, GCaMP6s fluorescence intensity in 300 $TRPV1^+$ (Left) or $TRPV1^-$ (Right) HEK293FT cells following addition of a NO donor, DEA NONOate (10 mM), at 30 s (dashed lines). b, Representative time-lapse images of global Ca^{2+} responses in $TRPV1^+$ cells in response to the DEA NONOate infusion. Scale bar: 50 μm. c, Representative whole-cell patch-clamp traces of $TRPV1^+$ cells (blue) and $TRPV1^-$ cells (green) in response to DEA NONOate infusion at the holding potential of –40 mV. d, Peak current density (mean ± standard error of the mean (s.e.m.)) following DEA NONOate infusion in $TRPV1^+$ cell or $TRPV1^-$ cells. A significant difference was observed between two groups, as confirmed by one-tailed Student's t-test (n = 7 cells for each group, ** ($p = 0.0038$) < 0.01).

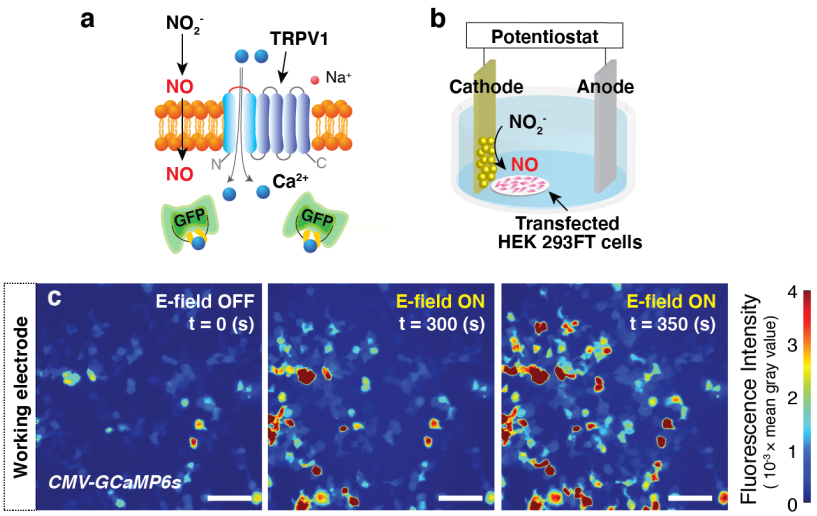

Figure 2-8: **Electrochemically produced NO activates TRPV1** a, A schematic illustrating Ca^{2+} influx through TRPV1 mediated by electrochemically produced NO. b, Experimental scheme for the electrochemical NO-delivery in vitro. c, Representative time-lapse images of Ca^{2+} influx into $TRPV1^+$ cells evoked by the Fe_3S_4-catalysed NO generation at –1.75 V vs Pt. The cathode decorated with the Fe_3S_4 nanocatalysts was positioned at the left edge in all the images. Scale bar: 50 μm.

Human embryonic kidney (HEK) 293FT cells were co-transfected with a plasmid carrying TRPV1 separated from a fluorescent protein mCherry by the posttranscriptional cleavage linker p2A under the excitatory neuronal promoter calmodulin kinase II α-subunit (CaMKIIα::TRPV1-p2A-mCherry) and a plasmid carrying a genetically encoded fluorescent calcium ion (Ca^{2+}) indicator GCaMP6s under the broad cytomegalovirus promoter (CMV::GCaMP6s). The latter allowed for monitoring of intracellular Ca^{2+} influx in response to the triggering of TRPV1. Consistent with previous reports [28, 65], an increase in intracellular Ca^{2+} in cells expressing TRPV1 ($TRPV1^+$) was observed in response to the NO donor (DEA NONOate), whereas cells not expressing TRPV1 ($TRPV1^-$) did not exhibit any increase in intracellular Ca^{2+}. Approximately 96 % of $TRPV1^+$ cells showed robust Ca^{2+} responses (as marked by the normalized GCaMP6s fluorescence increase $\Delta F/Fo \geq 50$ %) induced by 10 mM of the donor following 200 s (Figure 2-7a,b). A noticeable increase in intracellular Ca^{2+} was observed at donor concentrations as low as 500 μM. Consistent with Ca^{2+} imaging results, whole-cell patch-clamp recordings showed that the addition of the NO donor induced significant inward currents in $TRPV1^+$ cells, but not in $TRPV1^-$

cells (Figure 2-7c,d).

We then investigated whether the electrochemical NO-delivery could similarly evoke intracellular Ca^{2+} influx through TRPV1 (Figure 2-8a). In these experiments, conductive fluorine-doped tin oxide (FTO) substrates coated with Fe_3S_4 or Pt-Fe_3S_4 acted as cathodes against Pt anodes in Tyrode's solution containing 0.1 M $NaNO_2$. Cathodes were positioned in the immediate proximity of the $TRPV1^+$ cells to ensure the efficient delivery of NO (Figure 2-8b). NO generation catalysed by Fe_3S_4 nanoclusters at the cathode triggered Ca^{2+} influx into $TRPV1^+$ cells. At –1.75 V vs Pt, only $TRPV1^+$ cells within 50 μm proximity from the cathode were activated after 300 s. Consistent with our calculations of the NO diffusion profiles, the Ca^{2+} influx into the $TRPV1^+$ cells located at greater distances from the cathodes was triggered gradually (Figure 2-8c).

Ca^{2+} influx into $TRPV1^+$ cells at the identical reaction conditions was blocked by the addition of 20 μM TRPV1 antagonist BCTC (N-(4-tertiarybutylphenyl)-4-(3-chloropyridin-2-yl) tetrahydropyrazine-1(2H)-carboxamide) [66]. No substantial Ca^{2+} influx was observed in $TRPV1^-$ cells in the presence of applied voltage and $NaNO_2$ and in $TRPV1^+$ cells in the absence of $NaNO_2$. Additionally, injection of NH_4^+, a minor byproduct of the NO_2^- reduction, did not yield measurable Ca^{2+} responses in $TRPV1^+$ cells (Figure 2-9). Furthermore, we found that ascorbate, which can selectively reduce nitrosothiol generated from the interaction between NO and thiol groups in TRPV1 [28,32], reduced the intracellular Ca^{2+} concentration as indicated by the decrease in GCaMP6s fluorescence (Figure 2-10). These results supported that the Ca^{2+} influxes observed in $TRPV1^+$ cells are mainly attributable to electrochemically formed NO.

The electrochemical approach further afforded variations in the latency of the Ca^{2+} responses in $TRPV1^+$ cells. Consistent with the accelerated NO release kinetics, lower latency Ca^{2+} responses were observed in $TRPV1^+$ cells by increasing the negative voltage at the nanocatalyst loaded cathodes vs Pt (Figure 2-11). In the presence of Fe_3S_4 nanocatalysts, a robust increase in GCaMP6s fluorescence ($\Delta F/Fo \geq 50$ %) in $TRPV1^+$ cells was observed 255 $\pm$ 3 s, 192 $\pm$ 1 s, and 92 $\pm$ 2 s following application

of –1.75 V, –2.0 V, and –2.5 V, respectively. Peak Ca^{2+} influx was observed at 345 s at –1.75 V, 265 s at –2.0 V, and 144 s at –2.5 V. No response was observed at voltages $\geq$ –1.5 V (Figure 2-11a-b). Higher electrocatalytic activity of Pt-Fe_3S_4 nanoclusters allowed for NO generation at lower negative voltages ($\geq$–1.5 V), and lower latency Ca^{2+} responses were observed as compared to those observed for Fe_3S_4 nanocatalysts at the same applied voltage (Figure 2-11c-d).

Electrochemically generated NO was sufficient to activate $TRPV1^+$ primary hippocampal neurons. The neurons were co-transduced with lentivirus and adeno-associated virus serotype 9 carrying TRPV1-p2A-mCherry and GCaMP6s under CaMKIIα and broad neuronal human synapsin promoter, respectively (Lenti-CaMKII α::TRPV1-p2A-mCherry and AAV9-hSyn::GCaMP6s) (Figure 2-12a-b). In the presence of Fe_3S_4 or Pt-Fe_3S_4 nanocatalysts, NO generated by applying –2.0 V was sufficient to drive Ca^{2+} influx into 87 % of $TRPV1^+$ neurons ($\Delta F/Fo \geq 50$ %). In contrast, negligible Ca^{2+} responses were evoked in $TRPV1^-$ neurons at identical reaction conditions. Consistent with observations in HEK293FT cells, the latency to reach GCaMP6s fluorescence increase $\Delta F/Fo \geq 50$ % in $TRPV1^+$ neurons was shorter in the presence of Pt-Fe_3S_4 (153 $\pm$ 2 s) than in the presence of Fe_3S_4 nanocatalysts (234 $\pm$ 10 s) (Figure 2-12c-f).

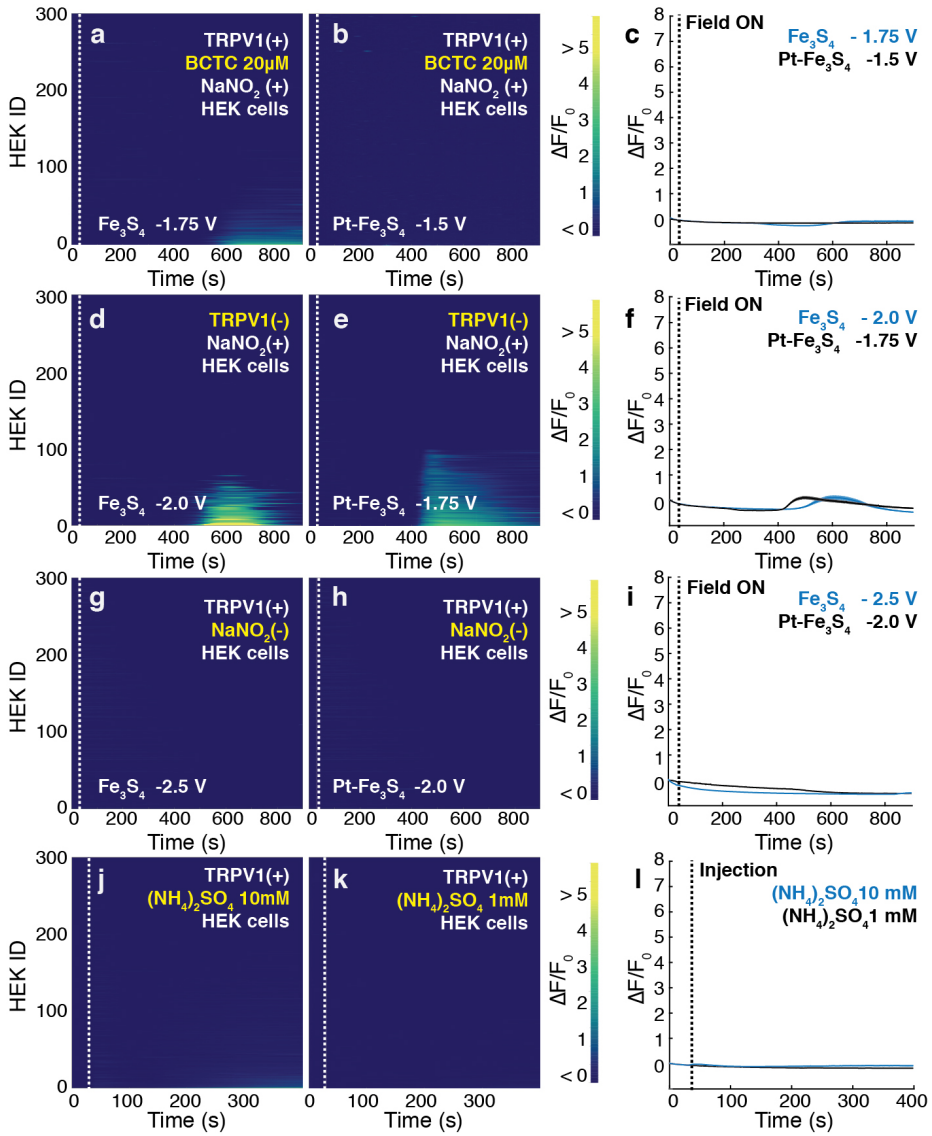

Figure 2-9: **Control groups to examine NO-mediated Ca^{2+} responses** a-c, Individual (a, b) and averaged (c) GCaMP6s fluorescence traces for $TRPV1^+$ HEK293FT cells (n = 300 cells for each trace) pre-incubated with 20 μM of TRPV1 antagonist, following NO delivery electrocatalysed by Fe_3S_4 at –1.75 V (a) and Pt-Fe_3S_4 at –1.5 V vs Pt (b) in the presence of 0.1 M $NaNO_2$. d-f, Individual (d, e) and averaged (f) GCaMP6s fluorescence traces for TRPV1– cells (n = 300 cells for each trace) following NO delivery electrocatalysed by Fe_3S_4 at –1.75 V (d) and Pt-Fe_3S_4 at –1.5 V vs Pt (e) in the presence of 0.1 M $NaNO_2$. g-i, Individual (g, h) and averaged (i) GCaMP6s fluorescence traces for $TRPV1^+$ cells (n = 300 cells for each trace) in the presence of Fe_3S_4 at –2.5 V (g) and Pt-Fe_3S_4 at –2.0 V vs Pt (h) without $NaNO_2$. j-l, Individual (j, k) and averaged (l) GCaMP6s fluorescence traces for $TRPV1^+$ cells (n = 300 cells for each trace) following addition of 10 mM (j) or 1 mM $(NH_4)_2SO_4$ (k) containing Tyrode's solution, respectively.

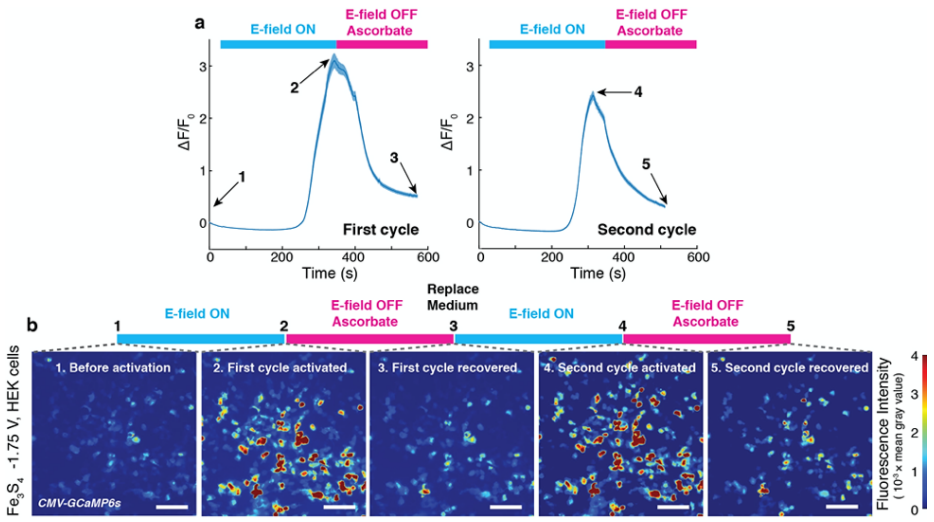

Figure 2-10: **Effects of a reducing agent on NO-mediated cell signaling** a, Normalized GCaMP6s fluorescence averaged across 300 TRPV1$^+$ HEK293FT cells during the first (left) and second (right) activation-and-recovery cycle. Activation of TRPV1$^+$ cells was achieved by the NO release catalyzed by Fe_3S_4 nanoclusters at –1.75 V vs Pt. When peak Ca^{2+} influx was observed, the voltages were turned off and sodium ascorbate was added into the solution to the final concentration of 33 mM (recovery). The entire reaction solution was carefully replaced with fresh Tyrode's solution with 0.1 M $NaNO_2$ between the two cycles. b, Representative time-lapse images of Ca^{2+} responses in TRPV1$^+$ cells during the first and second activation-and-recovery cycles in the presence of sodium ascorbate. Scale bar: 50 μm.

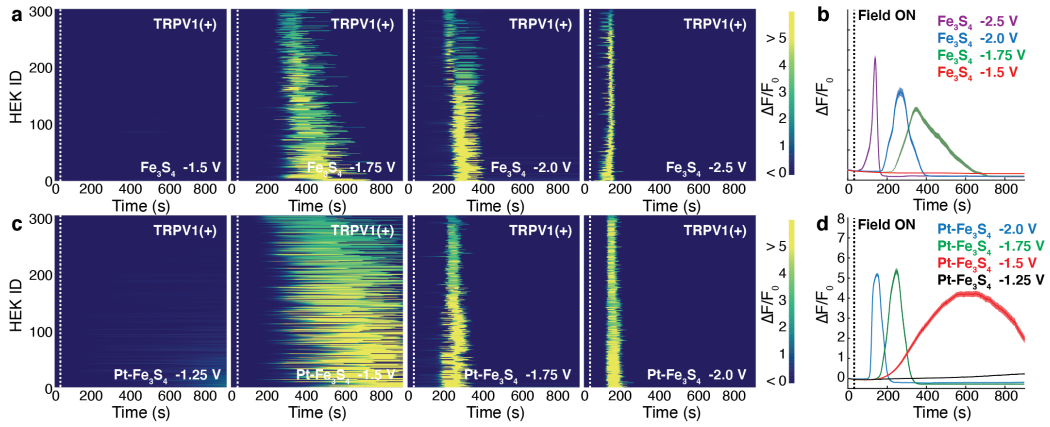

Figure 2-11: **Spatiotemporally controlled activation of TRPV1 with electrochemically produced NO** a-d, Individual (a, c) and averaged (b, d) GCaMP6s fluorescence traces for TRPV1$^+$ cells (n = 300 cells for each trace) in the presence of Fe_3S_4 (a, b) and the Pt-Fe_3S_4 (c, d) nanocatalysts and 0.1 M $NaNO_2$. Voltages of –1.5, –1.75, –2.0, –2.5 V and –1.25, –1.5, –1.75, –2.0 V vs Pt were applied at 30 s (dashed lines) in the presence of Fe_3S_4 and Pt-Fe_3S_4 nanocatalysts, respectively. b, d, Solid lines, and shaded areas indicate the mean and s.e.m., respectively. F_0 indicates the mean of the fluorescence intensity during the initial 10 s of measurement.

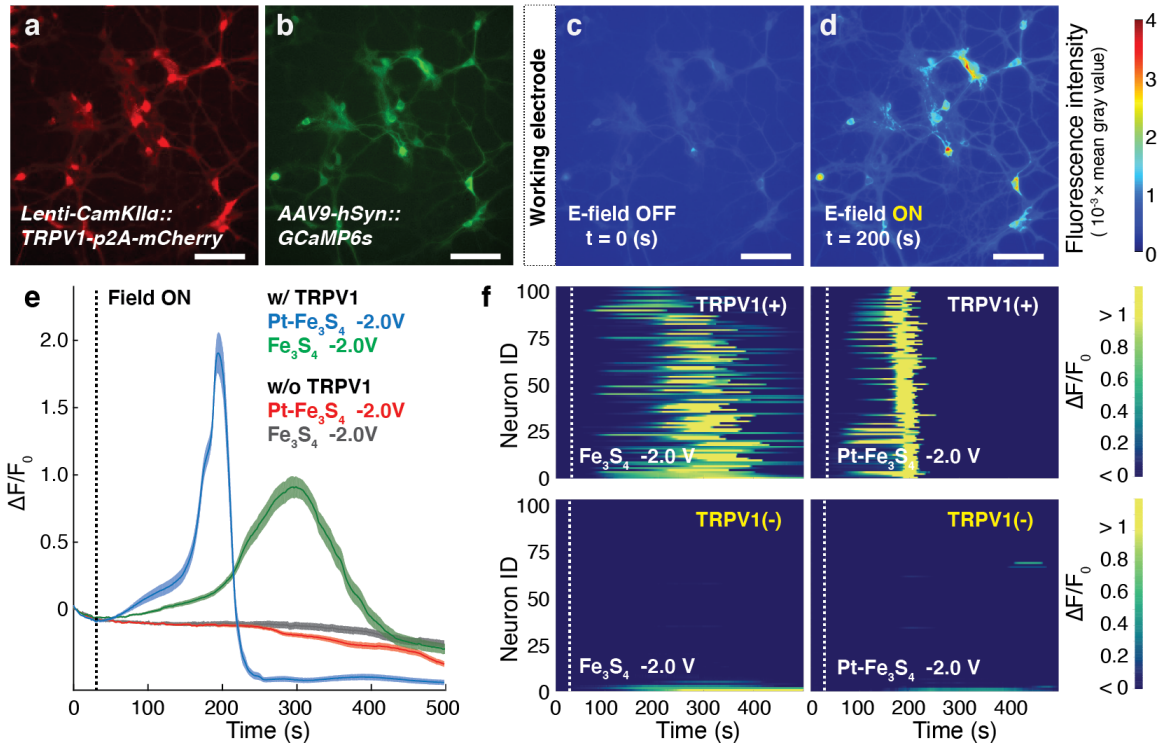

Figure 2-12: **Neuronal Ca^{2+} responses mediated by electrocatalytic NO generation in vitro** a-b, Fluorescent images of hippocampal neurons co-transduced with TRPV1 and GCaMP6s. Scale bar: 50 μm. c-d, Representative images of GCaMP6s intensity of $TRPV1^+$ neurons prior to (c) and following (d) NO release electrocatalysed by Pt-Fe_3S_4 at –2.0 V vs Pt. The Pt-Fe_3S_4 nanocatalysts-loaded cathode was located at the left edge in all the images. (a-d) The experiment was repeated three times independently with similar results. e, Normalized GCaMP6s fluorescence averaged across $TRPV1^+$ and $TRPV1^-$ neurons (n = 100 neurons for each trace) following NO delivery electrocatalysed by Pt-Fe_3S_4 and Fe_3S_4 nanoclusters at –2.0 V vs Pt applied at 30 s (dashed line). Solid lines and shaded areas indicate the mean and s.e.m., respectively. f, Individual GCaMP6s fluorescence in 100 $TRPV1^+$ and 100 $TRPV1^-$ neurons following NO delivery electrocatalysed by Pt-Fe_3S_4 and Fe_3S_4 at –2.0 V vs Pt applied at 30 s (dashed lines). F_0 indicates the mean of the fluorescence intensity during the initial 10 s of measurement.

2.4.2 Endogenous NO-sGC-cGMP Pathway

We then examined whether electrochemically generated NO could activate the soluble guanylate cyclase (sGC), an intracellular and endogenous NO receptor, in genetically intact cerebellar neurons. The sGC activity in neurons was evaluated by measuring the intracellular cyclic guanosine 3'5'-monophosphate (cGMP) levels (Figure 2-13a). Consistent with prior research [67], a substantial increase in cGMP levels in the neurons ($\sim$ 800 %) was observed following the addition of 10 mM of the NO donor (Figure 2-13b). Similarly, NO generated by Pt-Fe_3S_4 nanocatalysts at –2.5 V vs Pt increased the cGMP levels in the cerebellar neurons, whereas no significant changes in the cGMP levels were found in the absence of the applied voltage or addition of $NaNO_2$ (Figure 2-13c). These results indicated that our electrocatalytic approach could be extended to modulate the endogenous NO-signaling pathways. For instance, in future it may be possible to apply our approach to advance the study of synaptic plasticity mediated by NO through its interactions with sGC [43]. Furthermore, the spatial restriction and tuneable kinetics afforded by our approach may offer additional insights into the role of NO in specific circuits or signaling cascades [68].

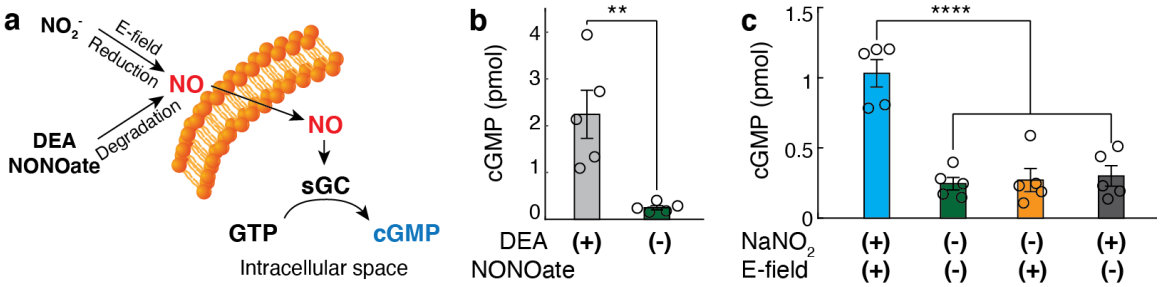

Figure 2-13: **Electrochemical modulation of NO-sGC-cGMP signaling pathway** a, An illustration of the NO-sGC-cGMP signaling pathway in genetically intact cerebellar neurons. GTP stands for guanosine 5'-triphosphate. b, Intracellular cGMP levels (mean $\pm$ s.e.m.) in 5×10^6 cerebellar neurons following incubation with DEA NONOate (10 mM) or Tyrode's solution for 5 min. A significant difference was found between two groups, as assessed by one-tailed Student's t-test (n = 5 independent experiments for each group, ** ($p = 0.0089$) < 0.01). c, Intracellular cGMP levels (mean $\pm$ s.e.m.) in 5×10^6 cerebellar neurons following NO delivery electrocatalysed by Pt-Fe_3S_4 at –2.5 V vs Pt for 5 min. Statistical significance of an increase in cGMP levels after NO delivery as compared to controls was confirmed by one-way ANOVA and Tukey's multiple comparison test (n = 5 independent experiments for each group, $F_{3,16} = 24.41$, **** ($p = 3.3\times10^{-6}$) < 0.0001).

2.5 Design and Characterization of Implantable, NO Delivery Probes

2.5.1 Fabrication of NO Delivery Probes with Fiber Drawing Process

To investigate the utility of our NO-delivery approach for applications in vivo, we designed miniature electrocatalytic probes suitable for chronic implantation into the mouse brain. We adopted a thermal drawing process that has previously enabled the fabrication of multifunctional, fibers for neural interfaces (Figure 2-14) [17, 40]. A macroscopic polycarbonate preform (12 mm in diameter) containing three hollow channels was fabricated by standard machining (Figure 2-14b). One of the channels was intended for delivery of $NaNO_2$ solution and the remaining two channels were designed to host microelectrodes forming the electrocatalytic cell for reduction of the delivered $NaNO_2$ into NO. During the draw (Figure 2-14a), the preform (Figure 2-14b) was heated above the polycarbonate glass transition temperature and stretched into a 5 m-long fiber with a diameter of $\sim$ 400 μm (Figure 2-14c-d). Tungsten and gold-coated tungsten microwires (50 μm in diameter) were directly converged into the preform from the wire spools (Figure 2-14a), resulting in a probe featuring two microelectrodes and a microfluidic channel. Following fiber connectorization to external tubing and electrical pin connectors, 300 μm lengths of the embedded microwires were exposed from the fiber tips for further functionalization. Pt-Fe_3S_4 nanoclusters, which exhibited greater electrocatalytic activity as compared to Fe_3S_4 counterparts, were deposited onto the exposed gold-coated tungsten microwire cathodes. The tungsten microwires were electroplated with Pt and used as the anodes (Figure 2-15a) [69]. The fully assembled NO-delivery fibers exhibited height and weight of 25 mm and 0.3-0.4 g, respectively (Figure 2-15b).

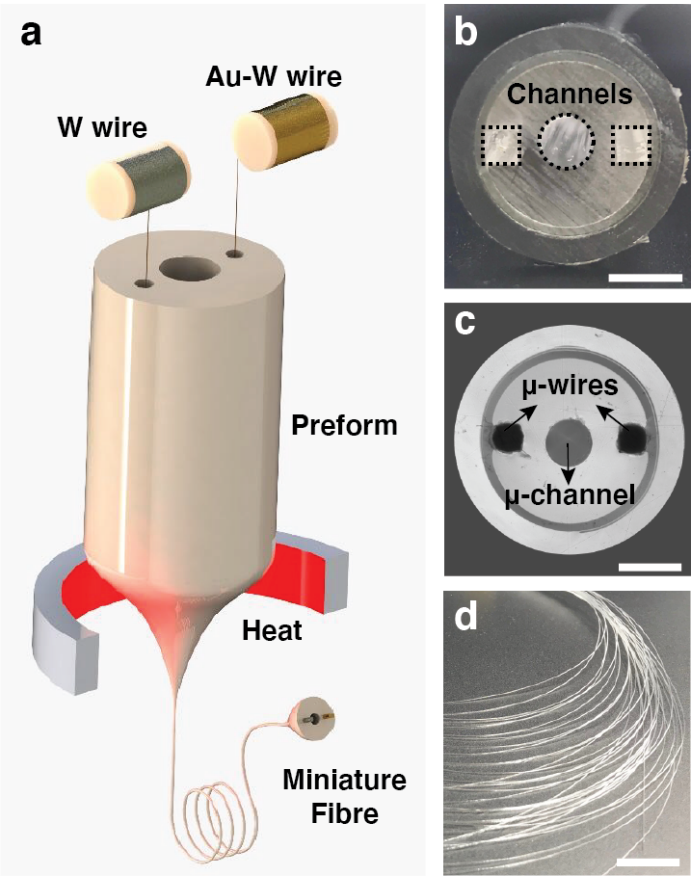

Figure 2-14: **Fabrication of the NO-delivery fiber** a, An illustration of the fiber drawing process. Tungsten and gold-plated tungsten wires were converged into the preform during the draw. b, Cross-sectional image of the preform containing three hollow channels. Scale bar: 3 mm. c, Cross-sectional microscope image of the resulting fiber. Scale bar: 100 μm. d, A photograph of a bundle of fiber produced during the draw. Scale bar: 10 cm.

2.5.2 NO Generation through Microscale, NO Delivery Probes

The microfluidic capabilities of the probes were corroborated by passing the solution of a blue dye and $NaNO_2$ into agarose brain phantoms (Figure 2-15c). Electrocatalytic conversion of the delivered $NaNO_2$ into NO was characterized via chronoamperometry. The current density at the exposed microwires (50 μm in diameter and 300 μm in length) was –4 mA/cm^2 at –2.0 V vs Pt, which was similar to that in the bulk electrochemical cells used for the in vitro studies (Figure 2-4d, Figure 2-15d). Akin to the bulk cells, the electrocatalytic fibers were capable of NO generation at the cathodes, which mediated Ca^{2+} influx in TRPV1$^+$ cells in vitro(Figure 2-16), while oxygen evolution mainly occurred at the anodes (Figure 2-17).

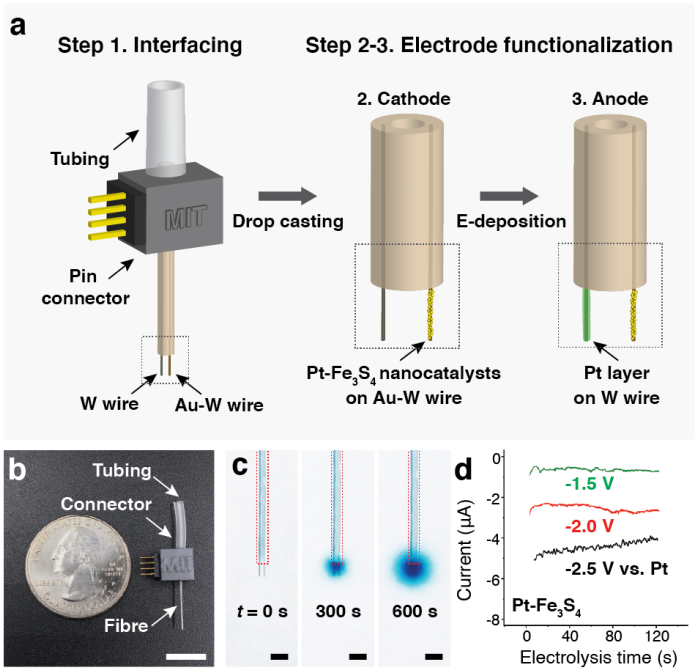

Figure 2-15: **Functionalization and characterization of the NO-delivery fiber** a, An illustration of fiber connectorization, followed by functionalization of the cathode and anode microwires with Pt-Fe_3S_4 nanocatalysts and Pt layer, respectively. b, A photograph of a fully assembled NO-delivery fiber. Scale bar: 10 mm. c, Infusion of Tyrode's solution containing 0.1 M $NaNO_2$ and a dye (BlueJuice) into a brain phantom (0.6% agarose gel) through the microfluidic channel. Images were taken at 0, 300 and 600 s after the infusion at a rate of 100 nL/min. Scale bar: 500 μm. d, Chronoamperometry profiles of the NO-delivery fiber in the Tyrode's solution containing 0.1 M $NaNO_2$.

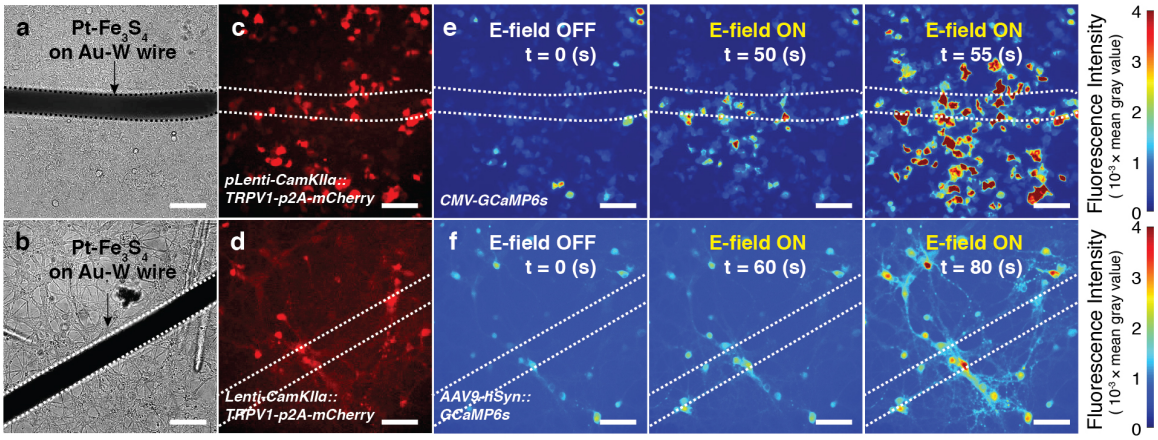

Figure 2-16: **In vitro neuronal responses induced by NO-delivery fiber** a-b, Optical images of Pt-Fe_3S_4 nanocatalysts coated microwires of the NO-delivery fiber, positioned above the $TRPV1^+$ HEK293FT cells (a) or $TRPV1^+$ hippocampal neurons (b). c-d, Fluorescent images of $TRPV1^+$ cells (c) and neurons (d), positioned below the microwires in a and b, respectively. White dotted lines indicate the positions of microwires onto cells and neurons. e-f, Representative time-lapse images of Ca^{2+} responses in $TRPV1^+$ HEK293FT cells (e) and neurons (f) elicited by Pt-Fe_3S_4 electrocatalyzed NO generation at –2.0 V vs Pt, indicating the localized activation of TRPV1 in the proximity of the microwires. Scale bar: 50 μm.

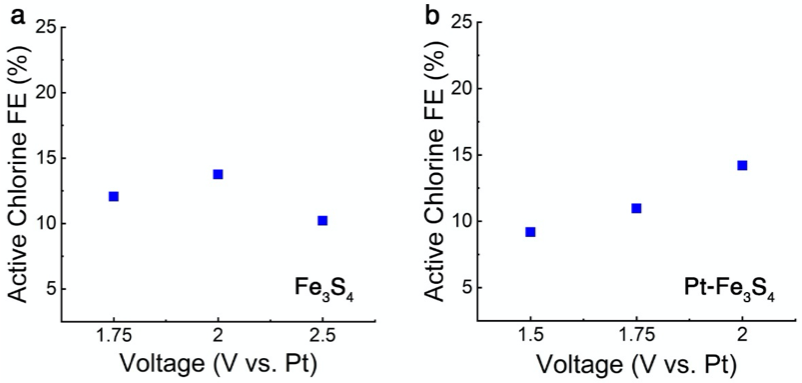

Figure 2-17: **Active chlorine assay on the miniature fiber electrode** a-b, Voltage-dependent active chlorine Faradaic efficiency (FE) in electrolytic cells containing Fe_3S_4 (a) and the Pt-Fe_3S_4 nanocatalysts (b) at cathodes. These measurements indicate that oxygen evolution is likely the major counter-reaction. All experiments were conducted in Tyrode's solution.

2.6 NO-mediated Neuronal Stimulation In Vivo

2.6.1 Probe Implantation and NO Generation in the Mouse Brain

We next applied the electrocatalytic fibers to drive NO-mediated responses in vivo (Figure 2-18). We chose mouse ventral tegmental area (VTA) as our target brain region due to its low endogenous TRPV1 expression levels and well-characterized projection circuits [70–72]. The mice were transduced in the VTA with Lenti-CaMKIIα::TRPV1-p2A-mCherry (TRPV1$^+$) or a control virus (Lenti-CaMKIIα::mCherry,TRPV1$^-$) to account for potential effects of NO on the endogenously expressed channels [73, 74]. Following a 6-8 weeks incubation period, the mice were implanted with NO-generation fibers in the same region. TRPV1 expression as marked by mCherry fluorescence was observed in the $\sim$350 μm radial vicinity from the viral injection sites in the VTA (Figure 2-19). The anatomical locations of the exposed microwires of the implanted electrocatalytic fibers were aligned with TRPV1 expression in the VTA. To locally generate NO with the implanted fibers, Tyrode's solution containing 0.1 M $NaNO_2$ was infused into the VTA via the microfluidic channels and –2.5 V was applied to the integrated Pt-Fe_3S_4 coated cathodes vs the integrated Pt-coated anodes (Figure 2-18).

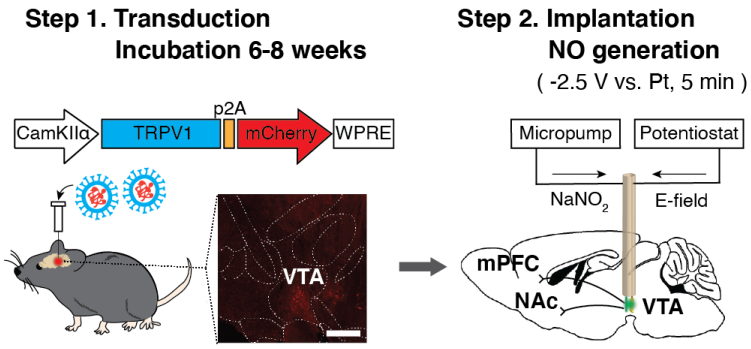

Figure 2-18: **An experimental scheme for neuronal stimulation with NO-delivery fibers in vivo** An illustration of the virus-assisted gene delivery, fiber implantation, and NO generation in the mouse brain. Inset: A confocal image of TRPV1-p2A-mCherry expression in the mouse VTA. Scale bar: 500 μm.

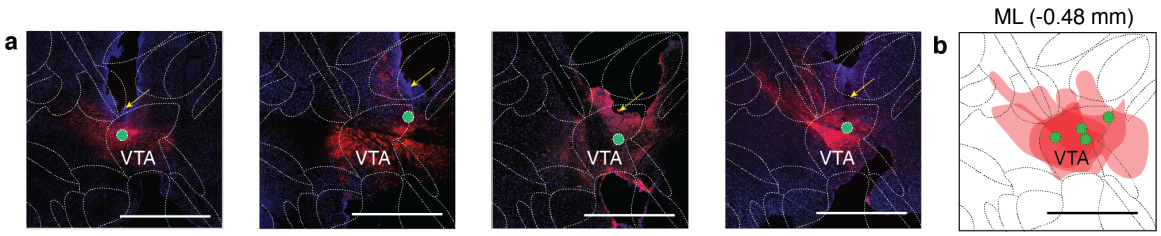

Figure 2-19: **TRPV1 expression and fiber implantation in the mouse brain** a, Four representative confocal images of the VTA of TRPV1$^+$ mice implanted with NO-delivery fibers. Red fluorescence and green dots indicated the transduction area of TRPV1, which is tagged with mCherry, and anatomical locations of exposed microwires of the fibers, respectively (scale bar = 1 mm). b, The overlay of four confocal images in a with the histological brain image (black line), which is reproduced from Paxinos and Franklin's the Mouse Brain in Stereotaxic Coordinates (Academic Press, 2019) (scale bar = 1 mm).

2.6.2 Analysis of NO-mediated Neuronal Excitation In Vivo

The extent of NO-mediated neuronal excitation in the VTA was first investigated via the immunofluorescence analysis of the expression of an immediate-early gene c-fos, which was previously shown to be upregulated in electroactive cells in response to Ca^{2+} influx [75]. Consistent with these prior reports [71, 72], a significantly higher percentage of c-fos positive cells relative to all cells as marked by nuclear stain DAPI was found in the VTA of TRPV1$^+$ mice subjected NO generation as compared to control groups, which included TRPV1$^+$ mice where the voltage was not applied following $NaNO_2$ delivery, TRPV1$^-$ mice subjected to NO generation, and TRPV1$^-$ mice where the only voltage was applied without $NaNO_2$ delivery (Figure 2-20a,b). We also observed upregulation of c-fos expression in the nucleus accumbens (NAc) and medial prefrontal cortex (mPFC) of TRPV1$^+$ mice subjected to electrocatalytic NO generation (Figure 2-20c-f). The NAc and mPFC receive excitatory projections from the VTA [70–72].

Consistent with c-fos expression analyses, fiber photometry recordings of GCaMP6s fluorescence showed that NO released from the implanted fibers could trigger neuronal activity in the VTA (Figure 2-21, Figure 2-22a). In these experiments, a cocktail of Lenti-CaMKIIα::TRPV1-p2A-mCherry (or Lenti-CaMKIIα::mCherry) and AAV9-hSyn:: GCaMP6s was injected into the mouse VTA (Figure 2-22b). Following a 6-8

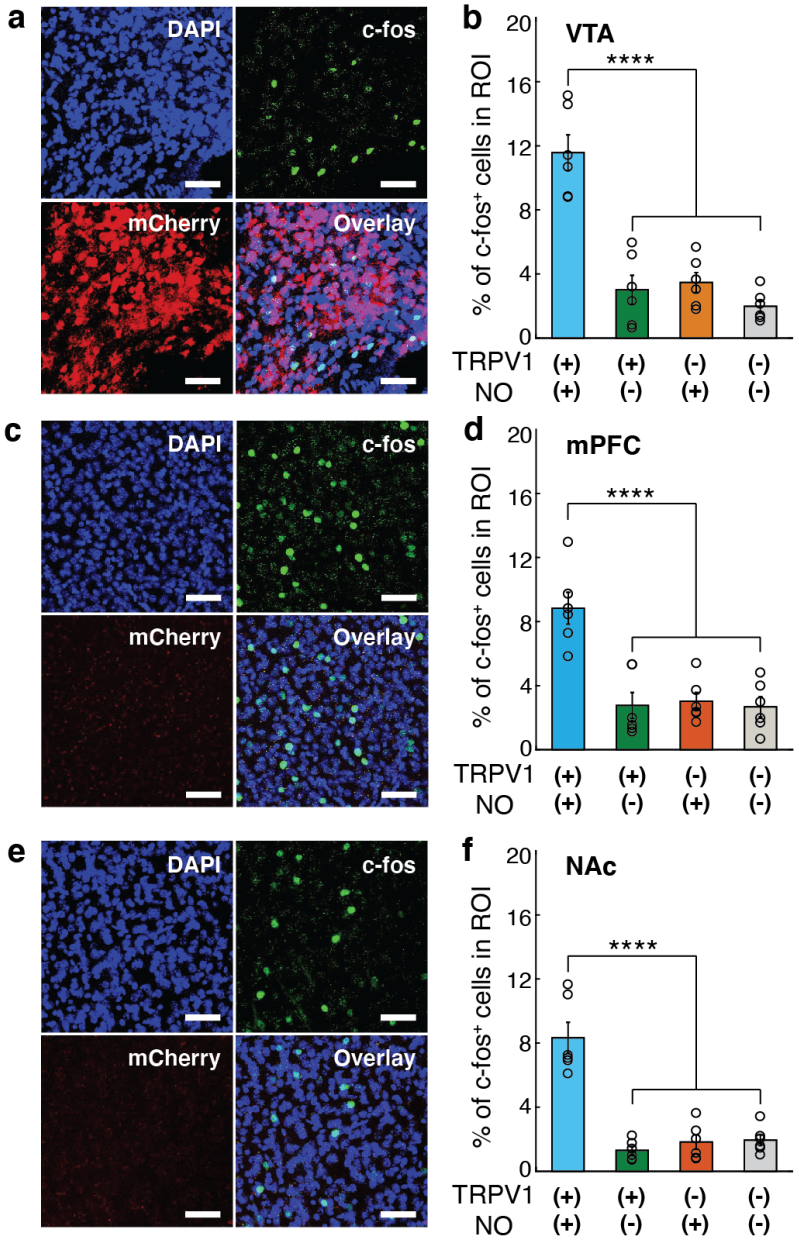

Figure 2-20: **Upregulation of c-fos expression after NO delivery** a-f, Confocal images (in TRPV1$^+$ mice) (a, c, and e) and percentages of the c-fos expressing neurons among DAPI-labeled cells (mean ± s.e.m.) (b, d, and f) in the region of interest (ROI) in the VTA (a, b), mPFC (c, d), and NAc (e, f) following electrocatalytic NO generation in the VTA. Scale bar: 50 μm. Statistical significance of an increase in c-fos expression after NO generation in TRPV1$^+$ mice as compared to controls was confirmed by one-way ANOVA and Tukey's multiple comparison tests (n = 6 mice, VTA $F_{3,20} = 29.97$ $p = 1.3\times10^{-7}$, mPFC $F_{3,20} = 15.49$ $p = 1.92\times10^{-5}$, NAc $F_{3,20} = 33.54$ $p = 5.4\times10^{-8}$, **** $p < 0.0001$).

week incubation period, the mice were implanted with the NO delivery fibers in the VTA and the conventional silica optical fibers the NAc, respectively (Figure 2-22c).

Confocal image analyses confirmed the GCaMP6s expression in cell bodies in the VTA and the VTA axons projecting to the NAc (Figure 2-21). Consistent with prior studies that have shown that neuronal stimulation in the VTA can be photometrically detected in their excitatory projections in the NAc [72], we found that in $TRPV1^+$ mice NO-mediated excitation of the VTA neurons yields an increase in the GCaMP6s fluorescence in their terminals in the NAc. A modest increase in intracellular Ca^{2+} was observed following a 60 s long application of –2.0 V to the fiber cathodes in the presence of $NaNO_2$. Applying –2.5 V has resulted in a rapid rise in GCaMP6s fluorescence consistent with accelerated NO generation kinetics. No significant GCaMP6s fluorescence change was observed in $TRPV1^-$ mice under the same stimulation conditions (Figure 2-22d). These findings indicate that the interplay between the TRPV1 overexpression and NO delivery in the VTA dominates over other possible mechanisms potentially contributing to the GCaMP6s fluorescence increase in the NAc, including modulation of non-VTA neurons potentially projecting to the NAc from the surrounding regions that could have been directly transduced by the AAV9-hSyn::GCaMP6s. Similarly, the application of the cathode voltage alone was insufficient to evoke Ca^{2+} influx in the NAc projecting axons in either $TRPV1^+$ or $TRPV1^-$ mice (Figure 2-22d). This is expected as the current elicited by –2.5 V was $\sim 5\ \mu$A, which was significantly lower than the values ($\geq 50\ \mu$A) typically used for direct electric neural stimulation [76, 77].

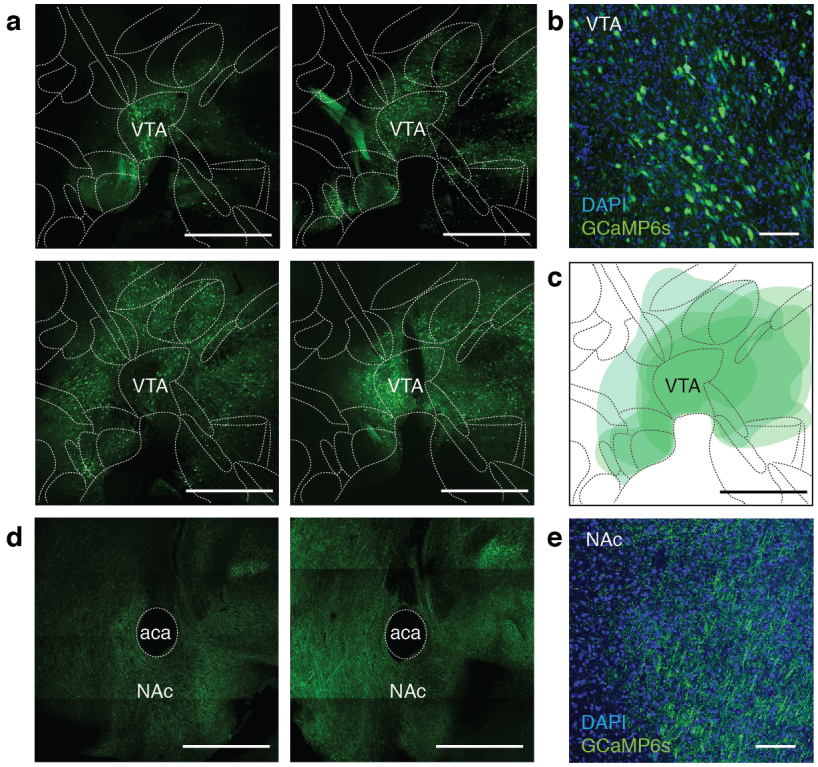

Figure 2-21: **GCaMP6s expression in the mouse brain** a-b, Representative low-magnitude (a) and high-magnitude (b) confocal images of GCaMP6s expression in VTA cell bodies (a: scale bar = 1 mm, b: scale bar = 200 μm). The experiment was repeated four times independently with similar results. c. The overlay of four confocal images with the histological brain image (black lines), which is reproduced from Paxinos and Franklin's the Mouse Brain in Stereotaxic Coordinates (Academic Press, 2019). d-e. Representative low-magnitude (d) and high-magnitude (e) confocal images of GCaMP6s expression in VTA-NAc axons (d: scale bar = 1 mm, e: scale bar = 200 μm).

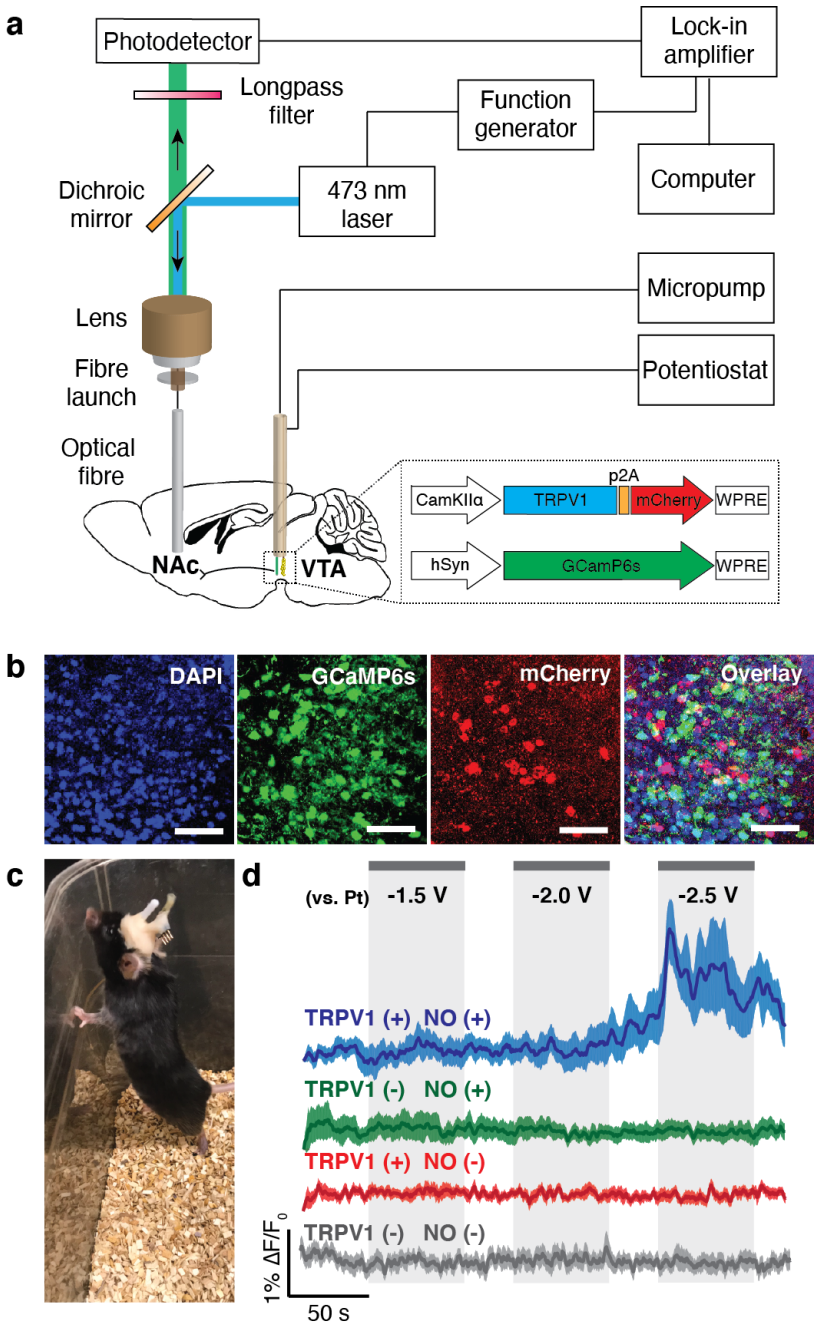

Figure 2-22: **In vivo fiber photometry results with NO-delivery fibers** a, An illustration of the fiber photometry setup integrated with the micropump and potentiostat for NO generation. b, Representative confocal microscope images of a mouse VTA co-expressing GCaMP6s and TRPV1-p2A-mCherry. Scale bar: 50 μm. The experiment was repeated three times independently with similar results. c, A mouse implanted with a NO-delivery fiber in the VTA and an optical fiber in the NAc. d, Normalized GCaMP6s fluorescence traces in the NAc of the anesthetized TRPV1$^+$ (blue) and TRPV1$^-$ (green) mice in the presence of NO generation and the NAc of TRPV1$^+$ (red) and TRPV1$^-$ mice (gray) in the presence of voltage alone (no $NaNO_2$ infusion). Solid lines and shaded areas indicate the mean and s.e.m., respectively (n = 5 mice per condition). F_0 indicates the mean of the fluorescence intensity during the initial 10 s of measurement.

2.6.3 Biocompatibility and Stability of Electrochemical NO Delivery Strategy

To evaluate the biocompatibility of our NO-delivery strategy in vivo, we investigated the interfaces between the brain tissue and the implanted fibers. Consistent with prior tissue analyses in the vicinity of polymer fibers [17, 40], NO-delivery fibers (400 μm in diameter) resulted in the significantly lower presence of astrocytes (as marked by glial fibrillary acidic protein, GFAP) and activated microglia (as marked by ionized calcium-binding adaptor molecule 1, Iba1) 7 days following implantation, as compared to the relatively smaller stainless steel microwires (300 μm in diameter). In the case of GFAP, the statistical difference between fiber and microwire groups was still observable 28 days following implantation, while there was no noticeable difference in Iba1 levels among groups following the same time period. Furthermore, we did not detect significant variations in levels of GFAP and Iba1 markers between the mice subjected vs not subjected to NO stimulation, likely due to the intermittent nature of NO release exclusively in the presence of applied voltage and the rapid decay of NO (Figure 2-23) [64]. In addition, no noticeable differences in cytotoxicity (and no observable deleterious effects on the local tissue) were observed between the VTA of mice subjected vs not subjected to NO generation as quantified by the cleaved caspase-3 assays (Figure 2-24). Finally, we confirmed that the Pt-Fe_3S_4 nanocatalysts, which did not evoke any observable cytotoxic responses in vitro or in vivo, remained stable at the surfaces of the cathodes two months following implantation into the mouse brain(Figure 2-25).

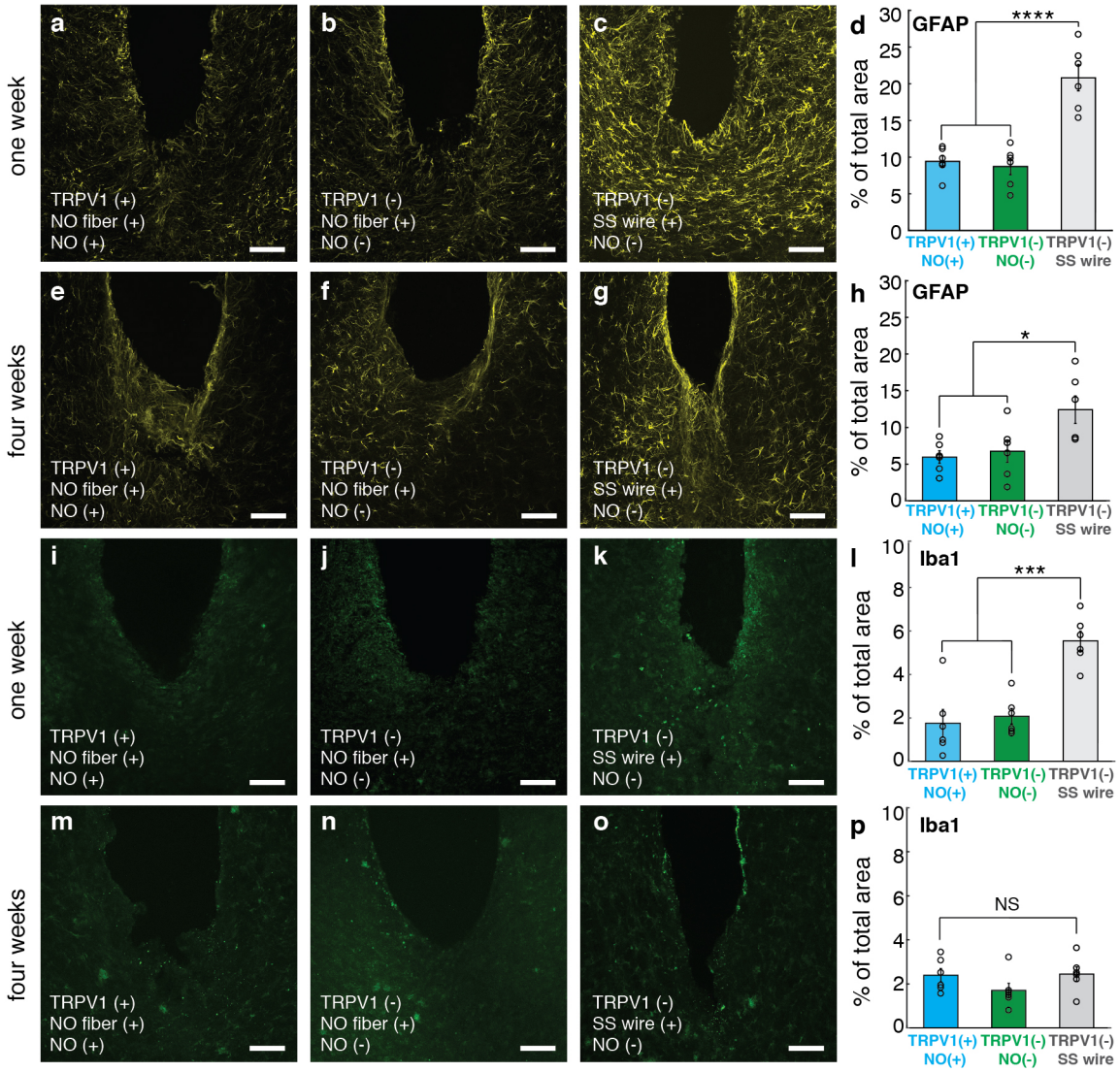

Figure 2-23: **Evaluation of GFAP and Iba1 expression levels at the interfaces between the brain tissue and the implanted fibers** a-h. Representative confocal images of the GFAP expression near the implantation site of TRPV1$^+$ mice subjected to NO stimulation and implantation of NO-delivery fiber (a,e), TRPV1$^-$ mice implanted with NO-delivery fiber without NO stimulation (b,f), and TRPV1$^-$ mice implanted with stainless steel wire without NO stimulation (c,g) 7 days (a-c) and 28 days (e-g) after implantation (scale bar = 100 μm). Percentages of the GFAP expressed area (mean ± s.e.m.) among the total area of the field 7 days (d) and 28 days (h) after implantation. i-p. Representative confocal images and average percentages of the Iba1 level near the implantation sites. Conditions are identical with a-h. One-way ANOVA and Tukey's multiple comparison tests were performed for d, h, and l, and p (n = 6 mice, GFAP: 7 days - $F_{2,15} = 27.54$, 28 days - $F_{2,15} = 5.75$, Iba1: 7 days - $F_{2,15} = 17.83$, 28 days - $F_{2,15} = 1.69$ * $p<0.05$, ** $p<0.01$, *** $p<0.001$, **** $p < 0.0001$).

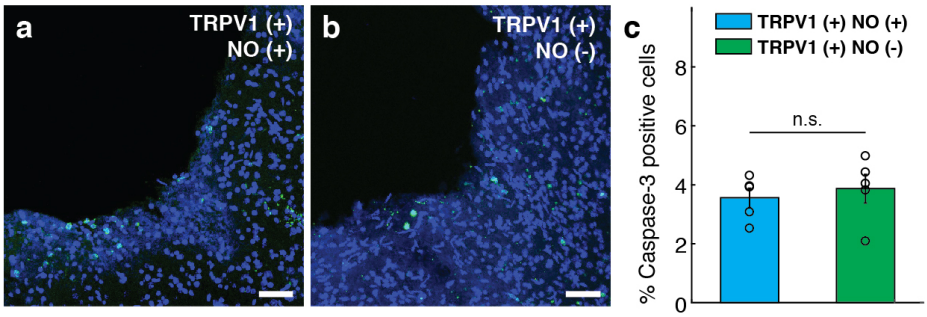

Figure 2-24: **Evaluation of cleaved caspase-3 positive cells at the interfaces between the brain tissue and the implanted fibers** a-b, Representative confocal images of cleaved caspase-3 positive cells (green) near the implantation site following NO generation (a) or after $NaNO_2$ injection without NO generation (b). Nuclear staining was performed with DAPI (blue). Scale bar: 50 μm. c, Percentages of cleaved caspase-3 positive cells among DAPI-labelled cells (mean $\pm$ s.e.m.) within 150 μm vicinity from the implantation site. No significant difference was found between the two groups, as assessed by one-tailed Student's t-test (n = 5 animals for each group, p = 0.612).

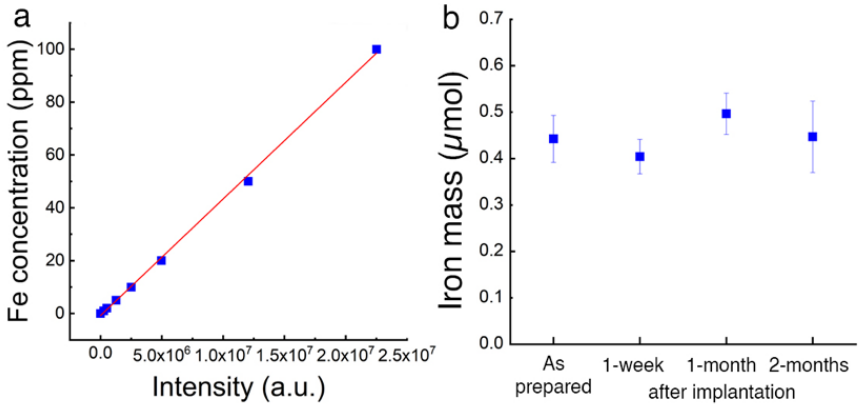

Figure 2-25: **Nanocatalyst physiological stability evaluation** Inductively coupled plasma - optical emission spectroscopy (ICP-OES) (PerkinElmer Optima 8000) was used to quantify the mass of iron on the implantable fibers. First, standard solutions, ranging between 1-100 ppm were prepared by diluting the ICP calibration standards (Sigma Aldrich). a, A linear fit was obtained after calibration. b, Based on the calibration curve, the iron mass on the cathode was calculated from ICP-OES spectra. Four groups of Pt-Fe_3S_4 loaded fibers were investigated; i) as-prepared fibers and the fibers explanted from the mouse brain ii) one-week, iii) one-month, iii) two months following implantation. Each error bar denotes the standard deviation of data.

2.7 Discussion and Conclusion

We have designed a strategy that enables the on-demand generation of NO, a lipophilic messenger in physiological processes including synaptic plasticity, vasodilation, and tumoricidal action of macrophages [41, 42], from the benign metabolite $NaNO_2$ by applying an electric field to electrochemically active nanocatalysts. This strategy affords in situ generation of NO with controllable release kinetics in the targeted regions. Furthermore, this electrocatalytic system was implemented in an implantable probe created via a multimaterial fiber drawing allowing for NO-mediated interrogation of neural circuits in vivo. Although demonstrated for activation of a particular NO-sensitive channel (TRPV1) in vivo, this electrochemical NO-delivery paradigm could be extended to target other NO-sensitive ion channels [28] and endogenous NO receptors [43, 77], advancing the mechanistic understanding of NO function in the nervous system and other organs.

Chapter 3

Electrochemical Modulation of Carbon Monoxide (CO)-Mediated Cell Signaling

3.1 Summary

This Chapter is based on J. Park et al., *Angew. Chem. Int. Ed.*, 2021 [78]

Despite the critical role played by CO in physiological and pathological signaling events, current approaches to deliver this messenger molecule are often accompanied by off-target effects and offer limited control over release kinetics. To address these challenges, we developed an electrochemical approach that affords on-demand release of CO through reduction of carbon dioxide (CO_2) dissolved in the extracellular space (Figure 3-1). Electrocatalytic generation of CO by cobalt phthalocyanine molecular catalysts modulates signaling pathways mediated by a CO receptor, soluble guanylyl cyclase. Furthermore, by tuning the applied voltage during electrocatalysis, we explore the effect of the CO release kinetics on CO-dependent neuronal signaling. Finally, we integrate components of our electrochemical platform into microscale fibers to produce CO in a spatially-restricted manner and to activate signaling cascades in

the targeted cells. By offering on-demand local synthesis of CO, our approach may facilitate the studies of physiological processes affected by this gaseous molecular messenger.

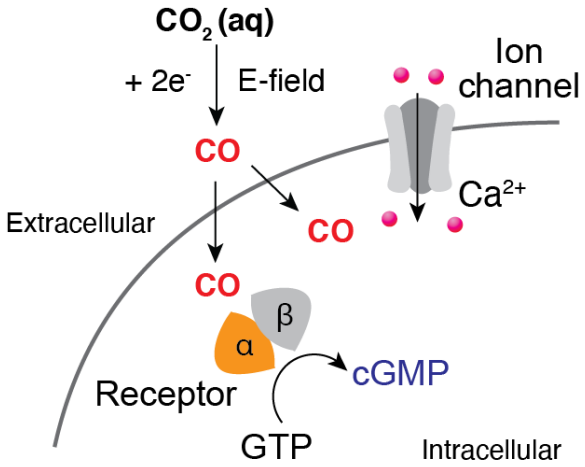

Figure 3-1: **A schematic illustrating electrochemical generation of CO for modulating signaling cascades**

3.2 Background and Motivation

3.2.1 Electrochemical Carbon Dioxide Reduction Reaction

Electrochemical reduction of CO_2 has been extensively studied to produce valuable chemicals fuels from atmospheric CO_2. Diverse carbon compounds can be electrochemically generated from CO_2 through proton-coupled electron transfer processes as follows (Equation3.1) [79]:

$$\begin{aligned} CO_2 + H_2O + 2e^- &\longleftrightarrow CO + 2OH^- \\ CO_2 + 6H_2O + 8e^- &\longleftrightarrow CH_4 + 8OH^- \\ 2CO_2 + 8H_2O + 12e^- &\longleftrightarrow C_2H_4 + 12OH^- \\ 2CO_2 + 9H_2O + 12e^- &\longleftrightarrow C_2H_5OH + 12OH^- \\ 3CO_2 + 13H_2O + 18e^- &\longleftrightarrow C_3H_7OH + 18OH^- \end{aligned} \tag{3.1}$$

The selectivity of the electrochemical reduction products in aqueous solutions can be controlled with the applied voltages. For example, it has been reported that the reduction products on Cu electrode can be greatly changed depending on the applied voltage: CO production is favourable at less negative voltages whereas CH_4 becomes the major reaction product at higher negative voltages [80]. Additionally, the binding energies of the intermediate species to the surface of the electrocatalysts (metallic electrodes or molecular complexes) can also influence the product selectivity of CO_2 reduction reaction. For example, CO generation is favorable in electrocatalysts having a lower binding energy to CO molecules, such as Au and Ag, since CO can be easily released from the surface of the electrocatalysts without further electrochemical reduction [81].

3.2.2 Motivation

CO is a gaseous and transmembrane diffusible messenger affecting numerous physiological and pathological processes, including vasoactive response, neurotransmission, and inflammation [82–86]. To understand the physiological effects of CO and poten-

tially harness them in a therapeutic context, prior work has explored direct delivery of CO gas via respiratory administration [83, 87]. However, this approach does not permit targeting of CO to specific tissues or organs and poses a risk of a global increase in carboxyhemoglobin levels manifesting in CO poisoning [83, 88–90]. Consequently, CO-releasing molecules (CORMs), which release CO as a free gas or transfer it to biological molecules, have been designed for targeted delivery of CO [91–95]. However, it remains challenging to tune CO-release kinetics of CORMs without modifying their molecular structures, and thus multiple CORMs are necessary for applications demanding variable CO release kinetics [83, 92, 94, 95]. Moreover, degradation of inherently unstable CORMs during delivery limits precision of CO dosing often leading to off-target release beyond tissues of interest [88]. Therefore, there is a demand for systems enabling on-demand synthesis of CO with controllable release kinetics.

3.3 Electrochemical System for In Situ CO Delivery

To address this need, we developed a system that enables on-demand synthesis of CO through electrochemical CO_2 reduction reaction (Figure 3-2a). By leveraging a selective catalyst cobalt phthalocyanine (CoPc) [96–98], CO_2 dissolved in the extracellular solution can be reduced to CO at the cathode (Figure 3-2b). Due to its high solubility ($\sim$ 34 mM) in water, dissolved CO_2, which exists in equilibrium with bicarbonate buffer [97, 99, 100], serves as a precursor for electrochemical formation of CO. Electrochemically produced CO is shown to modulate diverse CO-dependent cell signaling processes in vitro. Furthermore, CO release kinetics can be controlled by varying the cathode voltage. This tunability of CO release kinetics enabled systematic investigation of neuronal signaling mediated by this molecule. Finally, we demonstrate microscale, CO-releasing electrocatalytic fibers as tools to locally activate cell signaling.

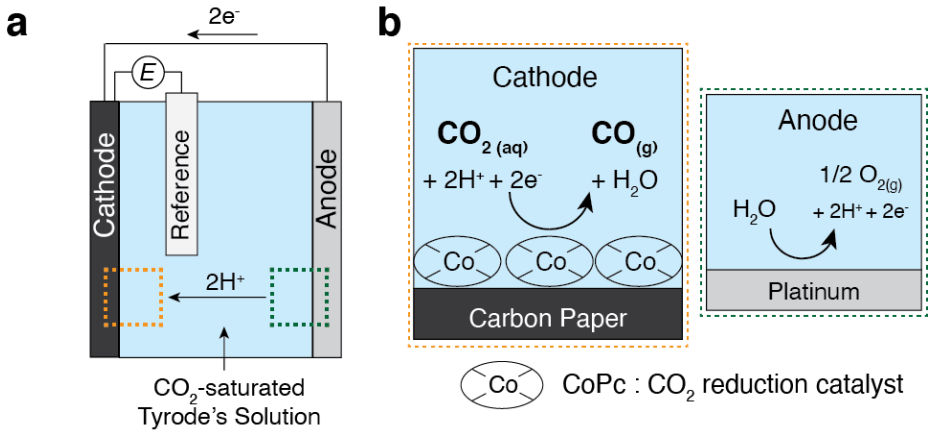

Figure 3-2: **Electrocatalytic synthesis of CO from CO_2 dissolved in extracellular solution** a, A schematic illustrating the electrochemical system for in situ CO delivery. b, An illustration of the electrochemical reactions at the CoPc/OxCP cathode and Pt anode.

3.3.1 Electrocatalytic Activities of Cobalt Phthalocyanine

CoPc loaded cathodes were prepared by drop-casting CoPc ink ($\sim$ 1 mg/ml) onto the oxygen-functionalized carbon paper (OxCP). The electrocatalytic activities of CoPc/OxCP cathodes were evaluated in a three-compartment electrochemical cell

containing physiological solution (Tyrode's) saturated with CO_2 at pH 7.4. Pt and Ag/AgCl electrodes were employed as anode and reference electrodes, respectively (Figure 3-2). CV profiles of CoPc/OxCP in CO_2-saturated Tyrode's solution showed higher reductive currents as compared with those recorded in N_2-saturated solution (Figure 3-3a).

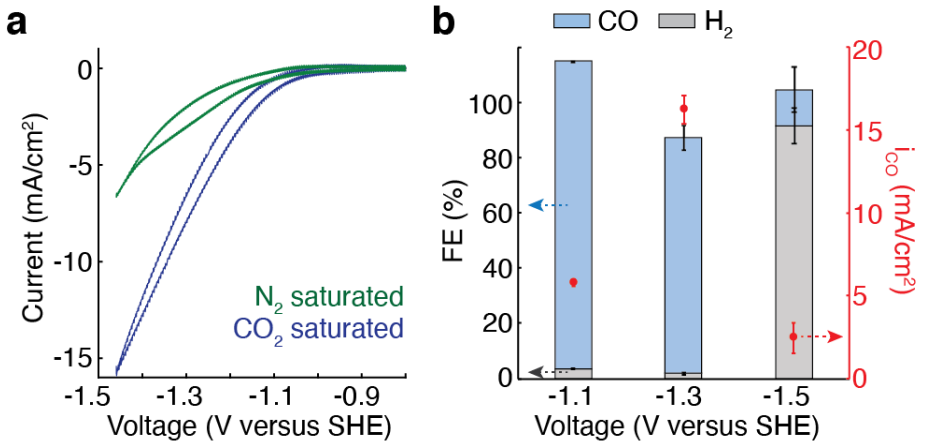

Figure 3-3: **Electrocatalytic activities of CoPc/OxCP electrodes in extracellular solution** a, CV curves of CoPc/OxCP electrodes in CO_2- (blue) or N_2- (green) saturated Tyrode's solution at pH 7.4 (scan rate, 100 mV/s). b, The Faradaic efficiency (FE) for CO and H_2, and partial current density of CO (i_{CO}) (mean ± standard error of the mean (s.e.m.), n = 3) at various applied voltages.

3.3.2 Analysis of Electrochemical Reaction Products

The cathodic products in CO_2-saturated Tyrode's solution were analyzed by chronoamperometry across a range of applied voltages. The cathodes exhibited high selectivity toward CO up to –1.3 V versus standard hydrogen electrode (SHE), and partial current density of CO increased as we applied more reductive potentials to the cathodes at this voltage range. Negligible amounts of H_2, a side product at the cathodes, were generated at identical reaction conditions with the Faradaic Efficiencies (FE) in the range of 1.8-3.4 % (Figure 3-3b). At higher negative voltages ($\leq$ –1.5 V), hydrogen evolution reaction dominated over CO_2 reduction reaction (Figure 3-3b). At Pt anodes, oxygen evolution was predominately found with a minor chlorine evolution (Figure 3-4). Together, these data indicated that CO can be electrochemically gen-

erated from CO_2 dissolved in Tyrode's solution with high selectivity, and CO release kinetics can be controlled via applied voltage.

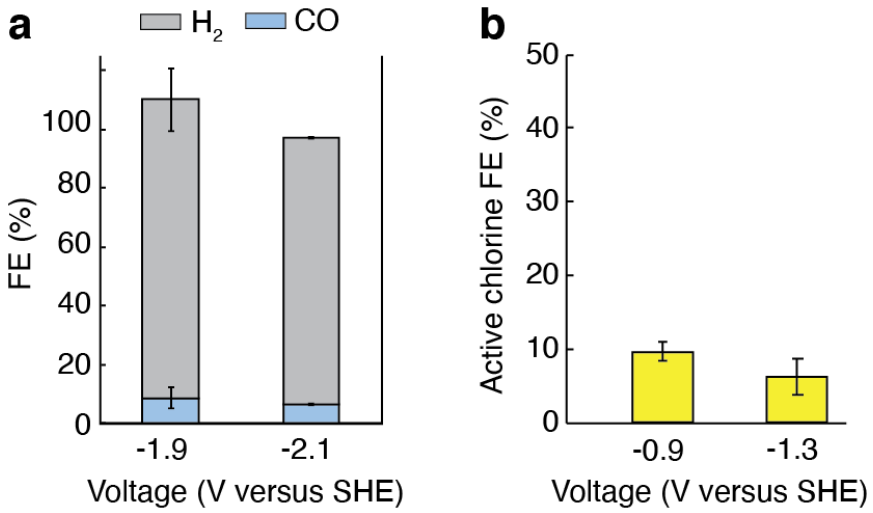

Figure 3-4: **Analysis of electrochemical reaction products at various applied voltages** a, The Faradaic efficiency (FE) for H_2 and CO (mean ± standard error of the mean (s.e.m.), n = 3) at negative voltages –1.5 V. Notably, the degradation of CoPc catalyst was also observed in this potential range over time. b, Faradaic efficiency for active chlorine produced at the Pt anode in CO_2-saturated Tyrode's solution (pH 7.4). Quantification of active chlorine was conducted using N,N-diethyl-p-phenylenediamine (DPD)-based active chlorine test

3.4 Control of Signaling Pathways with Electrochemical CO Generation

3.4.1 Endogenous CO-sGC-cGMP Pathway

To illustrate the utility of our electrochemical system for modulating CO-dependent signaling, we first applied it to activate sGC, one of the well-characterized receptors of CO [101–103]. It was previously shown that CO can bind to the heme moiety in sGC, activating the catalytic conversion of guanosine 5' triphosphate (GTP) to the second messenger cGMP [101–103]. To elicit robustly measurable cGMP formation, human embryonic kidney (HEK) 293 FT cells were co-transfected with two plasmids carrying DDK-tagged α- and DDK-tagged β-subunits of human sGC under the broad mammalian cytomegalovirus (CMV) promoter, respectively. The expression of these subunits in the cells was confirmed by immunostaining with anti-DDK antibodies (Figure 3-5a). Consistent with previous reports [104, 105], cells overexpressing both subunits (sGC^+ cells) exhibited substantially higher basal cGMP levels ($\sim$300 fold) as compared to unmodified cells only expressing low levels of endogenous sGC. In contrast, no noticeable increases in the cGMP levels were found after transfection of cells with either α-subunit or β-subunit alone (Figure 3-5b). When exposed to NO, a highly potent activator of sGC [20, 84], robust increase in cGMP levels ($\sim$20 fold) was found in sGC^+ cells, confirming the functionality of the genetically introduced sGC (Figure 3-6).

We next investigated whether electrochemically synthesized CO could activate sGC-cGMP signaling pathways (Figure 3-7a). We first confirmed that CoPc catalysts did not elicit any cytotoxic responses in HEK cells. Similarly, negligible cytotoxic responses were found in cells following acute exposure to CO_2-saturated Tyrode's solution (Figure 3-8). Additionally, we confirmed that the concentration of dissolved CO_2 at the bottom of the well plate, where sGC^+ cells were located, remained largely constant over 30 min in the absence of continuous CO_2 purging (Figure 3-9). CO produced at the CoPc/OxCP cathodes at –1.3 V versus SHE in CO_2-saturated Ty-

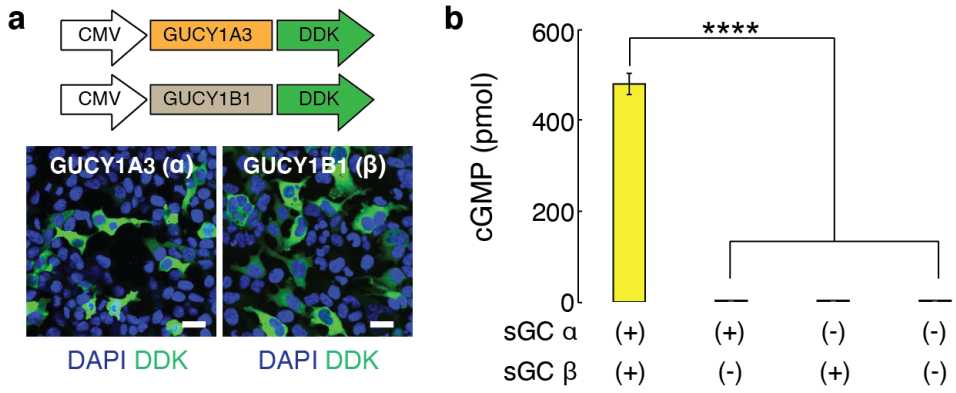

Figure 3-5: **Intracellular cGMP levels in HEK cells overexpressing sGC subunits** a, Representative confocal images of HEK cells transfected with DDK-tagged α-subunit of sGC or DDK-tagged β-subunit of sGC under the CMV promoter (scale bar, 50μm). b, Intracellular cGMP levels (mean ± s.e.m.) in 10^6 HEK cells 48 h after the transfection (n = 6, one-way analysis of variance (ANOVA) and Tukey's multiple comparison test, $F_{3,20}$ = 392.2, **** $p = 1.1 \times 10^{-16} < 0.0001$).

rode's solution at pH 7.4 led to a moderate increase in cGMP levels (∼150 %) in sGC^+ cells. To investigate whether the observed increase in cGMP is attributable to electrochemically formed CO, we recorded the cGMP levels in control groups, which included sGC^+ cells immersed in CO_2-saturated Tyrode's solution in the absence of an applied voltage and in the cells immersed in a solution not saturated in CO_2 in the presence of an applied voltage (–1.3 V versus SHE). Consistent with prior studies that found no changes in cGMP levels upon CO_2 delivery [106], no substantial increases in cGMP levels were observed in our control groups, indicating that electrochemically formed CO was responsible for sGC activation (Figure 3-7b).

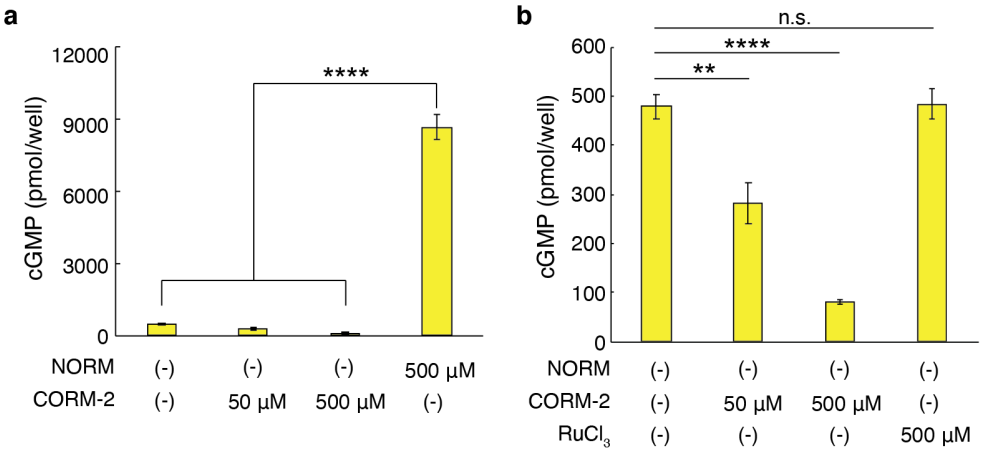

Figure 3-6: **Enhanced cGMP levels in HEK cells overexpressing sGC subunits after the addition of NO and CO donor solutions** a, Intracellular cGMP levels (mean ± s.e.m.) in 10^6 sGC^+ HEK cells following the addition of NORM (500 μM, DEA NONOate) or CORM-2 (50 μM, 500 μM). The statistical significance of an increase in cGMP levels after NO delivery was confirmed by one-way ANOVA and Tukey's multiple comparison test (n = 6, $F_{3,20} = 261.3$, ** $p = 3.3 \times 10^{-16} < 0.0001$). b, Intracellular cGMP levels (mean ± s.e.m.) in 10^6 sGC^+ HEK cells after the addition of CORM-2 (50 μM, 500 μM) or $RuCl_3$ (one-tailed Student's t-test, n = 6, ** $p = 0.003 < 0.01$, **** $p = 3.3 \times 10^{-6} < 0.0001$, and n.s. $p = 0.46 > 0.05$). Unlike electrochemically produced CO, CORM-2 failed to increase the cGMP levels in sGC^+ cells, presumably due to its NO scavenging activity.

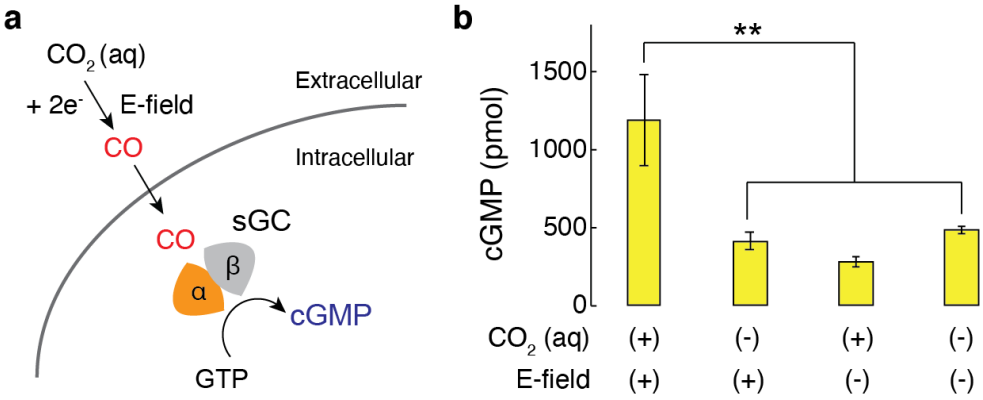

Figure 3-7: **Activation of sGC-cGMP signaling pathways with electrochemically produced CO** a, A schematic illustrating activation of sGC mediated by electrochemically produced CO. GTP, guanosine 5' triphosphate. b, Intracellular cGMP levels (mean ± s.e.m.) in 10^6 sGC^+ cells following CO delivery driven by CoPc/OxCP cathodes at –1.3 V versus SHE for 10 min. The statistical significance of an increase in cGMP levels after electrochemical CO delivery as compared with controls was assessed by one-way ANOVA and Tukey's multiple comparison test (n = 6, $F_{3,20} = 7.4$, ** $p = 0.0016 < 0.01$).

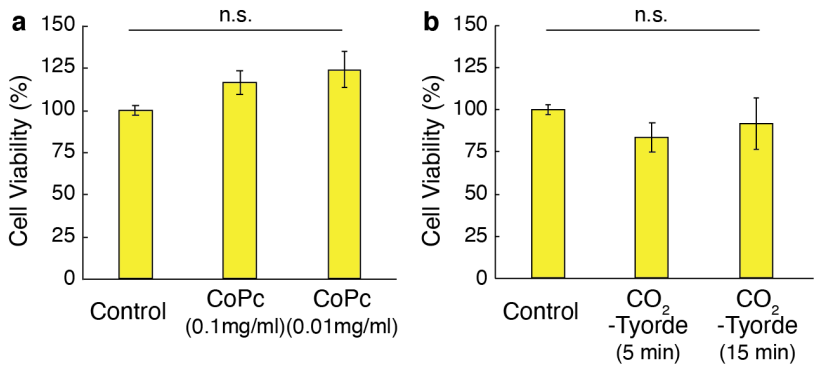

Figure 3-8: **Cell viability assay results showing negligible cytotoxic effects from CoPc or dissolved CO_2** a, Cell viability in the presence or absence of CoPc (mean ± s.e.m.). No statistically significant differences were observed between groups as identified by one-way ANOVA and Tukey's multiple comparison test (n = 7, $F_{2,18} = 2.72$, p = 0.093). b, Cell viability following acute exposure to CO_2-satuated Tyrode's solution at pH 7.4 (mean ± s.e.m.). No statistically significant differences were observed between groups as identified by one-way ANOVA and Tukey's multiple comparison test (n = 5, $F_{2,12} = 0.62$, p = 0.55).

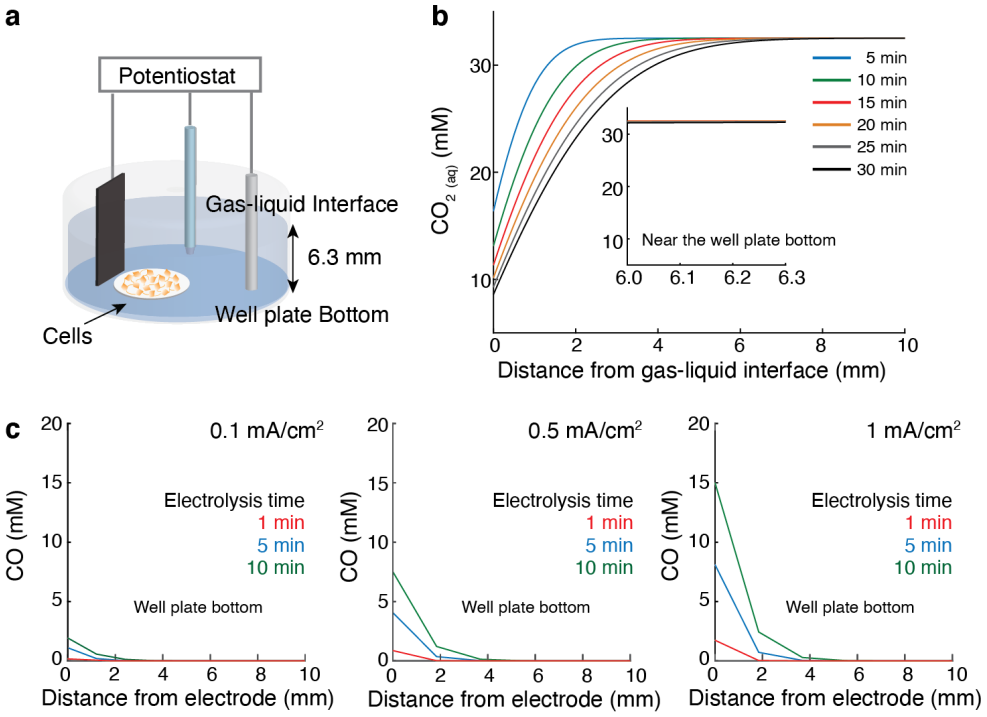

Figure 3-9: **Calculated CO_2 degassing and CO release kinetics from the CoPC/OxCP electrodes** a, A schematic illustrating an experimental setup for CO delivery to cells. b, Calculated CO_2 concentration profiles as a function of distance from gas-liquid interface considering CO_2 degassing kinetics. Inset shows negligible changes in CO_2 concentration near the cells c, Diffusion profile of electrochemically generated CO at various current densities and electrolysis time.

3.4.2 CO effects on NO-sGC-cGMP Pathway

Furthermore, electrochemically synthesized CO was sufficient to modulate the NO-mediated sGC-cGMP signaling in sGC^+ cells (Figure 3-10a). It has been previously proposed that CO, a weaker activator of sGC as compared to NO, could attenuate NO-mediated cGMP increases by competing for the same binding site (heme moiety of sGC) with NO [84, 107]. Indeed, inhibitory effects of CO on NO-mediated sGC activation were found in a number of organs, including the cerebellar cortex, retina, and resistance arteries [108–110]. Consistent with these prior studies [84, 107], we observed noticeable decreases in NO-stimulated cGMP levels (~60 %) in sGC^+ cells following addition of 500 μM CORM-2 (tricarbonyldichlororuthenium(II) dimer), a molecular CO donor. Similarly, CO synthesized at CoPc/OxCP cathodes in CO_2-saturated Tyrode's solution led to attenuation in NO-mediated cGMP production (~70 %) (Figure 3-10b). These results suggested that the electrocatalytic CO-delivery approach could be extended to regulate diverse sGC-mediated signaling pathways.

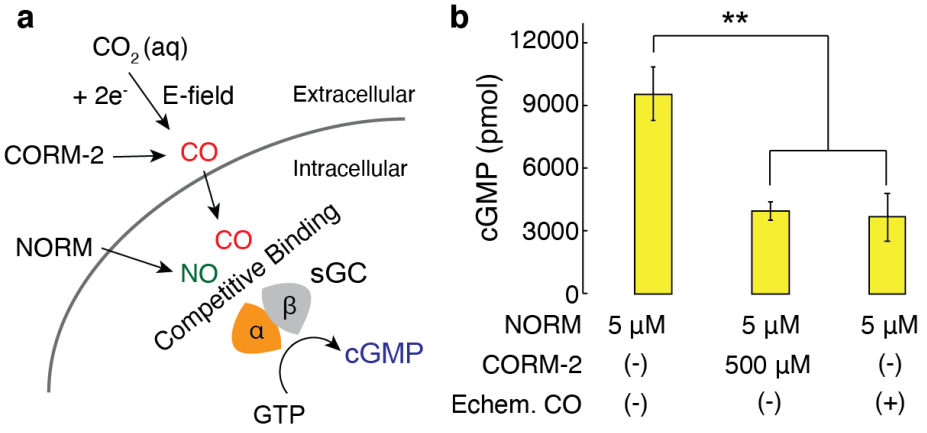

Figure 3-10: **Electrochemically released CO regulates NO-sGC-cGMP signaling pathways** a, An illustration of NO-sGC-cGMP signaling pathways modulated by CO. NORM, NO releasing molecule. b, Intracellular cGMP levels (mean ± s.e.m.) in 10^6 sGC^+ cells following NO delivery in the presence or absence of CO (n = 5, one-way ANOVA and Tukey's multiple comparison test, $F_{2,12} = 10.9$, ** $p = 0.002 < 0.01$).

3.4.3 CO-dependent Ca^{2+} Signaling in Neurons

We next evaluated whether our electrochemical system can be applied to interrogate CO-dependent signaling in neurons. Among the diversity of brain regions, hippocampus neurons have been shown to express high levels of heme oxygenase, which produces endogenous CO, implying that CO could play a critical role in hippocampal physiology [82,111]. Indeed, it has been reported that both endogenous and exogenous CO can trigger a myriad of processes in the hippocampus, including apoptosis, long-term potentiation, and expression of immediate early genes [3, 112, 113]. Thus we adopted hippocampal neurons as test beds for the CO-dependent signaling in neurons, and CO-triggered neuronal activity was recorded using an intracellular Ca^{2+} indicator fluo-4 as a proxy for neuronal membrane depolarization [114].

The effects of exogenous CO on hippocampal neurons were first investigated using CORM-2. When exposed to CORM-2 (50 μM), the normalized fluo-4 fluorescence ($\Delta F/F_0$) in hippocampal neurons gradually increased over time indicating Ca^{2+} influx into these cells, whereas the addition of an inactive form of CORM-2, $RuCl_3$, did not evoke any comparable fluorescence changes in neurons (Figure 3-11a,b). Addition of lower concentration of CORM-2 (from 1 to 10 μM) led to smaller Ca^{2+} influxes in neurons, indicating that observed Ca^{2+} signaling were predominantly triggered by CORM-2 (Figure 3-11c).

To investigate the biological mechanisms underlying the effects of CO-mediated Ca^{2+} influxes in neurons, we employed blockers (or inhibitors) of ion channels and receptors that have been previously proposed as molecular targets of CO_2 [115–117]. The latter included large-conductance, voltage- and Ca^{2+}-activated K+-channel (BK_{Ca}), L-type Ca^{2+}-channel, hyperpolarization-activated cyclic nucleotide-gated channel (HCN), and sGC. Among blockers (or inhibitors) of the putative CO targets, L-type Ca^{2+} channel blocker nitrendipine [118] significantly attenuated Ca^{2+} responses driven by CORM-2 (Figure 3-11d, Figure 3-12). Although the understanding of the mechanisms contributing to the CO-mediated Ca^{2+} increases in neurons continues to evolve [115], our findings suggest that observed Ca^{2+} responses are at least partially

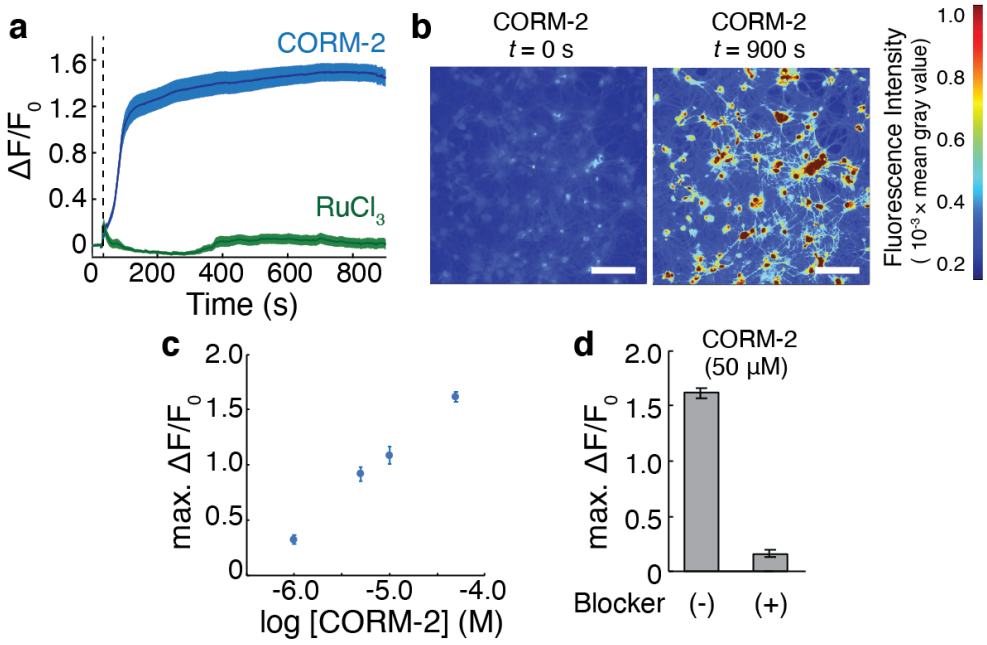

Figure 3-11: **Ca^{2+} responses in hippocampal neurons after the addition of CO donor solutions** a, Averaged fluo-4 fluorescence traces for hippocampal neurons (n = 100 neurons for each trace) following 50 μM CORM-2 (blue) or 50 μM $RuCl_3$ (green) infusion at 30 s (dashed lines). The solid lines and shaded areas represent the mean and s.e.m., respectively. b, Time-lapse images of Ca^{2+} responses in response to CORM-2 infusion (scale bar, 50μm). c, CORM-2 concentration-dependent maximum of normalized fluo-4 fluorescence change averaged across 100 neurons. d, Maximum of normalized fluo-4 fluorescence increases in 100 neurons following the infusion of 50 μM CORM-2 in the presence or absence of L-type Ca^{2+} channel blocker nitrendipine.

related to the interactions between CO and L-type Ca^{2+} channels.

We then applied our electrochemical CO-delivery system to similarly evoke Ca^{2+} responses in hippocampal neurons (Figure 3-13a). Here, CoPc/OxCP cathode, Pt anode, and Ag/AgCl reference electrode were utilized to deliver CO to neurons in CO_2-saturated Tyrode's solution at pH 7.4. Because the local CO concentration is calculated to be much lower at greater distances from the cathode (Figure 3-9), we positioned the CoPc/OxCP cathode in the immediate vicinity of the neurons (Figure 3-13b). Robust Ca^{2+} responses (as marked by $\Delta F/F_0 \geq 25\%$) in neurons were observed 250 s after application of –1.3 V versus SHE, and continued application of –1.3 V to the cathode led to Ca^{2+} influxes in neurons located at greater distances from the cathode (Figure 3-13c). To assess whether observed Ca^{2+} responses were attributable to CO released from the cathodes, we recorded Ca^{2+} changes in control

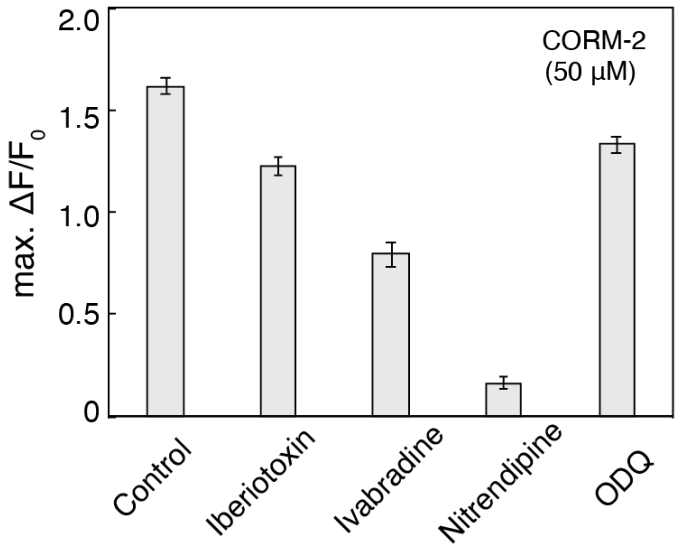

Figure 3-12: **Effects of ion channel blockers, inhibitors on CO-mediated neuronal Ca^{2+} responses** Maximum of the normalized fluo-4 fluorescence changes in 100 neurons following the addition of 50 μM CORM-2 in the presence or absence of ion channel blockers (or inhibitors): 20 μM Iberiotoxin for BK_{Ca} channel; 12 μM Nitrendipine for L-type Ca^{2+} channel; 400 μM Ivabradine for HCN; 10 μM 1H-[1,2,4]oxadiazolo[4,3-a]quinoxalin-1-one (ODQ) for sGC.

experiments, which included neurons immersed in CO_2-saturated Tyrode's solution with no voltage applied (Figure 3-14a) and in neurons immersed in Tyrode's not saturated in CO_2 in the presence of a cathodic bias (–1.3 V versus SHE,(Figure 3-14c)). The extent of Ca^{2+} responses found in the control experiments was significantly lower than that triggered by electrochemically formed CO (Figure 3-14a). Moreover, Ca^{2+} increases in response to CO released from the cathode were largely inhibited by the addition of L-type channel blocker nitrendipine, akin to our observations with CORM-2 (Figure 3-11d). These results suggested that Ca^{2+} responses observed in neurons are predominately mediated by electrochemically produced CO.

Our electrochemical approach further enabled an investigation of CO-mediated neuronal signaling at different CO release kinetics. When we applied –0.9 V versus SHE to the cathodes in CO_2-saturated Tyrode's solution, only 13% of neurons exhibited robust Ca^{2+} responses (as marked by $\Delta F/F_0 \geq 50\%$) (Figure 3-14d). In contrast, 91% of neurons responded at –1.3 V (Figure 3-14a) due to faster CO release kinetics at this voltage as compared to –0.9 V (Figure 3-3a). Despite the higher Faradaic

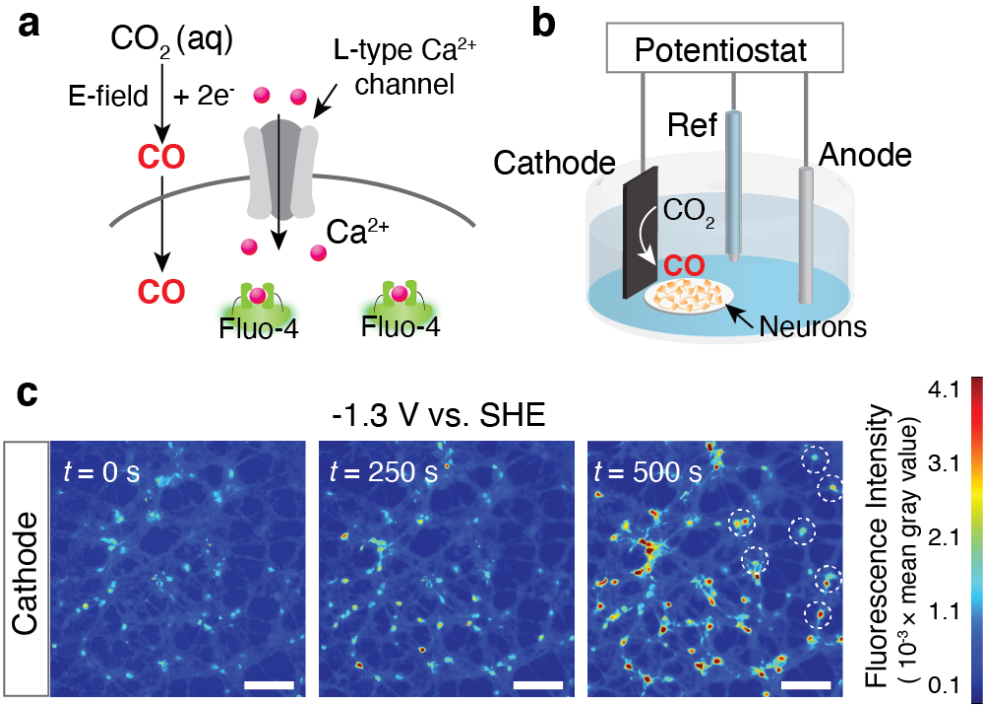

Figure 3-13: **Neuronal Ca^{2+} responses triggered by electrocatalytic CO release** a, A schematic illustrating a potential mechanism of CO-mediated Ca^{2+} responses in neurons through L-type Ca^{2+} channel. b, Experimental scheme for electrochemical CO delivery to neurons. c, Time-lapse images of Ca^{2+} increases in neurons triggered by CO produced from CoPc/OxCP cathodes, which were positioned at the left edge in all three images, at –1.3 V versus SHE (scale bar, 50μm). Neurons located at greater distances from the cathode responded over time (white dotted circles).

current, a smaller fraction of neurons showed Ca^{2+} responses at –1.7 V as compared to –1.3 V (Figure 3-14e). This observation is consistent with the extremely low CO selectivity of CoPc/OxCP catalysts at this reductive voltage (Figure 3-3b, Figure 3-4). By controlling CO generation kinetics with applied voltage, we found that CO release kinetics, not Faradic current, is the key factor affecting CO-mediated Ca^{2+} responses in neurons.

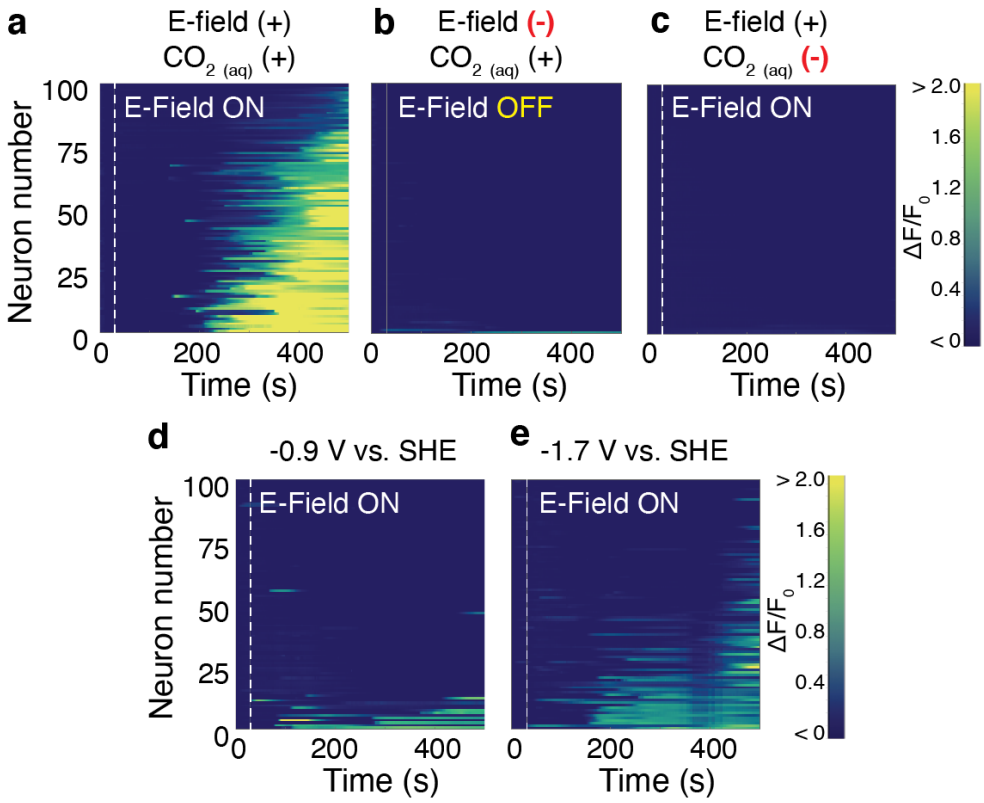

Figure 3-14: **Investigation of Ca^{2+} responses in neurons at various CO release kinetics** a-c, Individual fluo-4 fluorescence traces for 100 neurons at different experimental conditions. E-field (–) in (b) represents neurons immersed in CO_2-saturated solution in the absence of an applied voltage. CO_2(aq) (–) in (c) represents neurons immersed in Tyrode's not saturated in CO_2 in the presence of an applied voltage. Voltage of –1.3 V were turned on at 30 s (dashed lines) in a and c. d-e, Individual fluo-4 fluorescence traces for 100 neurons after electrochemical CO generation at –0.9 V (d) and –1.7 V versus SHE (e). Voltages were turned on at 30 s (dashed lines).

3.5 Microscale, CO-releasing Electrocatalytic Fibers

3.5.1 Fabrication of CO-releasing Fibers with Fiber Drawing Process

Finally, we miniaturized our electrochemical system by leveraging fiber drawing [17, 20]. Fiber-based fabrication allowed us to scale down macroscale components of an electrochemical cell into a microscopic electrocatalytic fiber (Figure 3-15a-d). A polycarbonate-based macroscopic preform, which contained two grooves on its surface for placing microelectrodes and one hollow channel for delivering CO_2-saturated solution, was fabricated through macroscale machining (Figure 3-15b). During drawing, the preform was heated and stretched into a microscale fiber (Figure 3-15c,d). Carbon nanotube (CNT) and Pt microwires (50 μm in diameter) were then placed into grooves on the surface of the fiber. The microwires extended from the fiber tips by approximately 300 μm, and CoPc ink was deposited onto the CNT microwires. The non-exposed region of the microwires was then fully coated with epoxy that provided electrical insulation and mechanical stability, and the microwires and the microfluidic channel were interfaced with electrical pin connectors and tubing inlets, respectively (Figure 3-15e, Figure 3-16a). We confirmed that CO_2-saturated Tyrode's solution can be delivered through the microfluidic channel integrated within the electrocatalytic fiber (Figure 3-16b). CoPc/CNT microwires, which served as cathodes integrated within the fibers, catalyzed CO_2 reduction reaction, as confirmed by chronoamperometry analyses (Figure 3-16c). Integrated Pt microwires served as anodes during the reaction.

3.5.2 Modulation of CO-mediated Signaling at the Microscale

The electrocatalytic fibers were then applied to locally deliver CO and evoke CO-mediated sGC-cGMP signaling cascades in the targeted cells. To monitor local cGMP dynamics, HEK cells were transfected with a plasmid carrying a genetically encoded fluorescent cGMP sensor, Green cGull [119], under the CMV promoter. The func-

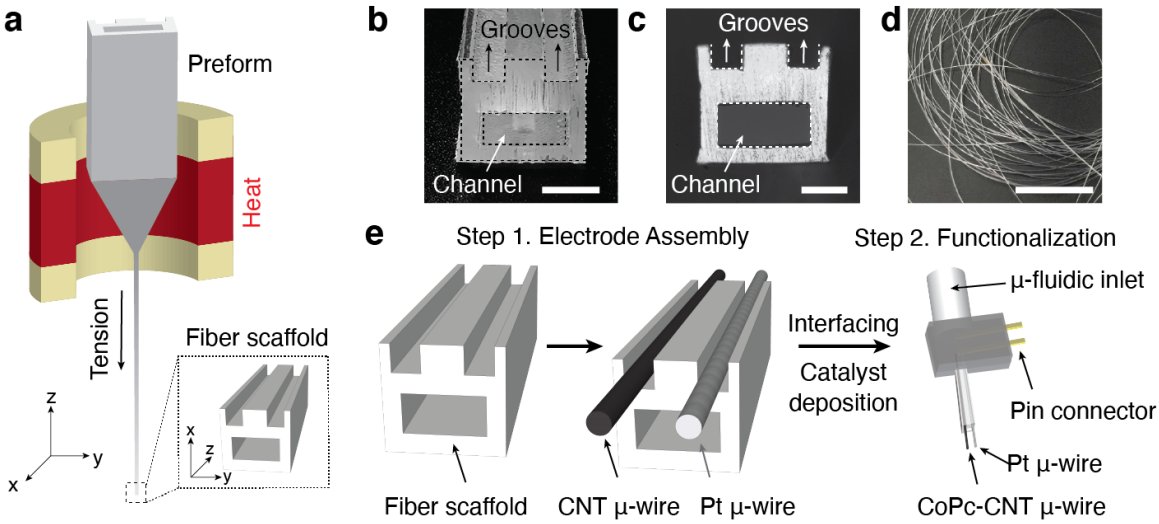

Figure 3-15: **Design and fabrication of CO-release fibers** a, A schematic illustrating the fiber drawing procedure. b-c, Cross-sectional images of the preform (b, scale bar, 5 mm) and the fiber scaffold after the drawing process (c, scale bar, 100 μm). Two microscale grooves and one hollow microchannel are visible in c. d, A photograph of a bundle of fiber scaffolds after the drawing process (scale bar, 5 cm). e, A schematic demonstrating microelectrode assembly on the fiber scaffold, followed by fiber connectorization and functionalization of the CNT microwires with CoPc catalyst.

tionality of Green cGull expressed in cells was first confirmed with a NO releasing molecule (NORM). After delivery of CO_2-saturated Tyrode's solution, CO was generated from the CoPc-CNT microwires at –1.3 V versus SHE. A gradual increase in Green cGull fluorescence (a marker of cGMP accumulation) was found in cells located in the proximity of the microwires (Figure 3-17a,b). In contrast, no noticeable Green cGull fluorescence changes were found in cells after delivery of CO_2-saturated solution in the absence of an applied voltage or in cells subjected to electric stimulation in the absence of CO_2 precursor (Figure 3-17b).

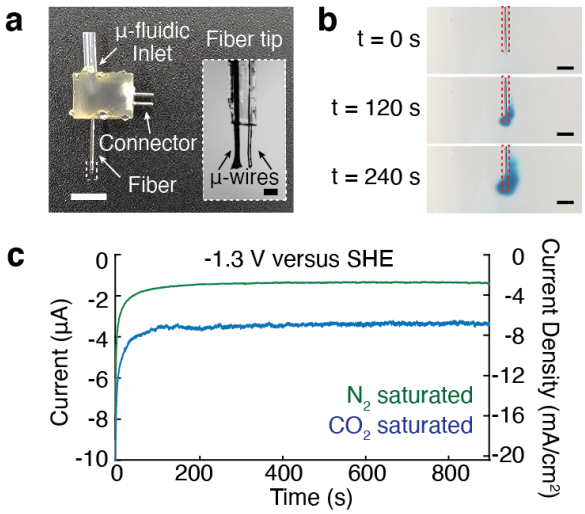

Figure 3-16: **Characterization of CO-release fibers** a, A photograph of the resulting CO delivery fiber (scale bar, 5 mm) and a microscope image of the fiber tip (inset, scale bar, 100μm). b, Delivery of CO_2-saturated Tyrode's solution with a dye (BlueJuice) into a brain phantom (0.6% agarose gel) through the microfludic channel within the fiber at an infusion rate of 100 nL/min (scale bar, 500μm). c, Chronoamperometry measurements conducted with the electrocatalytic fiber in CO_2-saturated (blue) or N_2-saturated (green) Tyrode's solution at pH 7.4.

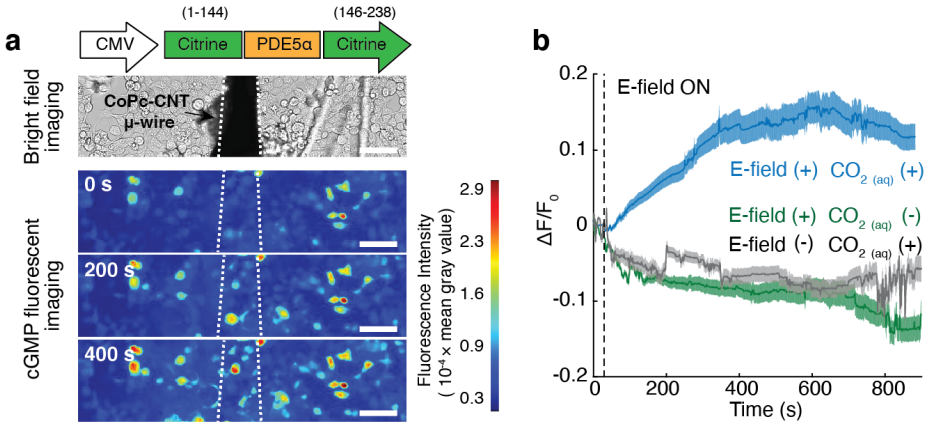

Figure 3-17: **Activation of sGC with CO-release fibers at the microscale** a, An optical image of a CoPc-CNT microwire of the CO-delivery fiber positioned above Green cGull-expressing cells (top). Time-lapse images of local cGMP dynamics in Green cGull-expressing cells in response to electrochemically synthesized CO from the CoPc-CNT microwire (white dotted lines) at –1.3 V versus SHE (scale bar, 50μm) (bottom). b, Averaged Green cGull fluorescence traces of cells (n = 100 cells for each trace) at different experimental conditions. The solid lines and shaded areas indicate the mean and s.e.m., respectively. E-field (–) and CO_2(aq) (–) indicate cells after delivery of CO_2-saturated solution in the absence of an applied voltage and cells subjected to cathodic voltage without CO_2 saturation, respectively. Voltages of –1.3 V were turned on at 30 s (dashed lines).

3.6 Discussion and Conclusion

By leveraging electrocatalytic activity and selectivity of CoPc catalysts toward reduction of CO_2 into CO at modest voltages, we have developed an electrochemical approach for in situ targeted delivery of this molecule to physiological environments. Electrochemically released CO from CoPc-functionalized cathodes was shown to modulate several sGC-mediated signaling cascades in cells. Furthermore, facile control over CO release kinetics in our platform enabled a systematic investigation of CO-mediated signaling in neurons. This electrochemical system was further implemented in microscale fibers produced via thermal drawing. CO generated from the electrocatalytic fibers evoked local cGMP accumulation in the targeted cells. We envision that our electrochemical approach can be extended to explore CO-mediated cellular signaling in diverse systems, including the peripheral nervous system (Figure 3-18), offering addition insights onto its role as a messenger molecule.

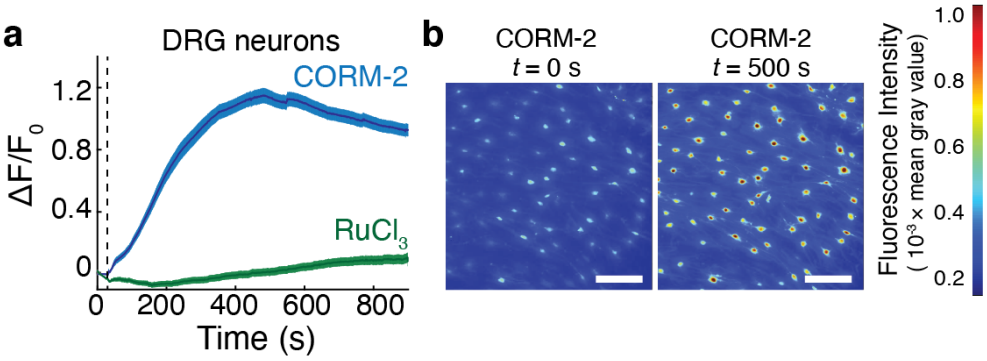

Figure 3-18: **CO triggers Ca^{2+} influxes in DRG neurons** a, Averaged fluo-4 fluorescence traces for dorsal root ganglion (DRG) neurons (n = 100 neurons for each trace) following the addition of 50 μM CORM-2 (blue) or 50 μM $RuCl_3$ (green) at 30 s (dashed lines). The solid lines and shaded areas represent the mean and s.e.m., respectively. b, Time-lapse images of Ca^{2+} responses in DRG neurons following the CORM-2 infusion (scale bar, 50μm).

Chapter 4

Magnetochemical Proton Generation for Remote Neuromodulation

4.1 Summary

This Chapter is based on J. Park et al., *Nano. Lett.*, 2021 [120].

Understanding and modulating proton-mediated biochemical processes in living organisms have been impeded by the lack of tools to control local pH. Here, we design nanotransducers capable of converting non-invasive alternating magnetic fields (AMFs) into protons in physiological environments by combining magnetic nanoparticles (MNPs) with polymeric scaffolds (Figure 4-1). When exposed to AMFs, the heat dissipated by MNPs triggered a hydrolytic degradation of surrounding polyanhydride or polyester, releasing protons into the extracellular space. pH changes induced by these nanotransducers can be tuned by changing the polymer chemistry or AMF stimulation parameters. Remote magnetic control of local protons was shown to trigger acid-sensing ion channels and evoke intracellular calcium influx in neurons. By offering a wireless modulation of local pH, our approach can accelerate the mechanistic investigation of the role of protons in biochemical signalling in the nervous system.

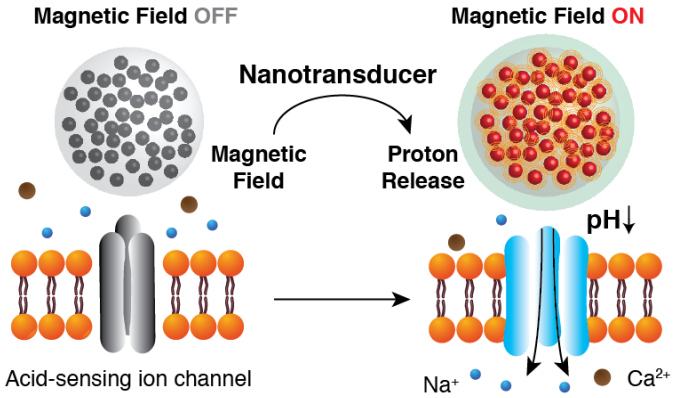

Figure 4-1: **An illustration of the magnetochemical proton generating system**

4.2 Background and Motivation

4.2.1 Degradation Kinetics of Biodegradable Polymers

During the past three decades, numerous types of biodegradable polymers have been developed for biomedical applications as drug delivery vehicles and scaffolds for tissue engineering [121, 122]. These polymers are naturally degraded by either hydrolytic or enzymatic routes and adsorbed by the tissue after finishing their biomedical mission. The clinical utilization of several biodegradable polymers, such as poly(lactic-co-glycolic acid) (PLGA), poly (ethylene glycol) (PEG), and poly(sebacic acid-co-1,3-bis(p-carboxyphenoxy) has been approved by the Food and Drug Administration in the USA [123, 124].

The unique characteristic of biodegradable polymers is that their physical, chemical, biological, and mechanical properties could be tailored for specific applications. For example, their biodegradation rates could be regulated up to $\sim 10^{10}$ folds by changing their chemical moieties and molecular weights [122, 125]. For example, the hydrolytic degradation rates of biodegradable polymers significantly decreased in the series of poly(anhydrides) $>$ poly(ketal) $\sim$ poly(ortho esters) $>$ poly(acetal) $>$ poly(hydroxyl esters)$>$ poly(amides) due to differences in reactivity of chemical moieties inside these polymers with water molecules [125]. In addition, hydrophilicity or physical features of polymeric scaffolds (size or shape) also affected their biodegradability rates [126]. Another parameter that can noticeably affect the degradation rates of biodegradable polymers is temperature [127, 128]. The activation energy of hydrolytic degradation of polymers is positive, indicating that increase in the temperature could accelerate their degradation processes. Previous reports explored the temperature-dependent degradation kinetics of biodegradable polymers and calculated the activation energy (E_a) for the degradation processes of polymers. For example, E_a of PLGA and poly(-olefin-co-maleic anhydride) degradation processes are measured as approximately 114 kJ/mole, 46 kJ/mole, respectively [127, 129].

4.2.2 Hysteretic Heat Dissipation by Magnetic Nanoparticles

To explain hysteretic heat dissipation by MNPs upon exposure to an AMF, understanding the thermodynamic reasoning for hysteresis is important. When we apply a high magnetic field to induce complete saturation of ferromagnetic materials followed by reducing the field back to zero, a remanent magnetization (M_r) remains at zero applied magnetic field. To demagnetize the ferromagnetic materials, a coercive field (H_c) is needed. Consequently, a hysteresis loop can be formed in the magnetization (M)-magnetic field (H) curves of ferromagnetic materials. The area of the hysteresis loop (B-H) is equal to the amount of energy that material is lost per cycle and unit volume [130].

The origin for the hysteresis is magnetic anisotropy that makes the magnetic moment tend to align along certain preferred directions [131]. Magnetic anisotropy originates from spin-orbital coupling within the crystal, the shape anisotropy, and surface effects [132–134]. Due to the magnetic anisotropy, different amount of magnetic field is needed to reach the saturation magnetization depending on the orientation of the magnetic field with respect to the atomic lattice. In other words, there are easy or hard axes which require small or large magnetic fields to achieve the saturation magnetization, respectively.

In the single domain MNP, the total energy (E_{tot}) can be expressed as summation of the anisotropy energy (E_a) and the Zeeman energy (E_z) induced by external field as follows (Equation4.1):

$$E_{tot} = E_a + E_z \approx K_u sin^2\theta + HM_s cos(\phi - \theta) \tag{4.1}$$

Where K_u, θ, and ϕ are the first-order uniaxial anisotropy coefficient, the angle between the magnetization and the easy axis, and the angle between the applied magnetic field and easy axis, respectively. In the case of easy axis magnetization ($\phi = 0°$), minimizing the total energy leads to the formation of an ideal rectangular shape of the hysteresis loop with the area of $8K_u$ and coercive field of $2K_u/M_s$, while those are zero in the hard axis magnetization case ($\phi = 90°$) [135, 136]. In the randomly

oriented cases, the estimated area of the hysteresis loop is approximately $4K_u$ [136]. It should be noted that any thermal activation process is ignored in the above cases (Stoner-Wohlfarth model).

In real situations, we should consider the effect of thermal fluctuations that result in spontaneous magnetization flips and consequently reduce the coercive field [137, 138]. As the energy barrier for flips is proportional to the volume of the single domain MNP, $K_u \times V$, the area of hysteresis loop significantly increased with the increase in MNP size [138]. However, if the coercive field becomes too large due to the large size of the MNP compared to the experimental field amplitude, only minor hysteresis loops could be accessed [139]. In this regard, controlling the size of the MNP is important for maximizing its hysteretic loss.

4.2.3 Emulsion Method for Nanocomposite Synthesis

Significant advances in emulsification solvent evaporation methods have enabled the synthesis of a myriad of polymeric particles with tunable sizes and compositions desirable for biomedical applications [121, 140]. As the formation of emulsion has either a kinetic or thermodynamic barrier, emulsification solvent evaporation method starts with applying external energy, usually in the form of heat or stirring, to the system [141]. For example, it has been known that the shear stress generated from a homogenizer or sonicator breaks up polymer-containing oil phase into microdroplets in an oil-in-water system [142]. Here, the oil-in-water system means that oil is the dispersed phase in water. In the viewpoint of thermodynamics, interfacial free energy between oil and water phases opposes the formation of emulsion, while configurational entropy term favors the emulsified state [141]. Therefore, to improve the thermodynamic stability of emulsified state, emulsifying agent, which reduces the interfacial free energy in the system through its amphiphilic nature, is incorporated during the emulsification process [141]. After emulsification, oil phase is slowly transported out from the droplets to the water phase, followed by evaporation at emulsion-air interface. Through this solvent evaporation process, polymer initially dissolved in the oil phase is hardened, finally resulting in the formation of polymeric particles.

The advantage of the utilization of emulsification solvent evaporation method is that diverse organic molecules or inorganic particles can be incorporated during the emulsification, endowing versatile functionality to the polymeric particles [143,144]. For example, hydrophobic drug molecules could be embedded in hydrophobic biodegradable polymer matrix, such as PLGA, and these hybridized polymeric particles can be used as drug delivery vehicles. As another example, previous reports demonstrated that MNP-PLGA nanoparticles could be utilized as magnetic resonance imaging agents [144].

4.2.4 Motivation

The pH of biological fluids is one of the critical factors that determine cellular function and viability [145–148]. In the nervous system, acidic environments affect neuronal function by triggering proton-activated ion channels, including acid-sensing ion channels (ASICs) [149–151]. ASICs play a role in multiple physiological processes, including synaptic plasticity, mechanosensation, learning and memory [151–153]. Furthermore, acid-induced toxicity mediated by ASICs contributes to neurological diseases, such as ischemic stroke and epileptic seizures [151]. Reduction in the extracellular pH also affects the function, morphology, and survival of non-neuronal glial cells [154, 155]. To understand proton-mediated neurobiological processes, multiple methods that can alter the pH in biological systems have been developed. While earlier studies evoked pH reduction with CO_2 inhalation, this method was often accompanied by off-target pH changes [156, 157]. More invasive techniques, such as microinjections of acidified medium through permanently implanted cannulas or control of protons with electrochemical devices, have been also applied to achieve localized pH modulation [157–160].

4.3 Wireless Generation of Proton with Magnetic Nanotransducers

In search of a less invasive technique to locally modulate pH of a target region, we designed a wireless proton generating platform controlled by low-radiofrequency AMFs. The latter exhibit minimal coupling to biological matter due to its low conductivity and negligible magnetic permeability [161]. Paired with hysteretic heating of MNPs, AMFs have been applied to control neural activity, gene expression, and hormone release [71, 162–164]. In this study, we leveraged the MNP heating in AMFs to manipulate local pH by integrating MNPs with polyanhydrides (or polyesters), which generate carboxyl groups as their hydrolysis products (Figure 4-2a) [123, 124]. MNP heating facilitated the hydrolytic degradation of the polymer, which in turn led to the rapid decrease in extracellular pH. We applied these chemomagnetic nanotransducers to convert an AMF cue into protons for the control of ASICs-mediated signalling processes in neurons (Figure 4-2b).

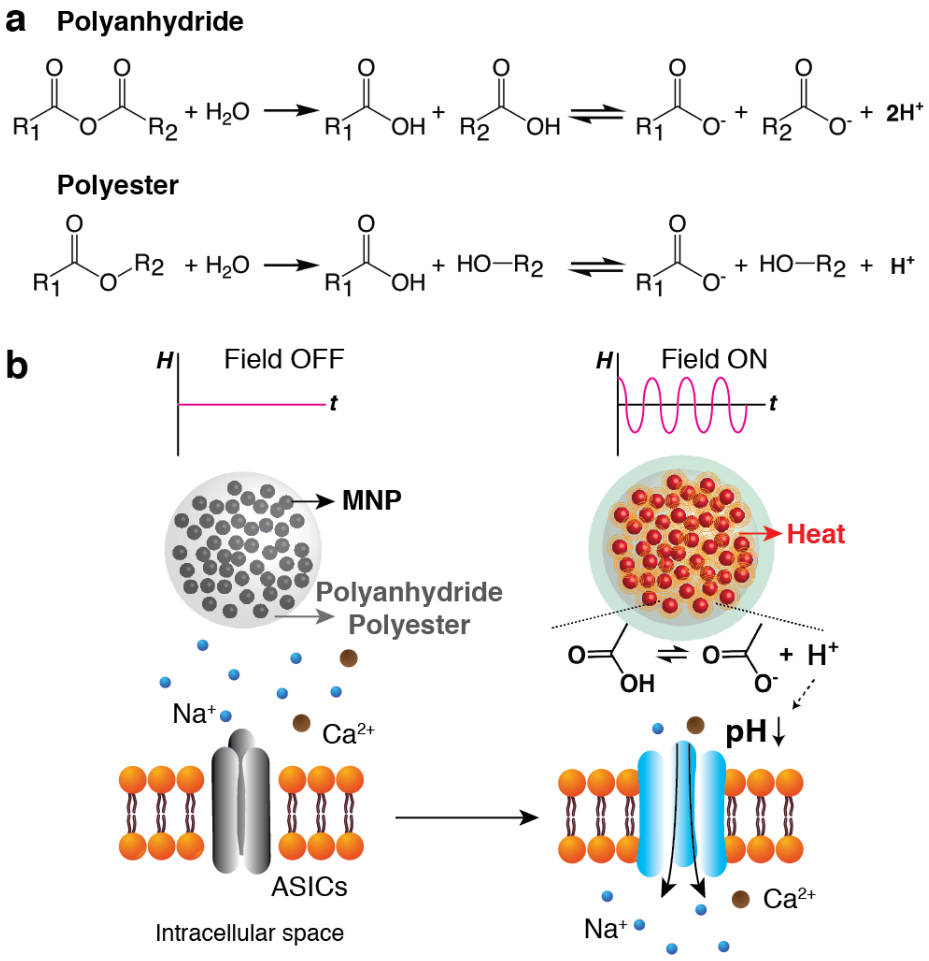

Figure 4-2: **Magnetic field-controlled proton generation system for remote activation of ASICs** a, Hydrolytic degradation of polyanhyride and polyester. Water-labile linkages in polyanhydride and polyester are converted into carboxyl groups following hydrolysis. b, An illustration of the wireless proton generating system. MNP heating elevates temperature inside the nanotransducers and accelerates the hydrolysis of polyanhydride and polyester. The carboxyl groups generated during the hydrolysis reduce the extracellular pH and activate neurons by triggering ASICs.

4.3.1 Nanotransducer Synthesis through Emulsion-Solvent Evaporation

As the first step to develop MNP-polymer nanotransducers, we prepared monodisperse Fe_3O_4 MNPs with diameters of 23.8 ± 1.7 nm (Figure 4-3a), which possess hysteretic heat dissipation rate of ∼ 500 $W/g_{[Fe]}$ in AMFs with amplitudes H_0 ∼ 15 kA/m and a frequency ∼ 500 kHz [139]. Similar particles have been previously shown to have negligible cytotoxic effects [71]. Motivated by prior research showing significantly higher temperature inside the sub-micrometer MNP-containing scaffolds as compared to the bulk ferrofluid during the MNP heating [165], we then designed MNP-polyanhydride or MNP-polyester nanotransducers, where synthesized MNPs were embedded inside the nanoscale polyanhydride or polyester scaffolds, respectively (Figure 4-2b). We hypothesized that significant temperature increase within these nanotransducers would accelerate the hydrolytic degradation of polymers [127] without comparable changes in temperature of the surrounding solution in AMFs. We employed poly(sebacic acid) (PSA) and poly(lactic-co-glycolic acid) (PLGA) as test-beds for demonstrating a proof-of-concept of our chemomagnetic approach to control local pH. PSA and PLGA are widely investigated polyanhydride or polyester biomaterials, respectively, due to their biocompatibility, tunable degradation rates, and well-established fabrication and surface modification methods [123, 124, 166].

The designed MNP-PSA or MNP-PLGA nanotransducers were synthesized by using an oil-in-water emulsion-solvent evaporation method [144]. Briefly, the mixtures of MNPs and PSA or PLGA dispersed in chloroform were emulsified with a high-speed homogenizer in the presence of the surfactant polyvinyl alcohol dissolved in deionized water. After evaporation of the chloroform, MNP-PSA or MNP-PLGA nanotransducers were collected and redispersed in Tyrode's solution. The percentage of MNPs in a nanotransducer was defined by the initial MNP-polymer ratio in the chloroform (Figure 4-3b). Transmission electron microscopy (TEM) images of representative MNP-PSA and MNP-PLGA nanotransducers with a 1:2 MNP:polymer weight ratio revealed high-density MNPs embedded within the spherical polymer scaffolds (Figure

4-3c,d). The diameters of the synthesized MNP-PSA and MNP-PLGA nanotransducers were measured as 432 ± 87 nm and 203 ± 32 nm, respectively (Figure 4-3e). Fourier transform infrared (FT-IR) spectrum of MNP-PLGA nanotransducers showed absorption bands near 1750, 1200, and 1100 cm^{-1} [167], which could be attributed to the C=O and two C-O stretching vibrations in the ester, confirming the presence of PLGA in the nanotransducer. Similarly, the existence of PSA in the MNP-PSA nanotransducer was confirmed by C=O, C-O, and -CH_2- bands in the FT-IR spectra (Figure 4-4).

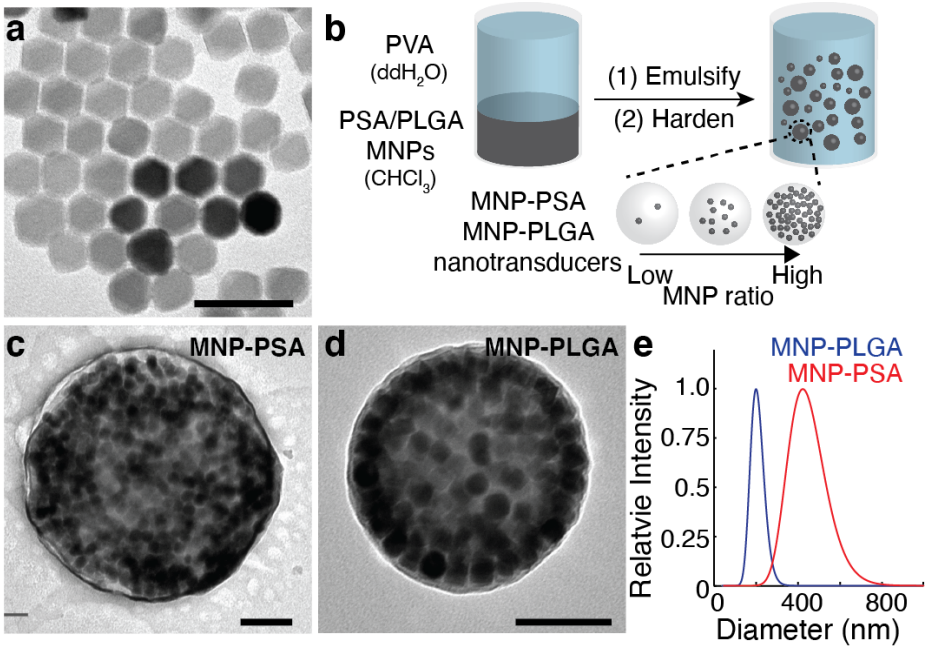

Figure 4-3: **Synthesis and characterization of MNP and MNP-PSA/MNP-PLGA nanotransducers** a, A transmission electron microscope (TEM) image of synthesized Fe_3O_4 MNPs. Scale bar: 50 nm. b, An illustration of the synthesis of MNP-PSA and MNP-PLGA nanotransducers via the emulsion-solvent evaporation method. c-d, Representative TEM images of a MNP-PSA (c) or a MNP-PLGA (d) nanotransducer (1:2 MNP:polymer weight ratio), respectively. Scale bar: 100 nm. e, Dynamic light scattering spectra of the MNP-PSA (red) and MNP-PLGA (blue), illustrating their size distributions.

4.3.2 Extracellular pH Changes Induced by Nanotransducers

We then evaluated the feasibility of applying the synthesized nanotransducers as wireless proton generators by recording the pH changes of a nanotransducer solution following exposure to an AMF. Physiologically safe AMFs with amplitudes H_0

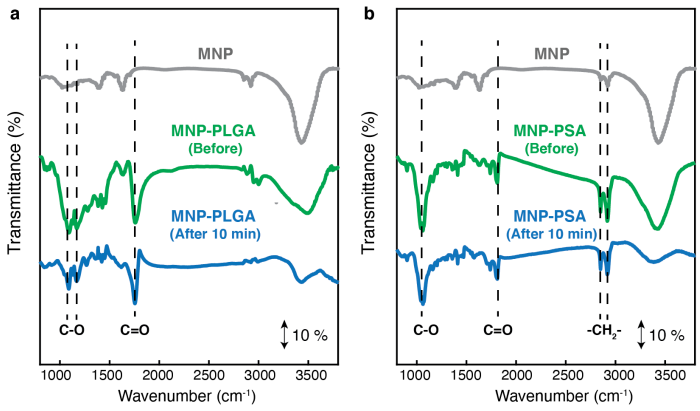

Figure 4-4: **FT-IR spectra of nanotransducers** a, Fourier transform infrared spectroscopy (FT-IR) spectra of MNPs (gray), MNP- PLGA nanotransducers (green), and MNP-PLGA nanotransducers after 10 min of exposure to AMFs (blue). b FT-IR spectra of MNPs (gray), MNP-PSA nanotransducers (green), and MNP- PSA nanotransducers after 10 min of exposure to AMFs (blue). As anticipated from the modest proportion of the hydrolyzed bonds (<10%), no noticeable appearance or disappearance of absorp- tion bands in MNP-PLGA or MNP-PSA were found after AMF stimulation.

$\sim$ 50 kA/m and a frequency $\sim$ 150 kHz were generated by a custom-designed resonant coil [71, 168, 169] and applied to Tyrode's solutions of nanotransducers (1:2 MNP:polymer weight ratio) with concentrations of $\sim$ 15 mg/mL. Following AMF exposure, the pH of the collected solution was recorded using a ratiometric pH-indicating fluorescent dye seminaphtharhodafluor (Figure 4-5a) [170]. After 60 s of exposure to AMFs, pH of Tyrode's solution containing MNP-PSA nanotransducers was reduced from 7.40 to 6.87 $\pm$ 0.17. Further exposure to the AMF led to the gradual decrease in pH to 6.52 $\pm$ 0.11 and 6.38 $\pm$ 0.22 after 300 s and 600 s, respectively. In the absence of AMF stimuli, only a slight decrease in solution pH to 7.18 $\pm$ 0.07 was observed even after 1 h of spontaneous hydrolytic degradation at room temperature (Figure 4-5b).

Exposure to the AMF of the MNP-PLGA nanotransducers did not result in significant pH changes compared to the MNP-PSA nanotransducers. The pH of a solution loaded with MNP-PLGA nanotransducers was only slightly reduced from 7.40 to 7.30 $\pm$ 0.05 and 7.24 $\pm$ 0.03 after 300 s and 600 s of exposure to AMFs, respectively. Even in the modified Tyrode's solution with buffer capacity reduced 10 fold, MNP-PLGA nanotransducers lowered the solution pH to 6.88 $\pm$ 0.06 and 6.60 $\pm$ 0.07

after 300 s and 600 s, respectively, which were smaller changes than those induced by MNP-PSA nanotransducers in unmodified Tyrode's solution (Figure 4-5b). The difference between these two groups can likely be attributed to an intrinsically slower hydrolysis rate of ester group in PLGA compared to that of anhydride group in PSA [125]. This observation was further confirmed in a follow-up experiment where the PSA and PLGA nanospheres were hydrolytically degraded in the absence of AMF stimuli (Figure 4-6). Together, these data suggest that MNP-PSA nanotransducers can remotely lower the solution pH in response to AMFs. Furthermore, the proton release kinetics of the nanotransducers are dependent on polymer chemistry. This dependency provides an opportunity to tune the release kinetics of the nanotransducers, minimize their spontaneous degradation before exposure to AMFs, and optimize their application in vitro or in vivo while reducing thermal effects.

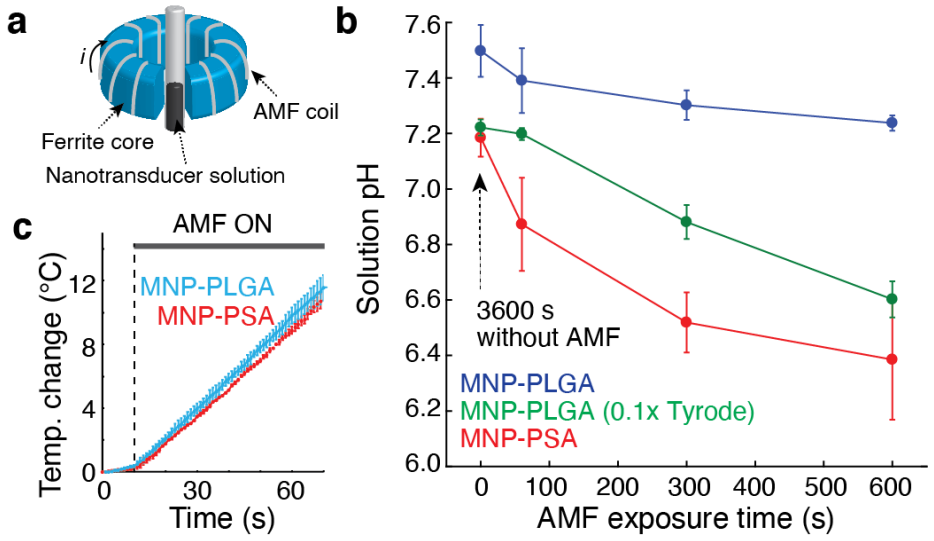

Figure 4-5: **Extracellular pH reductions induced by MNP-PLGA/MNP-PSA nanotransducers in AMFs** a, Experimental scheme for the analysis of proton release kinetics from nanotransducers in AMFs. AMFs were applied to Tyrode's solutions containing nanotransducers placed into the gap of an electromagnet of a toroid ferrite core. After exposure to an AMF, the solution was mixed with ratiometric pH indicator (seminaphtharhodafluor) solution. b, pH changes (mean ± standard deviation) of MNP-PLGA containing Tyrode's solution (blue, n=3), MNP-PSA containing Tyrode's solution (red, n=4), and MNP-PLGA containing 0.1× Tyrode's solution (green, n=4) as a function of AMF stimulation time. First point in each plot represents the pH changes 3600 s after reaction in the absence of AMF stimuli. c, Calorimetry measurements (mean ± standard deviation) for MNP-PLGA (blue, n=3) and MNP-PSA (red, n=3) containing Tyrode's solutions, respectively, before and during the AMF stimulation.

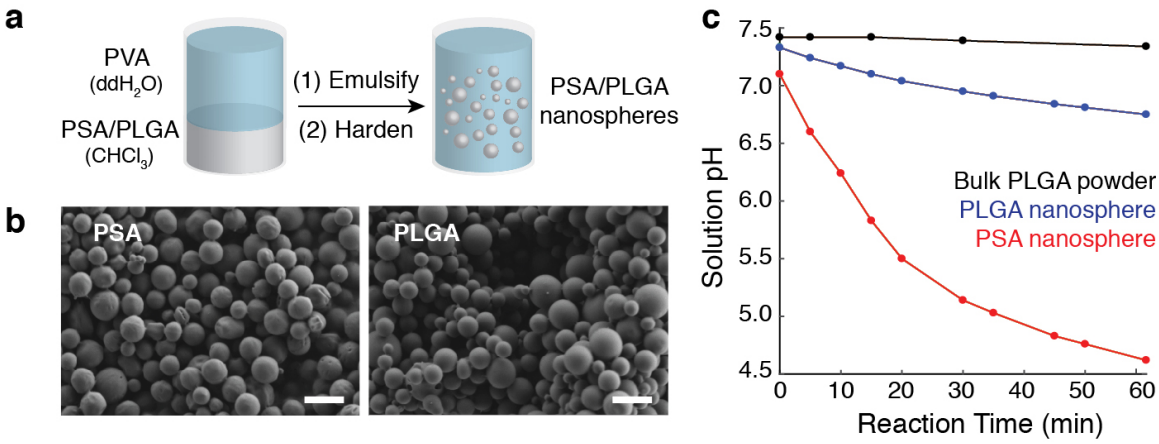

Figure 4-6: **Temperature-dependent degradation kinetics of PSA and PLGA nanospheres** a, An illustration of the synthesis of PSA and PLGA nanospheres with emulsion-solvent evaporation method. b, Scanning electron microscopy (SEM) images of synthesized PSA and PLGA nanospheres. Scale bar: 1 μm. c, pH changes of 6.67 mg/mL bulk PLGA powder (black), 6.67 mg/mL PLGA nanosphere (blue), and 6.67 mg/mL PSA nanosphere (red) containing Tyrode's solutions over time at 85°C. Faster reduction in solution pH was found in PSA nanosphere group as compared to PLGA nanosphere group.

4.3.3 Mechanistic Studies: Local Heating Effect

Finally, to test our hypothesis that the local heating near the MNPs surfaces rather than the bulk solution heating (Figure 4-5c), predominately accelerated the hydrolysis of PSA upon exposure to an AMF, we compared pH and temperature changes of Tyrode's solutions containing MNP-PSA nanotransducers and those of the concentration-matched physical mixtures of MNPs and PSA-only nanospheres after exposure to AMFs. We anticipated that hydrolysis of PSA nanospheres in physical mixtures with MNPs would be mainly attributed to the increase in the bulk solution temperature during ferrofluid heating in the AMF. We found that in contrast to the solutions of MNP-PSA nanotransducers, the exposure to the AMF stimuli did not evoke noticeable pH reductions in physical mixtures of MNPs and PSA nanospheres. The pH of solutions containing physically mixed MNPs and PSA nanospheres was only slightly reduced from 7.4 to 7.06 $\pm$ 0.09 and 7.03 $\pm$ 0.03 after 300 s and 600 s of exposure to AMF, respectively. However, no statistically significant difference in bulk temperature changes was found between the two groups (Figure 4-7). These findings suggest that the hydrolytic degradation of PSA in MNP-PSA nanotransducers

is largely driven by the local heat dissipation from MNPs.

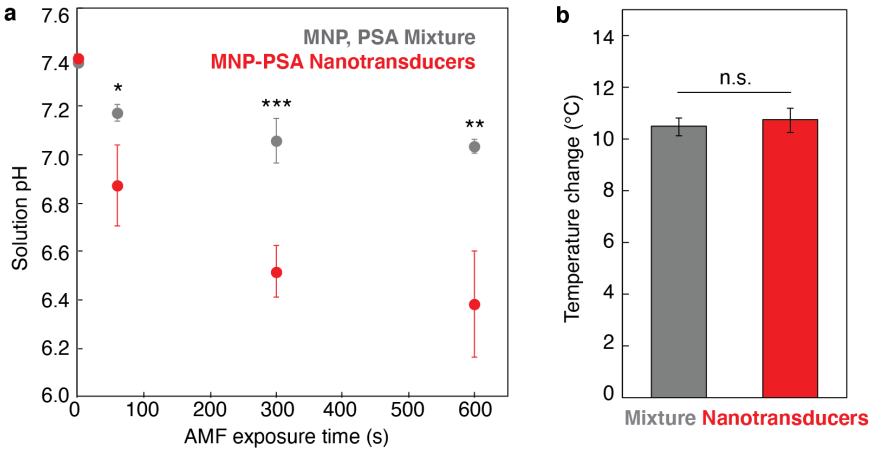

Figure 4-7: **Local heating effects on the proton release kinetics of nanotransducers in AMFs** a, pH changes of Tyrode's solutions of MNP-PSA nanotransducers (red, n=4) and of concentration-matched, physically-mixed MNP and PSA Tyrode's solutions (gray, n=3) as a function of AMF stimulation time (one-tailed Student's t-test, * $p < 0.05$, ** $p < 0.01$, *** $p < 0.001$). b, Bulk temperature increase of MNP-PSA nanotransducer solutions (red, n=4) and concentration-matched, physically-mixed MNP and PSA solutions (gray, n=3) after 60 s of AMF stimulation (one-tailed Student's t-test, $p = 0.25$).

4.4 Remote Control of Proton-Mediated Cell Signaling In Vitro

4.4.1 Proton-Mediated Ca^{2+} Influxes in Neurons

To investigate the ability of the nanotransducers to modulate proton-mediated signaling processes, we applied them to trigger ASICs, which are endogenously expressed Na^+-selective cation channels in the central nervous system [151]. Activation of ASICs induces entry of Na^+ ions into the cells, causing membrane depolarization and activation of voltage-gated Ca^{2+} channels [149, 151]. We chose to focus on hippocampal neurons because of their well-characterized ASIC expression and culture methods [153, 171]. We recorded the intracellular Ca^{2+} changes using the green fluorescent Ca^{2+} indicator fluo-4 as a proxy for membrane depolarization (Figure 4-8a) [114]. We first confirmed the functionality of endogenously expressed ASICs in the cultured hippocampal neurons. Consistent with prior studies, [150, 172] we observed that a rapid extracellular pH reduction induced Ca^{2+} influxes into the neurons. When exposed to an acidified medium with pH of 6.8, the normalized fluo-4 fluorescence ($\Delta F/F_0$) in the neurons increased by 24 $\pm$ 7 %. Ca^{2+} influx into the neurons at identical conditions was greatly diminished by the addition of 500 μM of the non-specific ASIC blocker amiloride, [149] indicating that Ca^{2+} influxes observed in the hippocampal neurons in reponse to pH decrease are predominately mediated by ASICs (Figure 4-8b).

Acid-evoked Ca^{2+} responses in the hippocampal neurons were further enhanced following viral transgene delivery and over-expression of ASIC1a, the predominant ASIC subunit in the central nervous system [149]. To enhance the expression levels of ASIC1a, neurons were transduced with lentivirus carrying ASIC1a transgene along with a fluorescent protein mCherry separated by the post-transcriptional cleavage linker p2A under the excitatory neuronal promoter calmodulin kinase II α-subunit (*Lenti-CaMKIIα::ASIC1a-p2A-mCherry*). The expression of mCherry-tagged ASIC1a was confirmed via fluorescent imaging in the transduced neurons (Figure 4-8c). The

ASIC1a-overexpressing (ASIC1a$^+$) neurons showed a robust fluo-4 fluorescence increase ($\Delta F/F_0 \sim 137 \pm 12$ %) following the injection of an acidified medium with pH of 6.8 (Figure 4-8d). At identical extracellular pH conditions, ASIC1a$^+$ neurons exhibited significantly higher Ca^{2+} influxes as compared to genetically intact neurons (Figure 4-8e). Addition of the amiloride has similarly led to a decrease in proton-mediated Ca^{2+} influxes in ASIC1a$^+$ neurons, akin to our observation in the genetically intact cultures (Figure 4-8b).

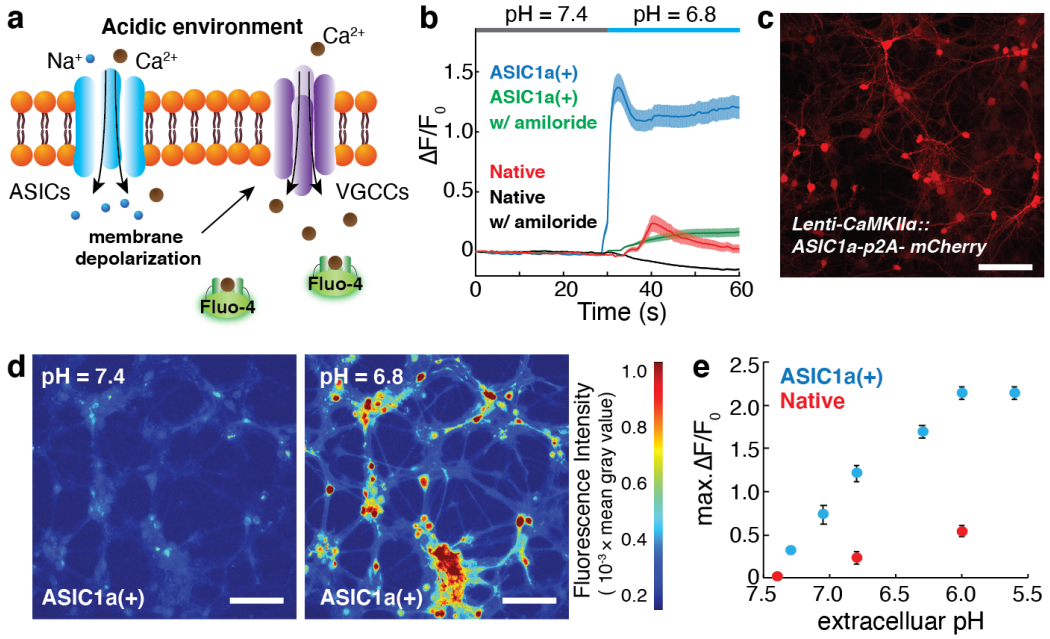

Figure 4-8: **Proton-mediated Ca^{2+} influxes in hippocampal neurons** a, A schematic illustrating proton-mediated Ca^{2+} responses in the hippocampal neurons. Acidic extracellular environment leads to the depolarization of the cell membrane by triggering cation (Na^+/Ca^{2+}) permeable ASICs, followed by the activation of voltage-gated Ca^{2+} channels (VGCCs). b, Normalized fluo-4 fluorescence profiles averaged across 100 genetically intact neurons (red) and 100 ASIC1a-overexpressing (ASIC1a$^+$) neurons (blue) following the rapid infusion of acidified medium (pH=6.8) at 30 s. At the same experimental condition, the proton-mediated Ca^{2+} influxes were greatly diminished by the addition of ASICs blocker amiloride to 100 native neurons (black) and 100 ASIC1a$^+$ neurons (green). Solid lines and shaded areas represent the mean and standard error of the mean (s.e.m.), respectively. c, A fluorescent image of ASIC1a$^+$ neurons. Scale bar: 50 μm. d, Representative fluo-4 fluorescent images of ASIC1a$^+$ neurons before and after the infusion of acidified medium (pH 6.8), showing robust Ca^{2+} influx in ASIC1a$^+$ in respond to acidic environment. Scale bar: 50 μm. e, Extracellular pH dependent maximum of normalized fluo-4 fluorescence increases (mean± s.e.m.) averaged across 100 native neurons (red) and 100 ASIC1a$^+$ neurons (blue) during 60 s of measurement.

4.4.2 Neuronal Activation by Nanotransducers Under Magnetic Fields

We next examined whether our nanotransducers could similarly trigger ASICs. Before applying AMF stimulation, we confirmed that both MNP-PSA and MNP-PLGA nanotransducers did not evoke significant cytotoxic responses in vitro. To elicit robustly measurable Ca^{2+} responses, we used ASIC1a^{+} neurons and MNP-PSA nanotransducers. ASIC1a^{+} neurons immersed in Tyrode's solution containing MNP-PSA nanotransducers (15 mg/mL, 1:2 MNP:PSA weight ratio) were exposed to AMFs for 60 s with the parameters previously shown to evoke the reduction of extracellular pH from 7.40 to 6.87 (50 kA/m at 150 kHz). Here, the MNP-PSA nanotransducer concentration and MNP-PSA ratio were optimized to induce a significant pH reduction required for ASIC activation (pH for half-maximum responses $pH_{50} \sim 6.8$) [151], while reducing non-specific thermal effects (Figure 4-9, Figure 4-10, Figure 4-11) [173]. Note that the resulting solution temperature following AMF application was 36 ℃, which is below the activation threshold for thermosensitive ion channels [71, 173].

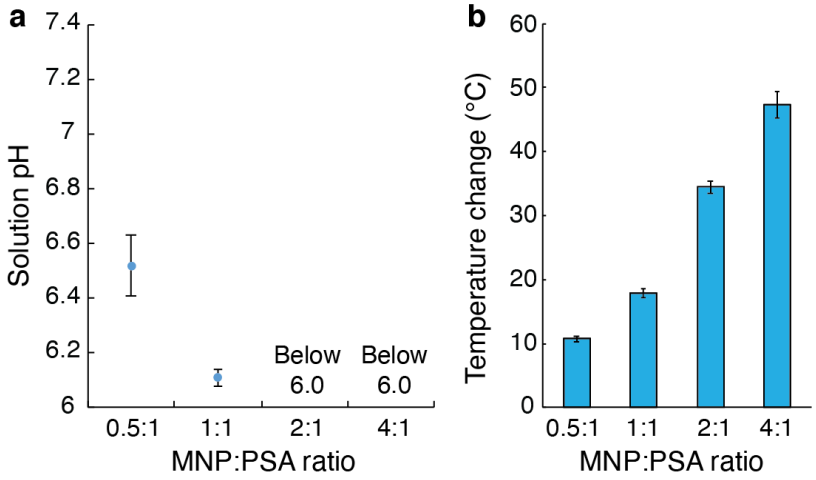

Figure 4-9: **Effects of the MNP-PSA ratio on changes in extracellular pH and temperature of MNP-PSA nanotransducer solutions** a, pH changes (mean ± standard deviation, n=3) in Tyrode's solutions of MNP-PSA nanotransducers as a function of the MNP-PSA ratio. Here, identical amounts of PSA were utilized and MNP contents were tailored accordingly. The pH of a solution was measured after 300 s of exposure to AMFs. b, Bulk temperature increases (mean ± standard deviation, n=3) in Tyrode's solutions of MNP-PSA nanotransducers 60 s after the AMF stimulation as a function of the MNP-PSA ratio. Significant temperature increases ($>$ 18°C, starting temperature: 25°C, final temperature: $>$ 43°C) were found in solutions with the ratio of MNP to PSA above 1.

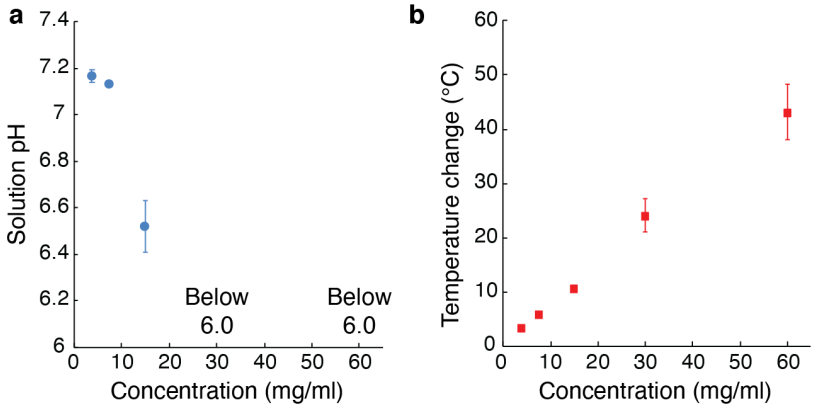

Figure 4-10: **Effects of nanotransducer concentration on changes in extracellular pH and temperature of MNP-PSA nanotransducer solutions** a, pH changes (mean ± standard deviation) of MNP-PSA nanotransducers containing Tyrode's solution (n=3) as a function of the nanotransducer concentration. Here, the pH of a solution was measured after 300 s of exposure to AMFs. b, Bulk temperature increases (mean ± standard deviation) of MNP-PSA nanotransducers containing Tyrode's solution (n=3) 60 s after the AMF stimulation as a function of the nanotransducer concentration.

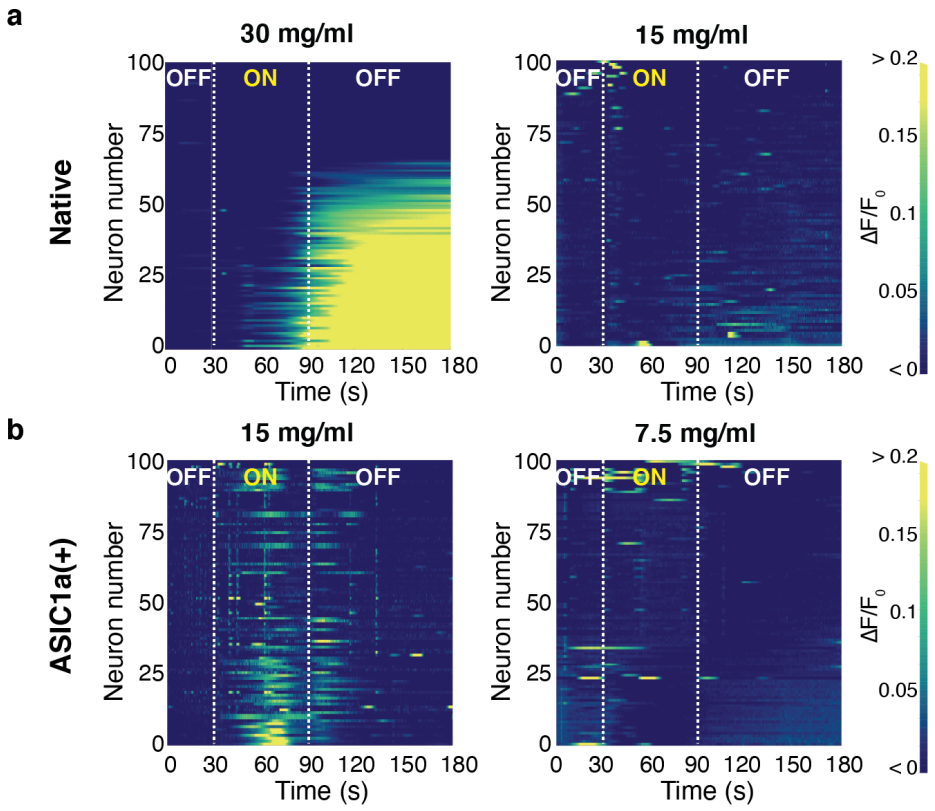

Figure 4-11: **Ca^{2+} responses in native and ASIC1a^{+} neurons evoked by MNP-PSA nanotransducers with various concentrations** a-b, Individual fluo-4 fluorescence traces for 100 native (a) and ASIC1a^{+} neurons (b) at different MNP-PSA nanotransducer concentrations. AMFs were turned on at 30 s and applied for 60 s (dashed lines). F_0 was obtained by averaging the fluorescence intensity during the initial 10 s of measurement. (a) Temperature increase ($\sim$ 24 °C, starting temperature: 25 °C, final temperature: $\sim$ 49 °C) mediated by the nanotransducer solution with concentration of 30 mg/mL evoked sustained and robust Ca^{2+} influxes. In contrast, no significant heating effect of $\sim$ 15 mg/mL nanotransducer solution (temperature increase: $\sim$ 11 °C, starting temperature: 25 °C, final temperature: $\sim$ 36°C) was found in native neurons. (b) No noticeable Ca^{2+} influxes were observed in ASIC1a^{+} neurons in the presence of the nanotransducer solutions with concentration of $\sim$ 7.5 mg/mL, due to the insignificant pH reduction after AMF stimulation.

After $\sim$ 32 s of exposure to AMFs, noticeable Ca^{2+} influxes were found in the ASIC1a$^+$ neurons (Figure 4-12a). Significantly greater proportion of ASIC1a$^+$ neurons exhibited Ca^{2+} influxes (as identified by $\Delta F/F_0 \geq 10\%$) in response to the AMF stimulation in the presence of MNP-PSA nanotransducers as compared to control groups, which included neurons immersed in MNP-PSA nanotransducer solutions and not subjected to the AMF stimulation, neurons subjected to the AMF stimulation in the presence of PSA-only nanospheres, and neurons immersed in bulk MNP-only solutions without PSA and subjected to the AMF (Figure 4-12a-d). These findings indicate that proton release from the nanotransducers during AMF stimulation dominates over other potential mechanisms leading to Ca^{2+} influxes, including spontaneous hydrolytic degradation of PSA, which might result in the reduction in the local pH, or the increase in the bulk solution temperature mediated by the MNPs, which could potentially cause depolarization and action potentials in neurons [173]. Indeed, a small fraction of neurons exhibited Ca^{2+} influx in response to the AMF-driven temperature increase in MNP solutions without PSA, however the extent of the response was significantly lower than that observed in the presence of MNP-PSA nanotransducers (Figure 4-12e). Moreover, Ca^{2+} influx into ASIC1a$^+$ neurons in the presence of the nanotransducers and AMF stimulation was greatly blocked by the addition of amiloride, further supporting that Ca^{2+} responses in the ASIC1a$^+$ neurons are mainly attributable to proton generation by the nanotransducers.

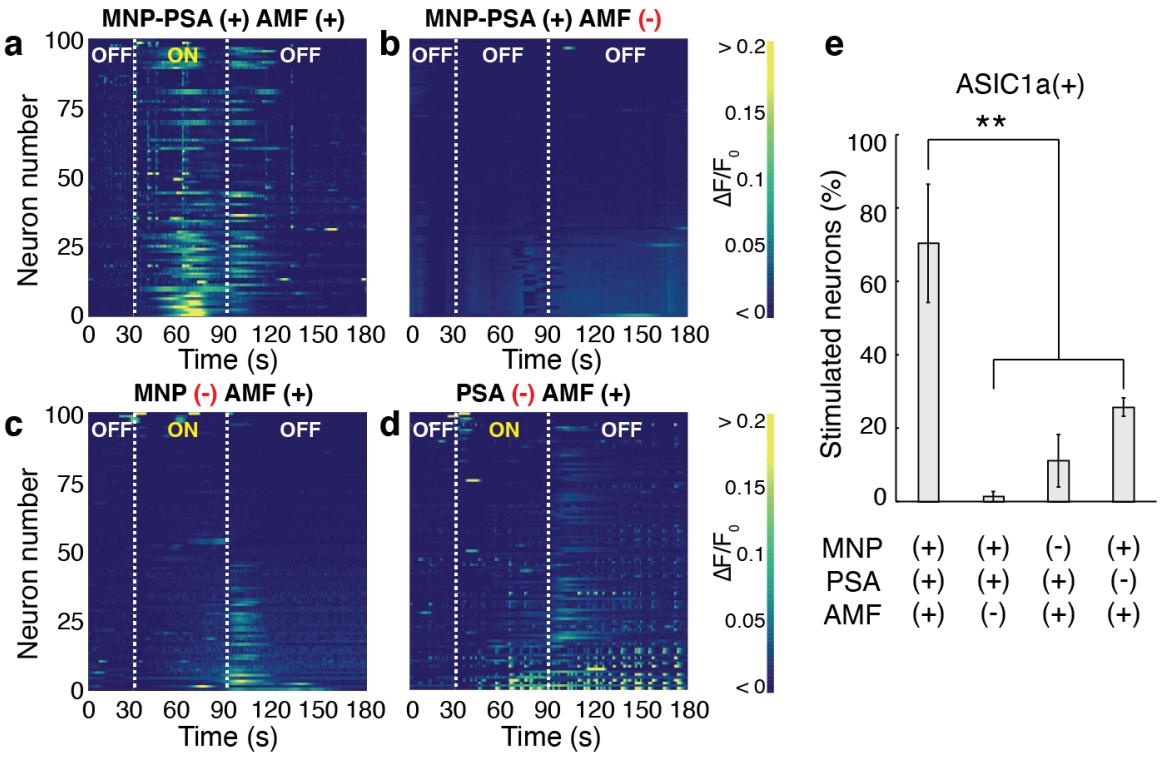

Figure 4-12: **Remotely controlled proton generation triggers ASICs and induces Ca^{2+} influxes in ASIC1a$^+$ neurons** a-d, Individual fluo-4 fluorescence traces for 100 ASIC1a$^+$ neurons at different experimental conditions. AMF(-) in (b) indicates that AMF is not applied during the measurement. MNP(-) in (c) and PSA(-) in (d) indicate PSA-only control particles without MNP (c) and concentration-matched MNP-only solutions without PSA (d). AMFs were turned on at 30 s and applied for 60 s (dashed lines). Averaged $\Delta F/F_0$ and individual fluo-4 fluorescence traces were analyzed with 100 neurons randomly selected from three independently conducted experiments. e, The percentages (mean ± s.e.m.) of the stimulated ASIC1a$^+$ neurons (as identified by $\Delta F/F_0 \geq 10\%$) at different experimental conditions (one-way ANOVA, n = 3 plates, $F_{3,8}$= 11.70, p = 0.0027, ** $p < 0.01$). Post-hoc Tukey's honest significant difference method was used for pairwise comparison.

4.5 In Vivo Application of Nanotransducers for Wireless Neuromodulation

4.5.1 Theoretical pH and Temperature Profiles In Vivo

To explore the potential feasibility of future applications of the nanotransducers in vivo, we employed a finite element model (FEM) to approximate local pH and temperature changes induced by MNP-PSA nanotransducers in the buffering system of the brain. In this model, 1 μL of MNP-PSA nanotransducer solution (15 mg/mL, 1:2 MNP:PSA weight ratio) used for in vitro studies was injected into the brain. Based on experimentally observed pH and temperature changes induced by identical experimental conditions in vitro (Figure 4-5), we calculated the theoretical proton and heat flux of nanotransducer solutions in AMFs. A mean-field approximation was made to estimate the bulk homogeneous reaction rate for the simulation derived from the rate of heterogeneous surface reactions occurring on individual nanotransducers. After 60 s of exposure to AMFs, the MNP-PSA nanotransducer solution caused a noticeable pH reduction ($<$ 6.8) inside the injected fluid volume (Figure 4-13a,c). After turning off the AMF, the pH gradually recovered over time (Figure 4-13b,d). At the same AMF conditions, no significant temperature increase ($<$ 1 ℃) was found between the injection site and the surrounding environment (Figure 4-13e,g). The small temperature gradients disappeared in 120 s in the absence of AMF stimulation (Figure 4-13f,h), owing to the higher diffusivity of heat compared to mass. It should be noted that MNP concentration (and iron content, 3.6 $mg_{[Fe]}$/mL) in our system is significantly smaller than that of the ferrofluids (50-100 mg/mL) commonly used for thermal stimulation of electroactive cells in vivo [71,164]. A finer meshing scheme yielded identical results, and turning off the heat sink into the brain recovered the in vitro findings. Along with our experimental observations during in vitro Ca^{2+} imaging, these numerical results suggest that our approach could, in the future, be applied to target acid-sensing neurons, such as those in the amygdala [174] (Figure 4-14), while avoiding non-specific thermal effects.

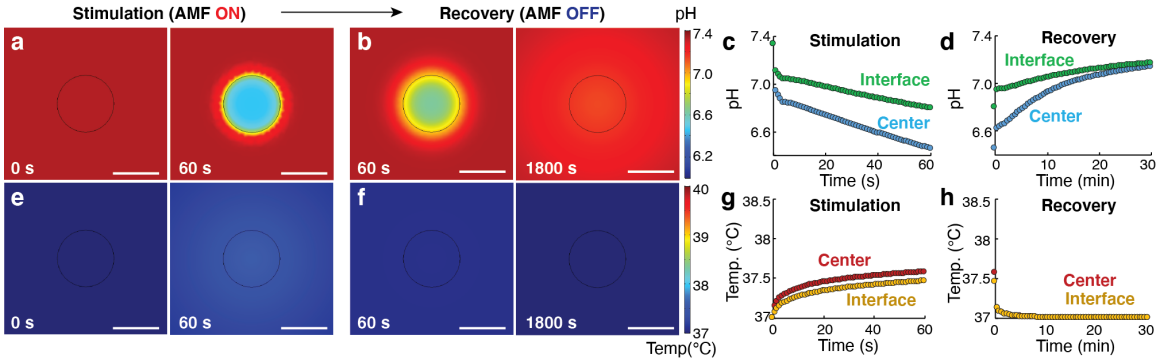

Figure 4-13: **Calculated pH and temperature profiles within and around a 1 μL MNP-PSA nanotransducer solution in vivo** a-b, Calculated pH profiles within and around a 1 μL injection of MNP-PSA nanotransducer solution in the buffering system of cerebral spinal fluid (CSF) at 0 s and 60 s of AMF stimulation (a), and 60 s or 1800 s after the AMF stimulation is turned off (b). Black circle indicates the CSF/injection interface. Scale bar: 1 mm. c-d, The corresponding values for the pH at the center of the injection and at the interface. e-f, Calculated temperature profiles within and around the same injection at 0 s and 60 s of the identical AMF stimulation (e), and 60 s or 1800 s after the AMF stimulation is turned off (f). Black circle indicates the CSF/injection interface. Scale bar: 1 mm. g-h, The corresponding values for the temperature at the center of the injection and at the interface.

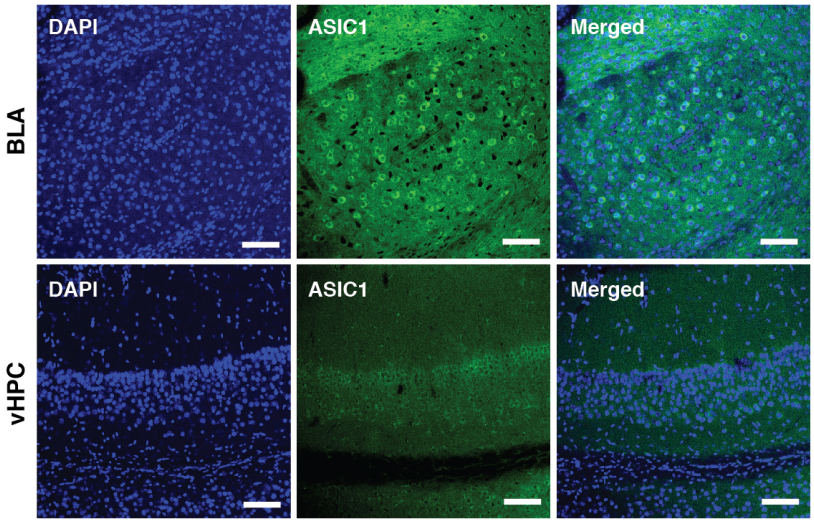

Figure 4-14: **ASIC expression in BLA and vHPC of the mouse brain** Representative confocal images of basolateral amygdala (BLA) and ventral hippocampus (vHPC) of a wild-type mouse (Male C57BL/6, Jackson Lab). High endogenous ASIC1 expression levels can be found in the BLA. Scale bar: 50 μm.

4.5.2 Control of Breathing Responses with Nanotransducers

Among diverse acid-sensitive brain regions, we targeted the retrotrapezoid nucleus (RTN), a well-characterized respiratory chemoreceptor, to investigate the feasibility of the nanotransducers in vivo. It has been known that RTN neurons can detect acidic environments, such as an increase in CO_2 partial pressure, through two types of proton receptors (TASK2, GPR4) expressed in these neurons. When exposed to the acidic environments, the firing rates of RTN neurons increases through the interactions between these proton receptors and protons. Changes in the firing rates of RTN neurons ultimately influence the breathing patterns of the subjects by affecting their projections in brainstems that regulates respiratory responses, such as the ventral respiratory column and nucleus of the solitary. [175, 176].

We first confirmed the functionality of RTN neurons by recording the breathing responses of anesthetized mice under different CO_2 partial pressure conditions. For the recordings, anesthetized mice were placed inside the recording chamber, and air (0.04 % CO_2) or 10 % CO_2 balanced with air were delivered to the chamber. The breathing response of the mice was recorded with a pressure sensor connected to the recording chamber, and the voltage signals converted by the pressure sensor were amplified by a custom-designed signal amplifier. Consistent with prior studies [175, 176], we found that an acute increase in partial pressure of CO_2 (10 % CO_2 balanced with air) inside the chamber accelerated breathing rates of the mice (phases 2, 4 in Figure 4-15). On the other hand, when we reduced the partial pressure of CO_2 by delivering air gas, the breathing rates of the mice decreased to normal levels (phases 3, 5 in Figure 4-15). These experiments corroborated that the breathing response of mice is sensitive to pH changes in the brain.

We then investigated whether our nanotransducers can similarly regulate breathing responses of anesthetized mice by acidifying the RTN neurons under magnetic fields. We injected MNP-PSA nanotransducer solutions or control particle solutions (concentration-matched MNP-only solutions without PSA or PSA-only particles without MNP solutions) into the RTN (coordinates relative to bregma: - 6.4 mm anteri-

orposterior, ± 1.3 mm mediolateral, and - 6.2 mm dorsoventral) of the mice utilizing a microinjection apparatus. After injection, the anesthetized mice were transferred to a custom-designed coil (working volume: $\sim$ 7 cm in diameter and $\sim$ 5 cm in height), which can produce AMFs with amplitude $H_0 \sim 40$ kA/m at a frequency $\sim$ 164 kHz. The mice were then connected to the recording nose cone inside the coil, which has constant air delivery to avoid accumulation of CO_2 inside the chamber (Figure 4-16). Finally, the mice were exposed to a sequence of three AMF cycles (60 s ON period followed by 180 s OFF rest periods). The breathing responses of the mice were simultaneously recorded with a pressure sensor connected to the chamber. We found that the breathing frequencies of mice that had been injected with MNP-PSA nanotransducers gradually increased after AMF stimulation, whereas negligible changes in breathing patterns were found in the control groups, including mice only subjected to AMF stimulation, mice subjected to AMF stimulation and injection of PSA-only nanospheres, and mice injected with bulk MNP-only solutions and subjected to AMF (Figure 4-17). These results demonstrated that MNP-PSA nanotransducers can remotely modulate animal behaviors by activating acid-sensing brain structures under AMFs.

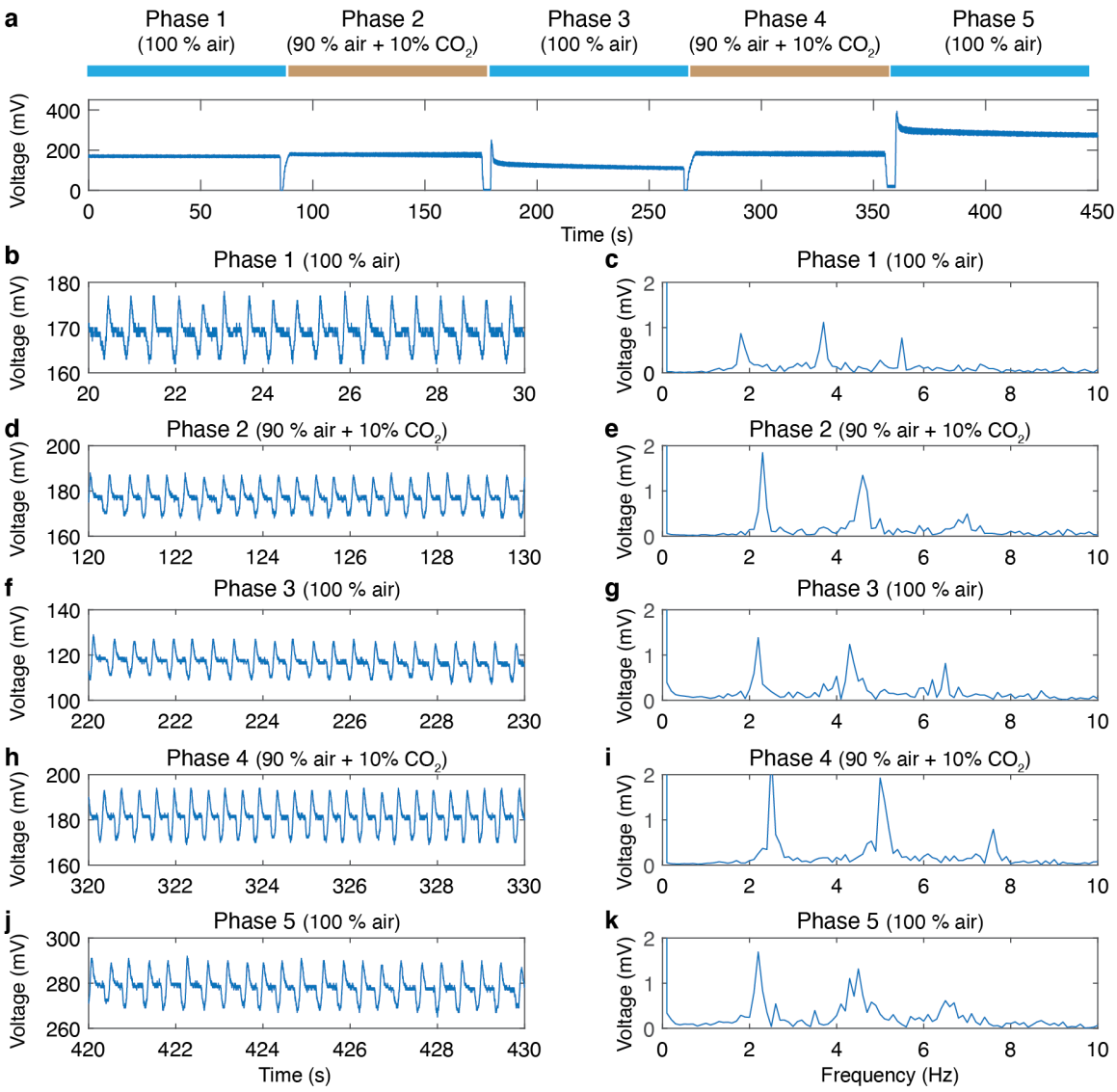

Figure 4-15: **Breathing responses of anesthetized mice under various CO_2 partial pressure conditions** a, A representative breathing pattern of the anesthetized mouse recorded by a pressure sensor at various CO_2 partial pressure conditions. b-k, Enlarged voltage traces (breathing patterns) of the mouse as a function of time (left) and Fourier transform of the voltage traces to extract characteristic frequencies (breathing rates of the mouse) (right). The characteristic frequencies increased upon delivery of 10 % CO_2 balanced with air (from phase 1 to phase 2 and from phase 3 to phase 4).

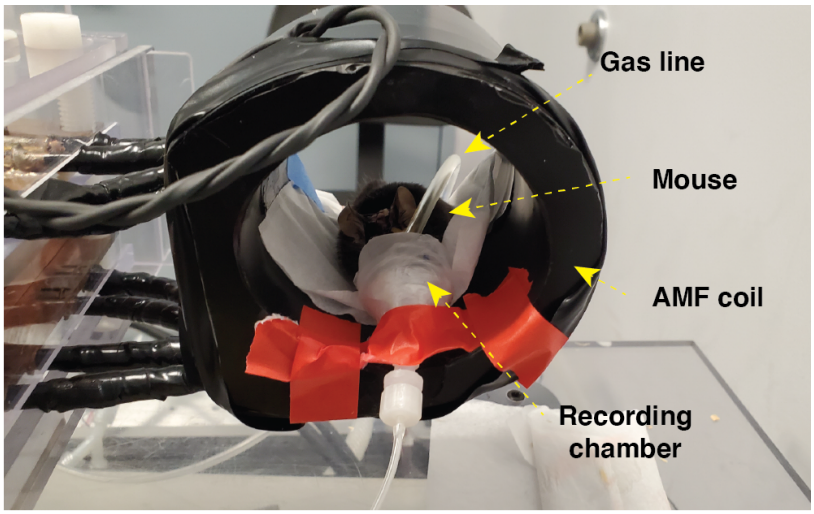

Figure 4-16: **Respiration recording system integrated with the custom-designed AMF coil** After injection of nanotransducers into the RTN, an anesthetized mouse is connected to the breathing recording chamber. Air is constantly delivered to the recording chamber through the gas line, and AMFs are produced by the coil.

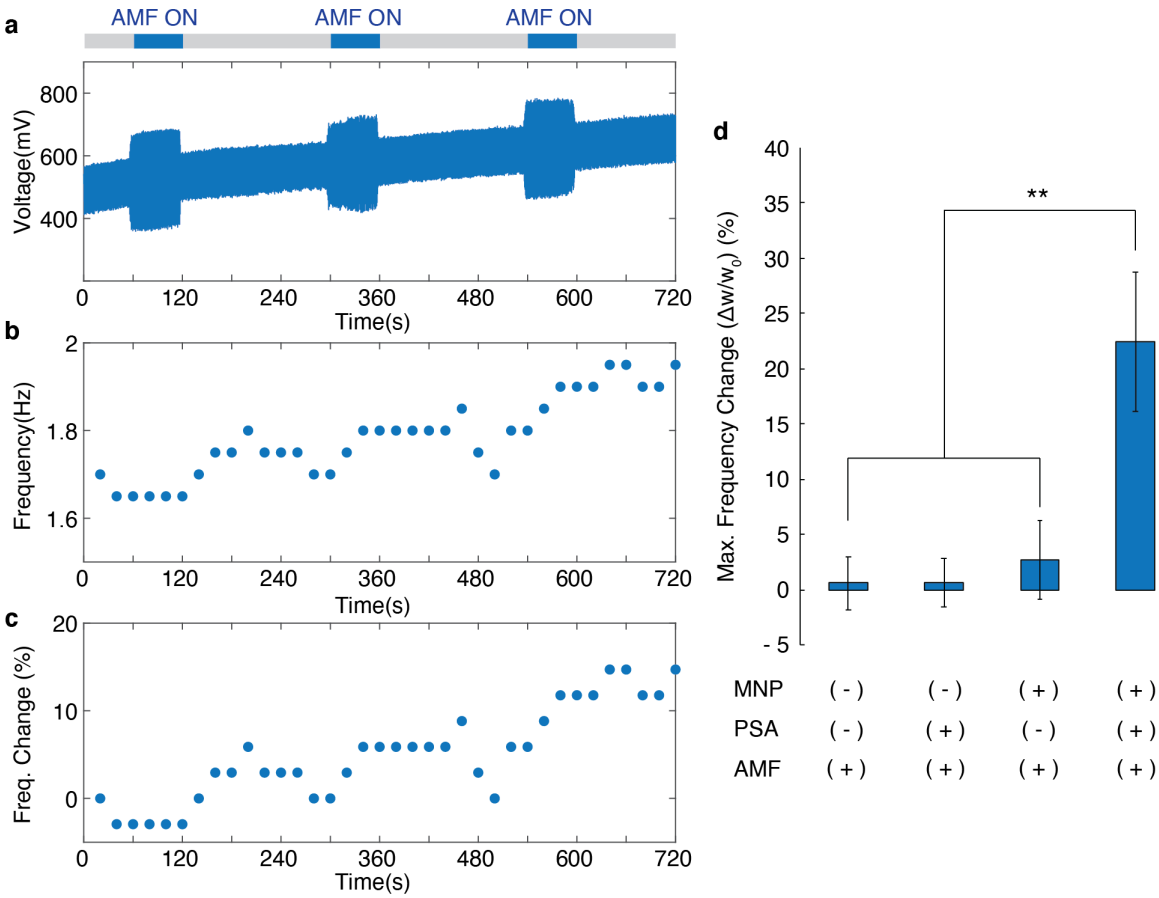

Figure 4-17: **Increased breathing rates of mice induced by MNP-PSA nanotransducers under AMFs** a, A representative breathing pattern of the anesthetized mouse injected with MNP-PSA nanotransducers under AMFs. AMFs were applied for 60 s at times t_1 = 60 s, t_2 = 300 s, and t_3= 540 s during the recordings. b, Characteristic frequencies (breathing rates of the mouse) extracted by Fourier transform of (a) as a function of time. c, Normalized breathing rate change ($\Delta w/w_0$, where w_0 indicates the breathing rate during the initial 20 s of measurement) as a function of time. d, Maximum of normalized breathing rate change ($\Delta w/w_0$, mean ± s.e.m.) during recordings (one-way ANOVA, n = 3 or 4 per each group, $F_{3,10}$= 8.07, p = 0.005, ** $p < 0.01$). Post-hoc Tukey's honest significant difference method was used for pairwise comparison.

4.6 Discussion and Conclusion

We created a tool to locally lower the pH of targeted regions on-demand in response to a non-invasive AMF cue. Rationally designed nanotransducers based on MNPs and PSA composites converted a magnetic stimulus into proton mass transfer via thermally triggered hydrolysis of an anhydride group. This enabled remotely controlled activation of acid-sensing neurons in vitro. Finally, we demonstrated that these nanotransducers can remotely modulate activity of acid-sensing neurons in a deep brain structure of mice and alter the breathing responses of mice under AMFs. As AMFs permit wireless targeting of structures deep within the body, nanotransducers can be applied to modulate diverse acid-sensing neurons in the brain, advancing the understanding of proton-mediated processes in the nervous system. Furthermore, our approach potentially provides a platform to investigate proton-mediated biochemical and physiological processes, such as enzymatic reactions [147], protein folding [177], and immune response [178].

Chapter 5

Magnetochemical Control of Redox Cofactor Chemistry

5.1 Summary

This Chapter is based on J. Park et al., *Angew. Chem. Int. Ed.*, 2021 [179].

Redox cofactors mediate many enzymatic processes and are increasingly employed in biomedical and energy applications. Exploring the influence of external magnetic fields on redox cofactor chemistry can enhance our understanding on magnetic field-sensitive biological processes and allow the application of magnetic fields to modulate redox reactions involving cofactors. Through a combination of experiments and modeling, we investigate the influence of magnetic fields on electrochemical reactions in redox cofactor solutions. By employing flavin mononucleotide (FMN) cofactor as a model system, we characterize magnetically induced changes in Faradaic currents. We find that radical pair intermediates have negligible influence on current increases in FMN solution upon application of a magnetic field. The dominant mechanism underlying the observed current increases is the magneto-hydrodynamic effect. We extend our analyses to other diffusion-limited electrochemical reactions of redox cofactor solutions and arrive at similar conclusions, highlighting the opportunity to use this framework in redox cofactor chemistry (Figure 5-1).

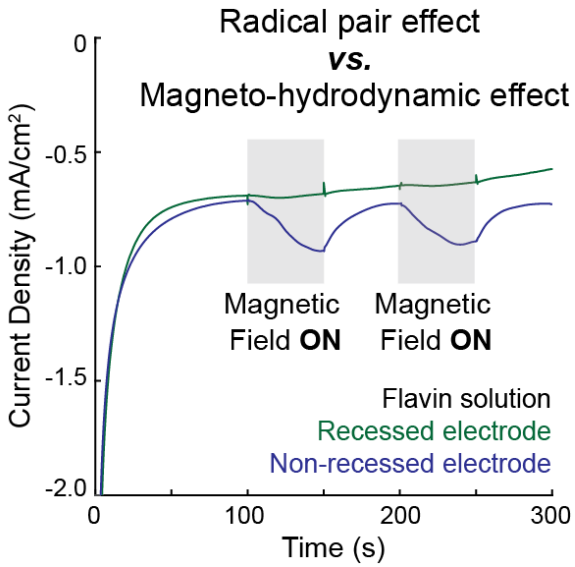

Figure 5-1: **A schematic illustrating the control of flavin redox chemistry with magnetic fields**

5.2 Background and Motivation

5.2.1 Radical Pair and Singlet-Triplet Interconversion

A radical pair, which is composed of two unpaired electrons, plays an important role as an intermediate in the numerous chemical reactions. Generally, radical pairs are formed during the cleavage of the covalent bond in single molecule or an electron transfer process between two molecules (Equation5.1):

$$\begin{aligned} R_1 - R_2 \quad &\longrightarrow \quad R_1^{\bullet} + R_2^{\bullet} \\ A + B \quad &\longrightarrow \quad A^{\bullet +} + B^{\bullet -} \end{aligned} \tag{5.1}$$

These processes follow the Wigner spin conservation rule; when starting molecules (R_1-R_2, A, and B) are singlets (S=0), the resulting primary radical pairs ($R_1^{\bullet}$ + $R_2^{\bullet}$ or $A^{\bullet +}$ + $B^{\bullet -}$) should be also in the singlet states [180]. After formation of the primary radical pair, its spin state is no longer stationary. Instead, the initial spin state is gradually evolved into the mixed singlet (S=0) and triplet (S=1) state through singlet-triplet intersystem crossing.

Intersystem crossing can be visualized with the simplified vector model of electron spin (Figure 5-2). All triplet and singlet states can be labeled with upward spin (α) and downward spin (β), which are pointing in the direction of an arbitrary magnetic field and that opposed to the magnetic field, respectively. The three triplet states of a radical pair are denoted as T_+, T_-, and T_0 and each state has spin configuration of $\alpha\alpha$, $\beta\beta$, and $\frac{1}{\sqrt{2}}(\alpha\beta+\beta\alpha)$, respectively. In the case of singlet state (S), its spin configuration can be labelled as $\frac{1}{\sqrt{2}}(\alpha\beta\text{-}\beta\alpha)$. The vectoral difference between T_0 and S states is phasing of two spin function products ($\alpha\beta$ and $\beta\alpha$); two spin products (vectors) are 0° out of phase in T_0 state, whereas these two spin products (vectors) are 180° out of phase in S state. During the intersystem crossing, T_0 and S states can be interconverted by rewinding one spin vector relative to each other by 180°. This type of transition between T_0 and S is called as spin rephasing transition. On the other hand, a transition between T_+, T_- and S, T_0 cannot be achieved with simple rewinding of one spin vector relative to others. Instead, spin vector should be flipped

to convert into other states (spin-flip transition) during the intersystem crossing [180].

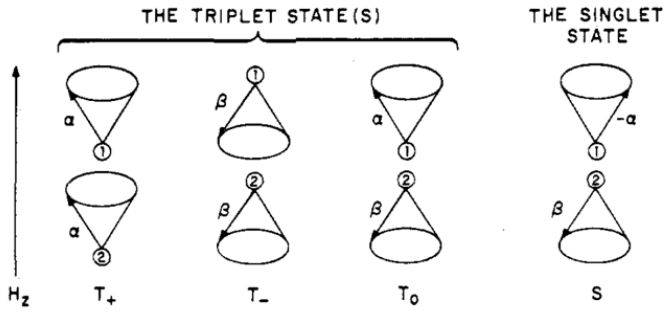

Figure 5-2: **Simplified vector model of radical pair spin states** Reprinted from [181].

Then, what factors lead to these spin transitions during intersystem crossing in a radical pair? The first is spin-orbit coupling (SOC) between the spin angular momentum of the unpaired electron and its orbital motion [182]. The SOC interaction perturbs the system, so that the spin quantum number (S) is no longer conserved anymore. However, it should be noted that SOC effect is not significant in the case of small organic radicals without containing heavy atoms [181]. More generalized factor that drives intersystem crossing is the hyperfine interaction between the spin in the molecule and its magnetic nuclei [182, 183]. The spin can experience an internal magnetic field generated from the nuclei of its own molecule. In the presence of the internal hyperfine field (B_{HFI}), spins tend to precess about the direction of the hyperfine field. If two spins in a radical pair experience different internal magnetic fields, their precession rates would be different, so that the spin rephasing transition between S and T_0 can be possible. In addition to the spin rephasing transition, as the direction of B_{HFI} is random, hyperfine interaction leads to the spin-flip transitions between T_+, T_- and S, T_0. Finally, the primary radical pair with either pure singlet or triplet state can evolve into an admixture of S, T_+, T_0, and T_- with the aid of hyperfine interaction. Likewise, this hyperfine interaction inside the molecule perturbs the system (i.e., $[B_{HFI}, S^2] \neq 0$) and allow the spin quantum number (S) to be changed. Instead, total angular momentum of molecule (F) is conserved.

5.2.2 Radical Pair Mechanism

An important feature is that only singlet radical pair can be participated in radical recombination reactions, including the reverse reactions of their formation processes, due to the spin conservation rule [180, 183]. Therefore, we can expect that the rate of spin evolution (intersystem crossing rate) is critical in determining the lifetime of these radical pairs and the kinetics of their recombination reactions. For example, if the intersystem crossing rate of primary radical pair with the initial singlet state is slowed down, we can expect that the lifetime of the radical pair decreased due to the enhanced radical recombination reactions. Additionally, when these recombination reactions are rate-determining steps in overall chemical reactions, intersystem crossing rate can influence the overall kinetics of the chemical reactions and even product yields [180, 181, 183].

The rate of spin evolution driven by hyperfine interaction can be influenced by the external magnetic field (B_0) [182]. In the presence of the external magnetic field, spins now experience the overall magnetic field (B_{tot}), which is a vector sum of the external magnetic field (B_0) and internal hyperfine fields (B_{HFI}): $B_{tot} = B_0 + B_{HFI}$ (Figure 5-3a). When the external magnetic field strength is much larger compared to the internal hyperfine field strength, the overall magnetic field is dominated by the external magnetic field. Therefore, the spins now tend to precess around the external magnetic field, precluding spin-flip transitions between T_+, T_- and S, T_0. In this case, only spin-rephasing transitions between S and T_0 can be possible. In this regard, in the presence of external magnetic field, the overall kinetics (rate) of spin evolution can be slowed down (Figure 5-3b).

Detailed magnetic field effects on the chemical reactions involving radical pairs can be estimated by solving differential equations [183–185]. Let's first consider the most simplified case. The radical pair ($A^{\bullet+}$ + $B^{\bullet-}$) is generated from reactants (A + B) through electron transfer process. This radical pair is evolved into admixture of singlet (S) and three triplet (T_+, T_-, and T_0) states through hyperfine interaction. Among these four states, only singlet radical pair $^1(A^{\bullet+} + B^{\bullet-})$ can undergo the

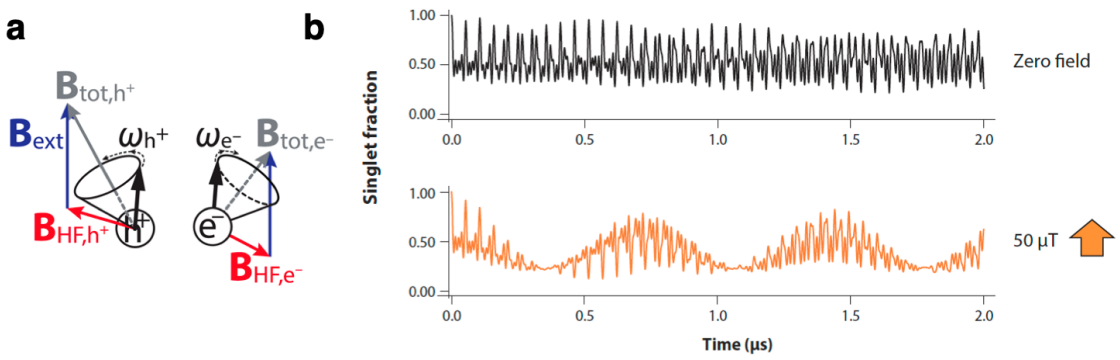

Figure 5-3: **Effects of external magnetic fields on hyperfine-induced intersystem crossing of the radical pair** a, Schematics for magnetic field effects on hyperfine-induced intersystem crossing of the radical pair. Reprinted from [182]. b, Calculated time-evolution profiles of the fraction of singlet radical pair in the absence (black) or presence (orange) of a weak external magnetic field. Reprinted from [183].

reverse reaction of its formation ($A^{\bullet+} + B^{\bullet-} \longrightarrow A + B$) due to the spin conservation rule. Then, we can calculate the time-dependent changes in concentration of reactants and the radical pair in the presence or absence of magnetic field with the following differential equations (Equation5.2):

$$\begin{aligned} \frac{d[A]}{dt} &\approx -(k_a)[A] + k_r[S] \\ Without\ external\ field: \frac{d[S]}{dt} &\approx -(k_r + 3k_{HFM})[S] + k_{HFM}([T_0] + [T_+] + [T_-]) \\ With\ external\ field: \frac{d[S]}{dt} &\approx -((k_r + k_{HFM})[S] + k_{HFM}([T_0]) \end{aligned} \tag{5.2}$$

Here, k_a, k_r, and k_{HFM} are rate constants for forward, reverse reactions of the radical pair formation and intersystem crossing rate of a radical pair induced by hyperfine interaction.

More complicated cases can be also estimated in a similar fashion. Let's assume that one of the radicals ($A^{\bullet+} + B^{\bullet-}$)) now participates in the formation of another product (C), such as the addition of a hydrogen ion to the radical ($B^{\bullet-} + H^+ \longrightarrow BH^{\bullet}$) (spin-independent process) (Figure 5-4a) [184]. Both ($B^{\bullet-}$) radical in singlet and triplet radical pairs can participate in this formation, as neither breaks down the spin conservation rule. The time-dependent kinetics of the formation

of product (C) and radical pairs can be calculated by solving following differential equations(Equation5.3):

$$\begin{aligned} \frac{d[C]}{dt} &\approx -(k_c)([S]+[T_0]+[T_+]+[T_-]) \\ Without\ external\ field: \frac{d[S]}{dt} &\approx -(k_r+3k_{HFM}+k_c)[S]+k_{HFM}([T_0]+[T_+]+[T_-]) \\ With\ external\ field: \frac{d[S]}{dt} &\approx -((k_r+k_{HFM}+k_c)[S]+k_{HFM}([T_0]) \end{aligned} \tag{5.3}$$

Here, k_c is the rate constant for the formation of product (C). Figure5-4 shows the representative changes in the radical pair and the product (C) concentration along the reaction time calculated by solving differential equations.

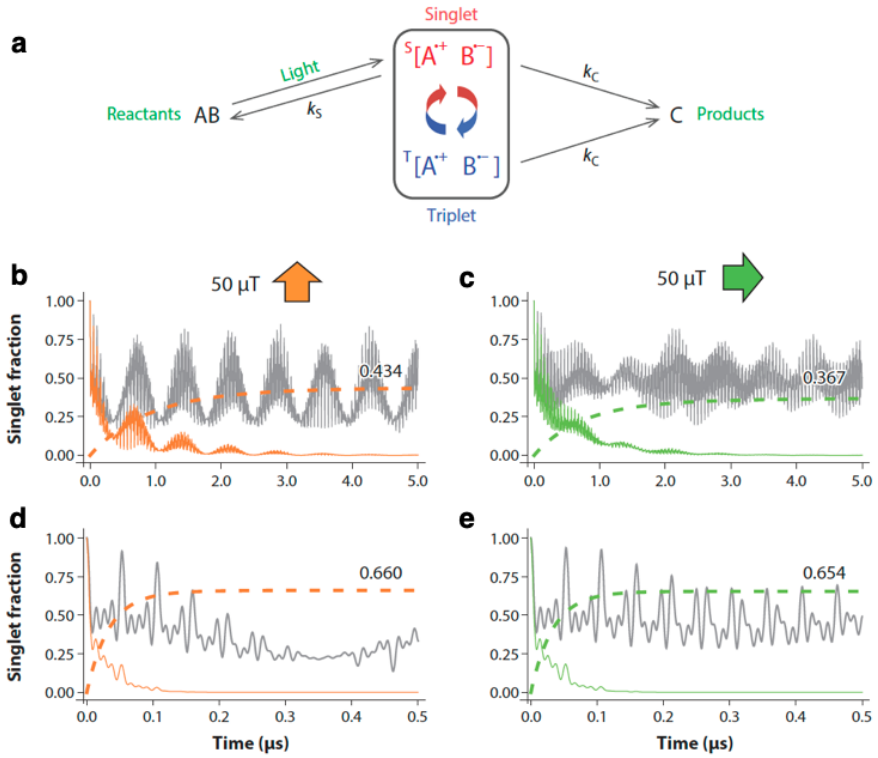

Figure 5-4: **Influence of external magnetic fields on radical-pair involving chemical reactions** a, Simplified radical-pair involved reaction scheme. b-c, Effect of a weak external magnetic field on fraction of the singlet radical pair $^1(A^{\bullet+} + B^{\bullet-})$ and the yield of final product (C) over time. Solid colored and gray lines represent the calculated fraction of singlet radical in the presence or absence of magnetic field, respectively. Dashed lines indicate the yield of the final product (C) in the presence of magnetic field. Difference between panel b and c is the direction of the magnetic field (90^o shift) Reprinted from [183].

Interestingly, in the presence of an extremely strong external magnetic field, the rate of spin evolution can be accelerated through so-called Δ g mechanism [180]. Under this condition, spin-flip transitions are still suppressed; however, spin-rephasing transitions between S and T_0 can be greatly accelerated. This is because the precession frequency difference (Δ w) between two spins, which can cause the spin-rephasing transitions between S and T_0, is linearly proportional to the overall magnetic field strength: $\Delta w \propto \Delta\ g \times B_{tot}$. As spin-rephasing transition requires rewinding one spin vector relative to each other by 180°, we can express its rate (k_{TS}) as $\Delta w/\pi$ (Figure 5-5a) [181]. Therefore, the rate of spin-rephasing transition (k_{TS}) can be largely enhanced under the strong external magnetic field (Figure 5-5b).

Figure5-5 summarizes the external magnetic field effect on the rate of spin evolution (intersystem crossing) [181, 186]. Under the weak external magnetic field, the magnetic field decreased the rate of spin evolution by suppressing the hyperfine-induced spin-flip transitions between T_+, T_- and S, T_0. As the external magnetic field strength increases, the rate of spin evolution starts to increase through Δ g mechanism. Likewise, these two counteracting magnetic field effectss allow us to accelerate or deaccelerate the rate of spin evolution with the external magnetic field strength.

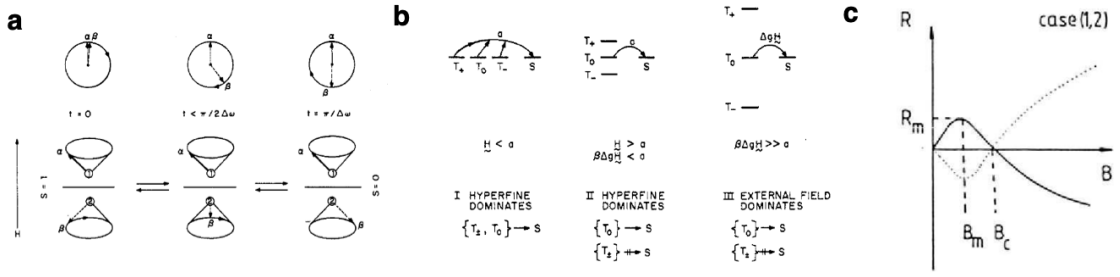

Figure 5-5: **Different magnetic field effects on singlet-triplet transition of the radical pair depending on the field intensities** a, Schematic description of the spin rephrasing transition between T_0 and S. b, Summarized magnetic field effects on intersystem crossing rate of the radical pair. When the magnetic field strength becomes larger than the magnitude of hyperfine interaction, magnetic field suppresses the hyperfine-induced spin-flip transitions between T_+, T_- and S, T_0. Under the much stronger magnetic field, intersystem crossing rate is determined by Δ g mechanism. c, Representative magnetic field effects on reaction yields along the magnetic field strength. Weak magnetic field and strong magnetic field play opposite roles in determining the reaction yields in the system (B_m: field at maximum yield (R_m) and B_c: zero-line crossing field). Reprinted from [180, 181].

5.2.3 Magnetoreception Based on Flavin Radical Pair

There is growing evidence that the radical pair mechanism plays important roles in the magnetoreception process in some bird species [183, 184, 187, 188]. In detail, it has been proposed that radical pairs generated in cryptochromes, a class of flavoproteins, could be the core units for magnetic sensing in these species (Figure 5-6a). Intraprotein electron transfer from the conserved tryptophane (TrpH) residues to the photoexcited flavin adenine dinucleotide cofactor (FAD) generates the first radical pair (RP1), ($FAD^{\bullet -}$-$TrpH^{\bullet +}$), within a 1 μs timescale (Figure 5-6b). This radical pair (RP1) is magnetic-sensitive and only singlet RP1, ^{1}($FAD^{\bullet -}$-$TrpH^{\bullet +}$), undergoes the reverse electron transfer reaction to yield FAD and TrpH. At the same time, both singlet and triplet RP1 participate in the formation of a secondary radical pair (RP2, $FADH^{\bullet}$-$Trp^{\bullet}$), which can potentially trigger the signal transduction cascade for magnetorecption in these bird species, through the proton transfer process (spin-independent process) [183].

It should be noted that these chemical reactions involving RP1 and RP2 in cryptochromes are similar to the cases described in Equation5.3, where FAD, TrpH, and RP2 are analogous to the reactants (A, B) and product C, respectively. Therefore, the reaction yield of RP2, a potential signaling chemical for magnetoreception, can be changed depending on the strength of external magnetic field. Indeed, approximately 1% of magnetic field effects on the reaction yield of RP2 has been experimentally reported in the cryptochrome at the applied field of 1 mT [184, 189]. Theoretical calculations further supported this hypothesis by showing that the reaction yield of RP2 can be changed by 0.1 % by the earth magnetic field at around 50 μT [190].

5.2.4 Magneto-hydrodynamic Effect

5.2.5 Motivation

Redox cofactors take on multitude of roles in biological processes and are essential mediators in many enzymatic reactions [191, 192]. The redox cofactors flavin adenine dinucleotide (FAD) and flavin mononucleotide (FMN), for example, are involved

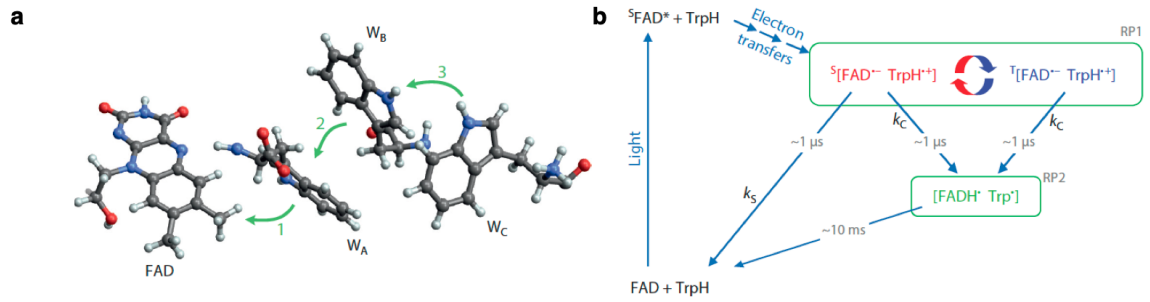

Figure 5-6: **Magnetic-field sensitive, FAD-TrpH radical pair in cryptochrome** a, Schematics for the formation of radical pair in cryptochrome. Green arrows indicate the sequential electron transfer from TrpH to FAD. b, Detailed reaction pathway (formation, intersystem crossing, elimination, and transition) of the radical pair. Reprinted from [183].

in electron transfer in flavoproteins, which regulate oxidative stress and photosynthesis [193–195]. Given their electron transfer properties, redox cofactors have been employed as building blocks in applications ranging from batteries and fuel cells to sensors [196–198].

As previously described in Section5.2.3, recent studies have suggested that magnetic fields influence the chemistry of redox cofactors in biological systems. In detail, it has been proposed that external magnetic fields could affect the singlet-triplet interconversion rate of FAD-based radical pairs formed in the flavoprotein cryptochrome. The effect of the magnetic field on the spin symmetry of the radical pair in the cryptochrome has been suggested as one of the possible origins of magnetoreception, a mechanism that allows certain species to sense Earth's magnetic field [183, 183, 187]. Given the importance of redox cofactors in biology and the growing interest in these molecules for engineering applications, it is essential to develop a mechanistic understanding of the redox behavior of these systems under the influence of magnetic fields.

5.3 Magnetic Control of Flavin Chemistry

5.3.1 Model System: Electrochemical Reactions of Flavin Solutions

Unfortunately, it has been extremely challenging to investigate flavin chemistry in flavoproteins, including cryptochrome, under magnetic fields due to their complicated structures and reaction pathways. In this regard, we investigated the influence of magnetic fields on flavin chemistry by leveraging the electrochemical reduction of FMN as a simplified model system. As shown in Figure5-7, electrochemical reactions of FMN involve the formation of a radical intermediate ($FMNH^{\bullet}$), implying that the electrochemical behavior of flavin could be magnetic-field sensitive similar to the flavin radical pair in cryptochrome (Figure 5-6). Furthermore, electrochemical reduction of FMN to $FMNH_2$ in aqueous solutions is a $2e^-/2H^+$ process, like what occur in various flavoproteins [199, 200].

We explored the influence of the magnetic field on electrochemical reduction reactions at various applied voltages, field intensities, and electrode configurations. We proposed several putative radical pair-based mechanisms and tested whether magnetic field-induced current increases in FMN solution were mediated by radical pair intermediates. Employing a combined experimental and theoretical approach, we found that the intermediates had negligible influence on current changes in FMN solution. Instead, our analyses suggest that the magneto-hydrodynamic effect is predominantly responsible for the magnetic field sensitivity of FMN solution, which is further confirmed for a range of electrochemical reactions involving other redox cofactors.

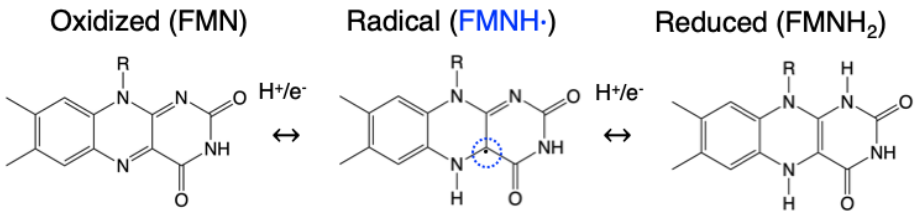

Figure 5-7: **A Schematic for electrochemical reduction of FMN to $FMNH_2$ through the formation of FMNH radical intermediate ($FMNH^{\bullet}$)**

5.3.2 Design of Electromagnetic-Electrochemical Apparatuses

To examine whether redox behavior of FMN is sensitive to magnetic fields, we built a three-electrode electrochemical cell, which was integrated into a high-power electromagnet comprised of two coils to generate a uniform magnetic field along the x-direction. Housed in a nuclear magnetic resonance tube (7.5 mm in diameter), two platinum (Pt) wires (500 μm in diameter), which served as cathode and anode, were aligned in parallel to the z-axis and positioned 5 mm apart along the x-axis. The Ag/AgCl pseudo-reference electrode was located between the two Pt electrodes (Figure 5-8). A solution of FMN (20 mM) in phosphate buffered saline (PBS) was used as an electrolyte.

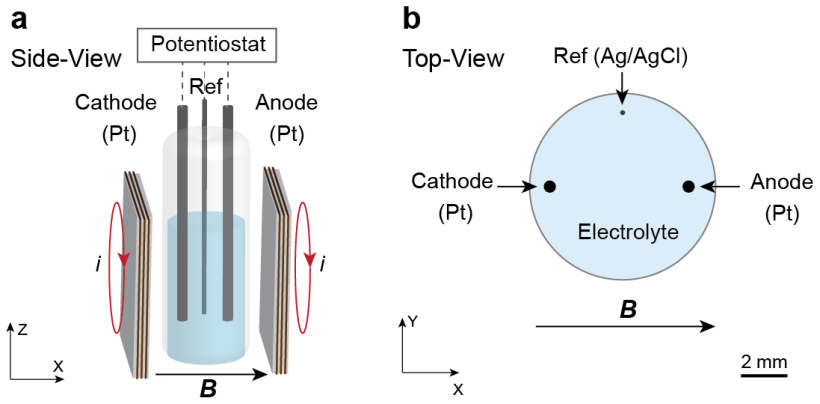

Figure 5-8: **Schematics for the electromagnetic-electrochemical apparatus with Pt wire electrodes** a, An experimental setup using Pt wire electrodes to investigate the influence of the magnetic field on the electrochemical reduction of FMN solutions. b, A schematic illustrating magnetic field direction and three-electrode cell configuration used for electrochemical analyses.

5.3.3 Magnetically-induced Changes in Faradaic Currents

The influence of magnetic field on the electrochemical properties of FMN in solution was first evaluated by CV. CV curves for the FMN solution were recorded with a potentiostat between 0 and –1.25 V versus Ag/AgCl, while a static magnetic field of 1 T was applied to the electrochemical cell. We observed increased reductive currents in the FMN solution between –0.25 and –1.20 V in the presence of the magnetic field. The influence of the magnetic field in this voltage range was also evident in

chronoamperometry measurements of FMN solutions. A static magnetic field of 1 T was applied for 37 s at times t_1=113 s and t_2=212 s during the measurements. With the application of the magnetic field the reductive currents rapidly increased and then slowly saturated over time. The magnetic field-driven current increases gradually disappeared when the magnetic field was turned off (Figure 5-9a). We found that the normalized current density increase induced by magnetic fields ($\Delta J/\mathrm{J}_0$, where J_0 indicates the reductive current density in the absence of a magnetic field) was dependent on the applied voltage. Higher magnetic field-induced current changes ($\Delta \mathrm{J}/J_0$) were observed at higher negative voltages up to –1.0 V. The effects were greatly diminished at –1.25 V, a potential at which the hydrogen evolution reaction (HER) dominated over the FMN reduction reaction [201] (Figure 5-9b). We confirmed negligible solution temperature changes (<1°C) throughout the periods (37 s) of magnetic field (1 T) application, indicating that observed current increases were unlikely driven by thermal fluctuations (Figure 5-9c).

The influence of the magnetic field on the reductive currents in the FMN solution also varied with the intensity of the magnetic field. As shown in Figure5-9d, the application of higher magnetic fields induced a more significant change in reductive currents in 20 mM FMN solution at –1.0 V versus Ag/AgCl. Robust increases in reductive currents in the FMN solution (as marked by $\Delta \mathrm{J}/J_0 \geq 10$ %) were observed in the presence of magnetic fields $\geq$ 150 mT, and the extent of normalized current density changes ($\Delta \mathrm{J}/J_0$) gradually increased with increasing the magnetic field intensity (Figure 5-9e). The dependence of $\Delta \mathrm{J}/J_0$ on the applied magnetic field strength further supported that the reductive currents in the FMN solution were indeed modulated by the external magnetic fields.

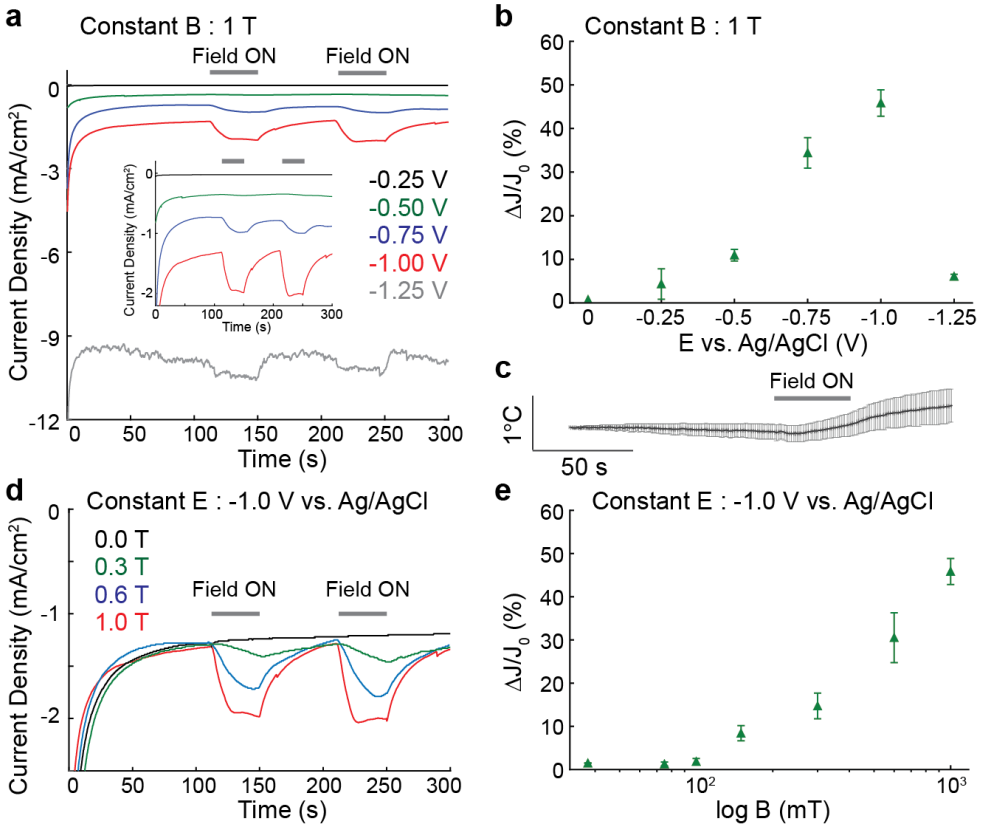

Figure 5-9: **Magnetically induced changes in reductive currents in the FMN solutions at various applied voltages and magnetic field intensities** a, Chronoamperometry profiles of 20 mM FMN solution at voltages ranging from –0.25 V to –1.25 V versus Ag/AgCl. During chronoamperometry, a magnetic field of 1 T was turned on at 113 s and 213 s and applied for 37 s (gray bars). The inset shows the enlarged chronoamperometry profiles. b, Normalized current increases (mean ± standard error of the mean (s.e.m.)) induced by a 1 T magnetic field during the electrochemical reduction of 20 mM FMN solution at different applied voltages (n = 1 for 0 V, n = 2 for –0.25 V, n = 3 for –0.5 V, n = 4 for –0.75 V, n = 16 for –1.0 V, n = 2 for –1.25 V). c, Solution temperature changes before, during, and after the application of a magnetic field of 1 T. The solid lines and shaded areas represent the mean and s.e.m., respectively (n = 4). d, Chronoamperometry profiles of 20 mM FMN solution at –1.0 V. Magnetic fields of 0, 0.3, 0.6, and 1.0 T were turned on at 113 s and 213 s and applied for 37 s (gray bars). e, Dependency of the normalized current increases (mean ± s.e.m.) induced by magnetic fields during electrochemical reduction of 20 mM FMN solution at -1.0 V on the applied magnetic field (n = 3 for 37.5 mT, n = 3 for 75 mT, n = 3 for 100 mT, n = 3 for 150 mT, n = 7 for 300 mT, n = 3 for 600 mT, n = 16 for 1000 mT).

5.4 Mechanistic Studies on Magnetic Field Effects on Flavin Reactions

5.4.1 Magneto-hydrodynamic effect in Flavin Solutions

To understand the underlying mechanism of the magnetically induced current changes in the FMN solution, we first related the electrochemical reaction timescale to the diffusion rate of FMN in solution. Based on the electron-transfer (reduction) rate constant and diffusion coefficient of FMN in solution [199], the Damköhler number of our system was calculated as ∼12500, indicating that the overall reaction is a diffusion-limited process. This was further corroborated by the experimental observation that peak currents during FMN reduction are proportional to $v^{1/2}$ [202], where v is the scan rate during CV measurements (Figure 5-10a). These findings implied that the observed current changes induced by a magnetic field are predominately related to the mass transport of FMN in solution.

To further confirm this, we functionalized the surface of an indium tin oxide (ITO) electrode with a FMN layer. We then tested whether the magnetic field still had an observable effect on the electrochemical reduction of the surface-bound FMN. CV analysis of the functionalized ITO electrodes revealed the characteristic FMN redox peaks [199, 203] in the absence of free FMN in the solution, confirming the presence of surface-bound FMN on the electrodes (Figure 5-10b). At –0.75 V versus Ag/AgCl, the application of a 1 T magnetic field did not evoke any noticeable current increases in the FMN-functionalized ITO electrodes, whereas robust current increases were found in free FMN solution at the same applied voltage (Figure 5-10c). This control experiment further suggests that the current increases found in free FMN solution upon application of a magnetic field can be attributed to improved mass transport of FMN towards the Pt wire inside the cell.

The effect of magnetic fields on mass transport of free FMN towards the Pt wire were then investigated by solving the coupled magneto-hydrodynamic equations of charged species in the presence of a supporting electrolyte [204–206]. Specifically, we

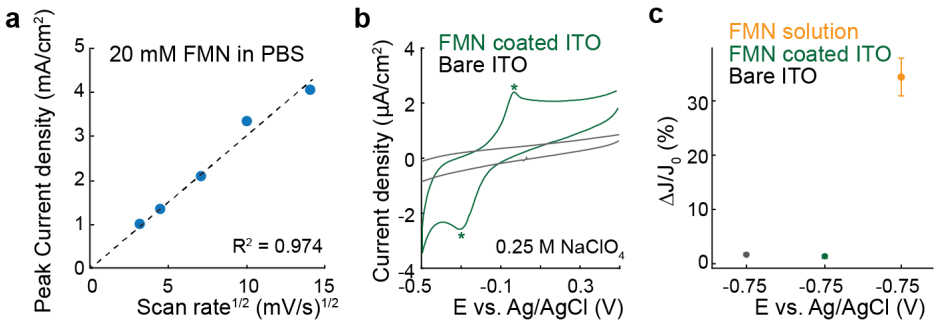

Figure 5-10: **Diffusion-limited, electrochemical reductions of FMN solution** a, Dependence of the peak current on the square root of the scan rate during electrochemical reduction of 20 mM FMN. b, CV curves of FMN-functionalized (green) or bare (black) ITO electrodes in 0.25 M NaClO4 solution. Redox features of surface-bound FMN can be observed (*) (scan rate: 50 mV/s). c, Normalized current increases (mean ± s.e.m.) induced by 1 T magnetic fields during chronoamperometry measurements for the FMN-functionalized (green) or bare (black) ITO electrodes at –0.75 V versus Ag/AgCl (n = 4 for the FMN-functionalized ITO, n = 3 for bare ITO, n = 4 for the FMN solution). Negligible influence of the magnetic field on current was found for FMN-functionalized or bare ITO electrodes as compared to that observed in 20 mM FMN solution after the application of a 1 T magnetic field at –0.75 V versus Ag/AgCl (orange).

focused on the experimentally accessible regime of large Damköhler (∼12500), large Peclet (∼30000), and small Reynolds (∼1) numbers, indicative of diffusion-limited reactions in the presence of laminar convection. Calculated chronoamperometry profiles upon application of an external magnetic field were qualitatively consistent with experimental observations, albeit predicting a stronger reductive current response to the magnetic field than that observed (Figure 5-11a). These differences can likely be attributed to the slight differences in shape, size, and surface roughness between the actual electrodes and the modeled counterparts having a perfectly round configuration and a flat surface. Consistent with previous reports [207, 208], the extent of the magnetically induced current increase has been estimated to depend sensitively on these parameters (Figure 5-12). The Lorentz force-induced convection was visualized with the streamlines of the supporting electrolyte on a plane perpendicular to the direction of the magnetic field. As a 250 mT magnetic field was switched on (t∼95s), the magnitude of the convective electrolyte flow increased, reaching a maximum just before it was switched off (t∼155s), and rapidly recovered to nearly static flow in the absence of the field (Figure 5-11b). Rotational electrolyte flow around the Pt

wire inside the cell was apparent in the presence of a magnetic field, consistent with Lorentz force dynamics [206]. Together, the theoretical model revealed that the current increases at Pt wires upon application of a magnetic field are mainly attributable to the Lorentz force-induced convection effect.

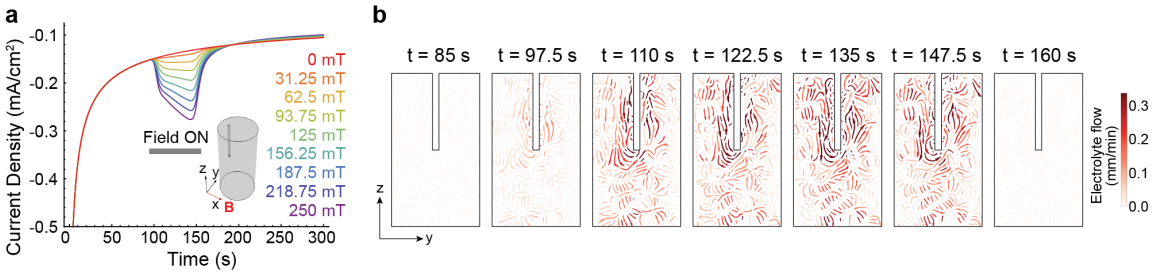

Figure 5-11: **Calculated chronoamperometry profiles and convective electrolyte flow in FMN solution in the presence of external magnetic fields** a, Calculated chronoamperometry profiles of 20 mM FMN solution upon the application of magnetic fields with magnitudes ranging between 0 - 250 mT. Inset shows the 3D domain used in the calculation and the direction of the external magnetic field (red coordinate arrow). Upon application of magnetic field, reductive currents increase, recovering to the diffusion-limited reductive currents when the field is turned off. b, Induced convective electrolyte flow on a plane normal (y-z) to the direction of the applied magnetic field as a function of time before and after the application of a 250 mT magnetic field. The apparent (counter-clockwise) rotation around the electrode is indicative of a Lorentz force.

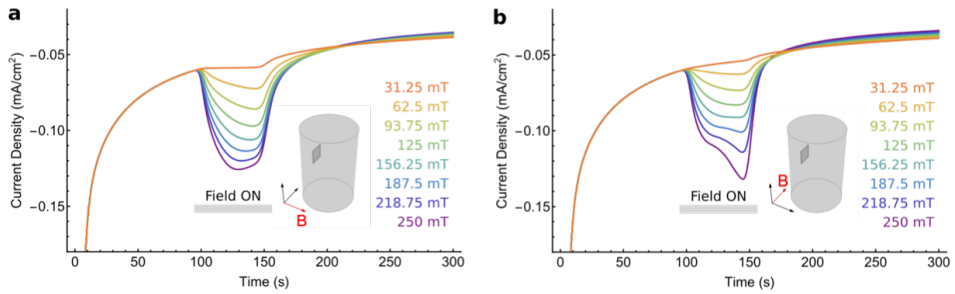

Figure 5-12: **Calculated chronoamperometry profiles in FMN solution with various electrode configurations upon application of magnetic fields** a-b, Calculated chronoamperometry profiles for planar electrodes of similar surface area as the cylindrical electrodes used to acquire data in Figure5-11 upon application of magnetic fields varying between 31.25 mT and 250 mT (a) perpendicular and (b) parallel to the electrode surface.

5.4.2 Recessed Electrode System

To minimize the Lorentz force-induced convection inside the cell and decouple the magneto-hydrodynamic effect and a possible radical-pair effect in the electrochemical reduction of FMN solutions, a new electrochemical system was built inspired by previous studies [209–211]. It has been shown that the macroscopic magneto-hydrodynamic effect is minimized in systems with recessed electrodes when the charge transport direction is parallel to the magnetic field direction [209–211]. Therefore, the newly designed cell features a recessed cathode and anode to ensure that the charge transport direction is homogenous and perpendicular to the electrode surface. In our system, Pt foils (25 μm thick) on aluminum current collectors were utilized as a recessed cathode and anode, fully covering two circular holes at the sides of the cell. An Ag/AgCl reference electrode was placed near the cathode, and a Nafion membrane was introduced between electrodes to prevent electrolyte convection near the anode from influencing the electrochemical reaction at the cathode [210]. A uniform magnetic field was generated using a large-scale, high-power electromagnet, and the fully-assembled cell (20 mm × 20 mm × 20 mm) was inserted between two coils of the electromagnet (Figure 5-13).

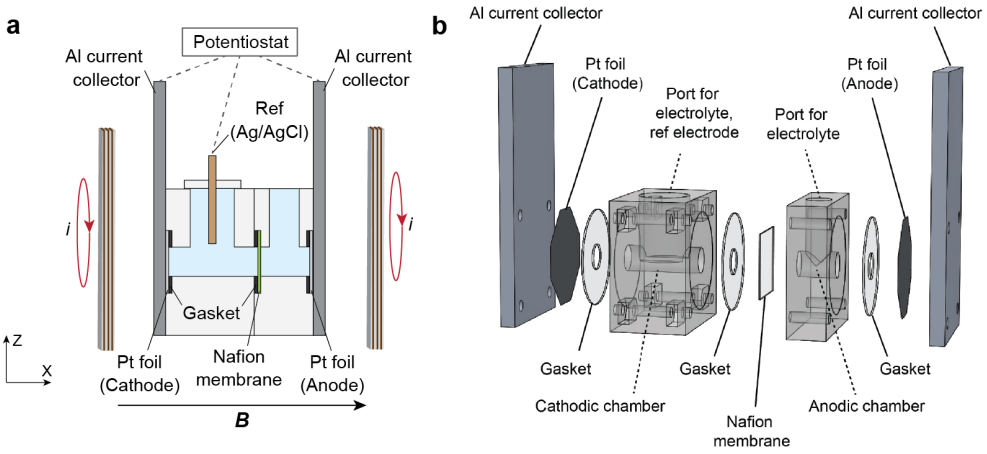

Figure 5-13: **Design of an electrochemical cell with recessed Pt foil electrodes** a, An experimental setup using recessed Pt foil electrodes to minimize the magneto-hydrodynamic effect and ensure charge transport perpendicular to the electrode surface. b, Detailed schematics of the recessed electrode-based electrochemical cell.

The magneto-hydrodynamic effect on the electrochemical reduction of FMN solu-

tion was attenuated in the recessed electrode-based system, consistent with previous reports [209–211]. When a magnetic field of 1 T was applied parallel to the charge transport direction, the extent of the current change at the recessed Pt foil at –0.75 V versus Ag/AgCl was only 4.4 ± 0.4 %, which was significantly smaller than the current change observed in the non-recessed Pt wire (34.5 ± 3.8 %) setup at identical experimental conditions (Figure 5-14). Note that the sharp peaks at 100, 150, 200, and 250 s correspond to the inductive currents associated with the change of the magnetic flux while turning the magnetic field on or off.

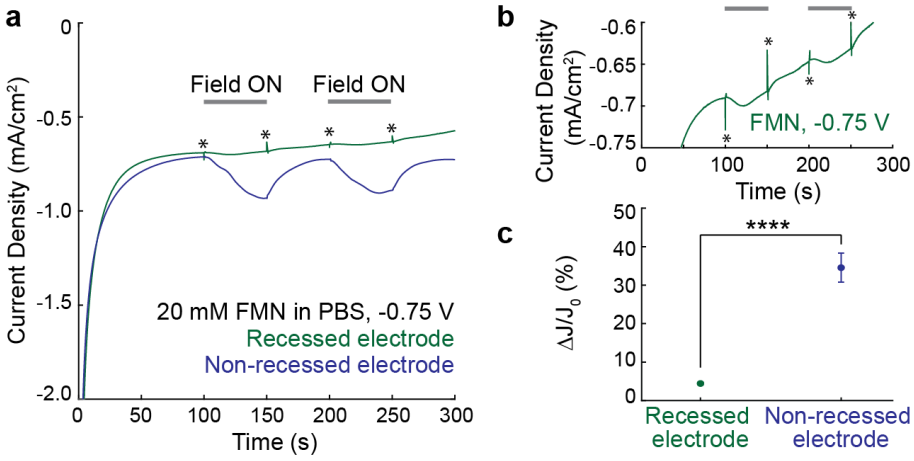

Figure 5-14: **Magnetically-induced current increases in FMN solutions in non-recessed or recessed electrode systems** a, Representative chronoamperometry profiles of the reduction of 20 mM FMN solution in the recessed electrode (green) and non-recessed setup (blue) at –0.75 V versus Ag/AgCl. A 1 T magnetic field was applied during chronoamperometry measurements for each solution (gray bars) b, The enlarged chronoamperometry curves of b in the recessed electrode setup. c, Normalized current increases (mean ± s.e.m.) induced by 1 T magnetic fields during the electrochemical reduction of 20 mM FMN solutions on recessed electrodes (green) and non-recessed Pt wire electrodes (blue). The statistical significance of a decrease in current changes at recessed electrodes as compared with non-recessed electrodes was found (n = 8 for recessed electrode, n = 4 for non-recessed electrode, **** $p = 3.8 \times 10\text{-}7 < 0.0001$).

We also confirmed that at –0.75 V hydrogen bubbles [209, 211, 212], side-products at the cathode, have a negligible contribution to the magneto-hydrodynamic effect. CV curves of PBS without FMN showed a sharp increase in the current at approximately –0.85 V associated with HER (Figure 5-15a), and we did not observe any significant current increases induced by magnetic fields at –0.75 V where HER is neg-

ligible. HER currents at –1.00 V increased by 5.2 ± 0.7 % with the application of a 1 T magnetic field (Figure 5-15b-d), consistent with prior studies [209, 211, 212].

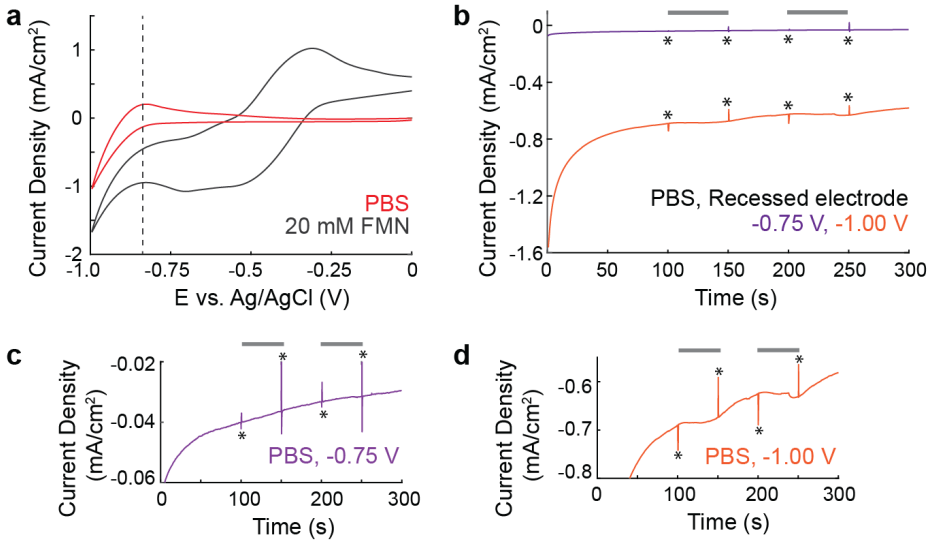

Figure 5-15: **Effects of hydrogen bubbles on current changes in FMN solutions upon application of magnetic fields** a, CV curves of 20 mM FMN solution (black) or PBS (red) in the recessed electrode setup (scan rate: 20 mV/s). The hydrogen evolution reaction on the electrode appeared at approximately –0.85 V. b, Representative chronoamperometry profiles of the recessed electrode setup in PBS at –0.75 V (purple) and –1.0 V (orange). A 1 T magnetic field was applied during chronoamperometry measurements for each solution (gray bars). c-d, The enlarged chronoamperometry curves of f at –0.75 V (c) and –1.0 V (d). Negligible magnetic-field induced current changes were found at –0.75 V(c), while slight increases in currents were recorded at –1.0 V (d).

5.4.3 Radical-Pair Effect in Flavin Solutions

After confirming that the macroscopic magneto-hydrodynamic effect is minimized in the recessed electrode configuration, we explored the possibility of radical pair effects in electrochemical reduction of FMN solution at the recessed electrode interface. Growing evidence suggests that magnetic fields can regulate the singlet-triplet transitions in radical pair intermediates involving $H^{\bullet}$ through accelerating the precession rate of each radical [213], referred to as the Δ g mechanism [180, 181], or modulating the spin-relaxation of the radical [214]. Based on these insights and a well-known proton-coupled electron transfer reduction mechanism in FMN [199,215], we proposed an electrochemical FMN reduction pathway involving the formation of a [$FMNH^{\bullet} \cdots H^{\bullet}$] radical pair intermediate. Due to the Pauli exclusion principle, only the singlet ^{S}[$FMNH^{\bullet} \cdots H^{\bullet}$] radical pair can recombine to form the final product $FMNH_2$. We hypothesized that magnetic field application may accelerate the overall reduction rate of FMN at 1 T by facilitating transitions between the spin triplet and singlet states through the Δ g mechanism(Figure 5-16a).

To test this hypothesis, we prepared deuterium (D) isotope-based PBS solution containing 20 mM FMN. As $H^{\bullet}$ and $D^{\bullet}$ radicals have different ground state spins and gyromagnetic ratios [183, 216], we anticipated significant differences in the extent of the effects of the magnetic fields on the kinetics of ^{T}[$FMNH^{\bullet} \cdots H^{\bullet}$] $\rightarrow$ ^{S}[$FMNH^{\bullet} \cdots H^{\bullet}$] spin evolution and the corresponding magnetically induced changes in the current densities. Interestingly, no statistically significant differences in $\Delta J/J_0$ were found between the H-based 20 mM FMN solution and the D-based counterpart (Figure 5-16b). Furthermore, the H/D kinetic isotope effect (KIE) value was below 1.5, indicating that protons, which could be the source of $H^{\bullet}$ in the radical pair, are likely not involved in the rate-determining step [217] (Figure 5-16c,d). These results suggest that the influence of the magnetic field on the electrochemical reduction of FMN at the recessed electrode is unlikely mediated by a radical pair mechanism involving $H^{\bullet}$.

We then explored alternative reaction pathways involving radicals. It has been proposed that flavin forms pairs with other radicals in flavoproteins, including the

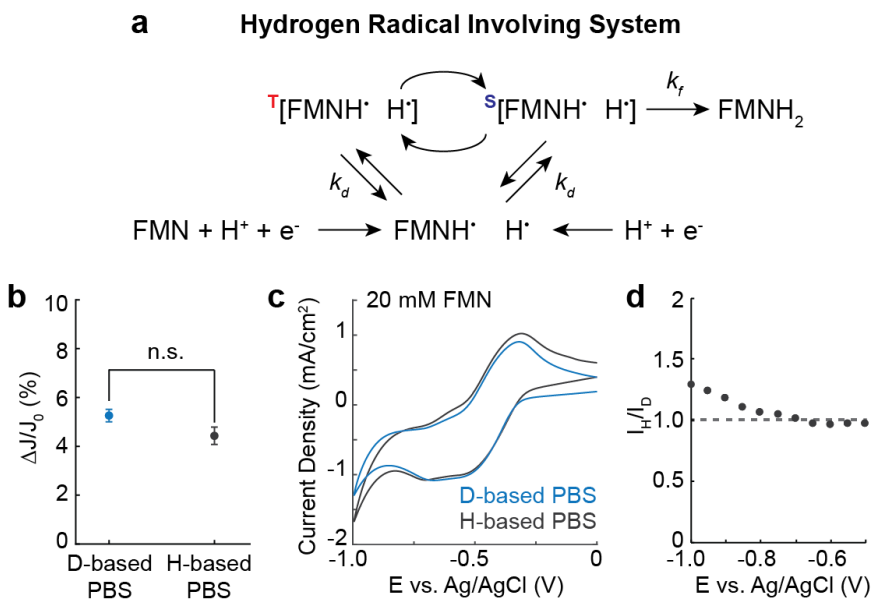

Figure 5-16: **Negligible effect of FMNH$^\bullet$-H$^\bullet$ radical pair on magnetic field sensitivity of FMN solutions** a, A hypothesized reaction scheme for the electrochemical reduction of FMN through the formation of a radical pair comprised of a FMNH$^\bullet$ and a H$^\bullet$. The radical pair can diffuse apart with the rate constant k_d, and spin-selective formation of $FMNH_2$ from the singlet radical can occur with the rate constant k_f. b, Magnetically-induced normalized current increases (mean ± s.e.m.) during the electrochemical reduction of 20 mM FMN dissolved in D-based PBS (blue) or H-based PBS (gray) solutions on recessed electrodes (n =4 for D-based PBS, n = 8 for H-based PBS). No statistical differences were observed, as confirmed by a two-sided student's t-test ($p = 0.16 > 0.05$). c, CV curves of 20 mM FMN dissolved in D-based PBS (blue) or H-based PBS (gray) solution in the recessed electrode setup (scan rate: 20 mV/s). d, Voltage-dependent I_H/I_D values calculated from (c). I_H and I_D represent reductive current densities measured in H-based PBS and D-based PBS solution, respectively.

tryptophan radical, the ascorbic acid radical, and superoxide ($O_2^{\bullet-}$) [184,190,218,219]. Among these, superoxide could be formed through an electrochemical reduction of O_2 present in the solution [220]. Thus, we proposed an alternative FMN reduction pathway that includes the formation of a [FMNH$^\bullet$ $\cdots$ $O_2^{\bullet-}$] radical pair intermediate. We hypothesized that the magnetic field could increase overall reaction rates by facilitating the spin evolution from ^{S}[FMNH$^\bullet$ $\cdots$ $O_2^{\bullet-}$] to ^{T}[FMNH$^\bullet$ $\cdots$ $O_2^{\bullet-}$] through the Δ g mechanism. Note that electron transfer from $O_2^{\bullet-}$ to FMNH$^\bullet$, that could lead to the formation of the final product $FMNH_2$ and O_2, is only allowed in the triplet state ^{T}[FMNH$^\bullet$ $\cdots$ $O_2^{\bullet-}$] considering that the electronic ground state of O_2 is a triplet (Figure 5-17a). To test this hypothesis, we examined whether the influence of the

magnetic field on the electrochemical reduction of FMN depended on the presence of O_2 dissolved in the solution. By repeating the chronoamperometry experiments in solutions purged with N_2, a common approach for reducing O_2 concentration [221–223], no significant differences on magnetically induced current increase at 1 T were observed as compared to the normal solution preparation (Figure 5-17b). These results indicate negligible effects of superoxide on magnetically-induced current increases at the recessed electrode, potentially due to the extremely fast spin relaxation of the superoxide (within a nanosecond) even if a [$FMNH^{\bullet} \cdots O_2^{\bullet -}$] radical pair intermediate existed [224].

Finally, we employed Trolox (6-hydroxy-2,5,7,8,-tetramethylchroman-2-carboxylic acid), a water-soluble free-radical scavenger [225], to quench radicals potentially formed during the electrochemical reduction of FMN. The addition of Trolox to the FMN solution did not elicit significant changes in peak currents or peak potentials during CV measurements, indicating that radicals are not involved in the rate-determining step (Figure 5-17c). Furthermore, similar current changes after the application of a magnetic field were still observed in the presence of Trolox (Figure 5-17d). Together, these results provide evidence that small increases in Faradaic currents at –0.75 V under applied magnetic fields are unlikely mediated by a radical pair mechanism.

5.4.4 Dominant Magnetic Field Effect in Flavin Solutions

Overall, our findings suggest that the contribution of the radical pair effect on electrochemical reduction of FMN solutions is negligible even in the recessed electrode-based system. The observed small current changes at –0.75 V versus Ag/AgCl upon the application of a magnetic field of 1 T are most likely caused by edge effects at the electrode [226, 227], the surface roughness of the electrode and the supporting current collector, as well as microscale hydrogen bubbles, although the quantity of the latter should be very small (Figure 5-15). Previous reports indicate that the Lorentz force-induced convection and the resulting current changes depend sensitively on the edge effects and surface roughness due to the fluctuation of the charge transport direction

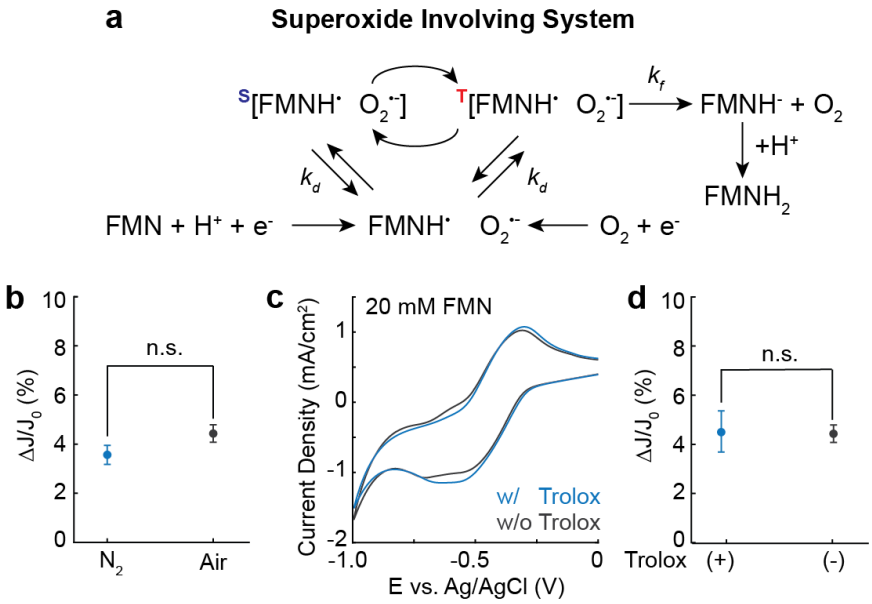

Figure 5-17: **Control experiments demonstrating negligible influence of FMNH•-based radical pair on magnetic field sensitivity of FMN solutions** a, Proposed reaction scheme for the electrochemical reduction of FMN through formation of a radical pair comprised of a FMNH• and a superoxide. b, Magnetically-induced normalized current increases (mean ± s.e.m.) during the electrochemical reduction of 20 mM FMN solution purged with 100% N_2 (blue) or air (78% N_2 and 21% O_2) (gray) in the recessed electrode setup (n =8 for air-purged solution, n = 5 for N_2-purged solution, p = 0.14 > 0.05). c, CV curves of 20 mM FMN solution in the presence (blue) or absence (gray) of Trolox in the recessed electrode setup (scan rate: 20 mV/s). d, Magnetically induced normalized current increases (mean ± s.e.m.) during the electrochemical reduction of 20 mM FMN solution in the presence (blue) or absence (gray) of Trolox on recessed electrodes (n = 8 with Trolox, n = 6 without Trolox, p = 0.91 > 0.05).

at the electrode [209, 227]. In accordance with previous findings [209, 226, 228], our simulation results showed that the surface roughness of the electrode can cause a noticeable magneto-hydrodynamic effect and induce current changes upon magnetic field application.

5.5 Generalized Magnetic Field Effects on Redox Cofactor Solutions

To assess the generality of our results and evaluate the effect of Lorentz force-driven convection on cofactor redox reactions, we investigated the influence of magnetic fields on Faradaic currents in solutions of other cofactors, including flavin adenine dinucleotide (FAD), nicotinamide adenine dinucleotide (NADH), and ascorbic acid (AA). Note that FAD is an electron-accepting cofactor in reductive conditions [199], whereas NADH and AA are electron-donating cofactors in oxidative conditions [229, 230]. The redox features of the three cofactors were examined by CV, and distinctive reductive or oxidative currents were found in 20 mM FAD, NADH, and AA solutions, respectively (Figure 5-18a). At –0.75 V versus Ag/AgCl, significant increases in normalized current densities of FAD were induced by the application of a magnetic field of 1 T in the non-recessed Pt wire-based system, whereas negligible variations in currents densities were observed in the recessed Pt foil-based system in the identical reaction conditions. Similarly, robust magnetic field-driven enhancements of Faradaic currents were found during the electrochemical oxidation of 20 mM NADH and AA solutions at +1.0 V versus Ag/AgCl in the non-recessed electrode-based system, while a magnetic field of 1 T induced significantly smaller changes in normalized current densities of NADH and AA in the recessed-electrode setup (Figure 5-18b). Together, these findings indicate that the magneto-hydrodynamic effect was not limited to the electrochemical reduction of FMN but affected all diffusion-limited electrochemical reactions on the non-recessed electrodes. Furthermore, these results further highlight the need for careful design of electrochemical cells while investigating the effects of magnetic fields on electrochemical reactions.

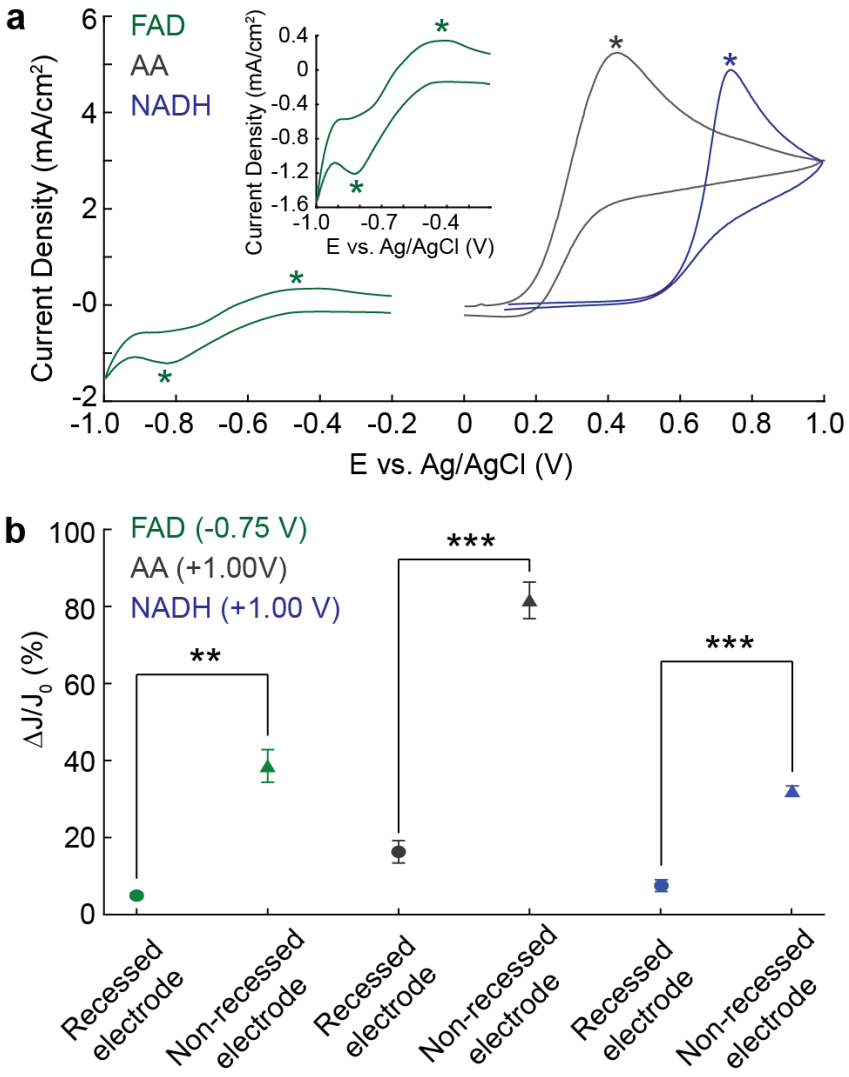

Figure 5-18: **Magnetic field effects on diffusion-limited, electrochemical reactions of other redox cofactor solutions** a, CV curves of 20 mM FAD (green), 20 mM AA (gray), and 20 mM NADH (blue) solutions (scan rate: 20 mV/s). The inset shows the enlarged CV curves of FAD solution. Redox features of FAD, AA, and NADH can be observed (*). b, Normalized current increases (mean ± s.e.m.) induced by a 1 T magnetic field during electrochemical reductions of 20 mM FAD (green) at –0.75 V versus Ag/AgCl, 20 mM NADH (blue) at +1.0 V, and 20 mM AA (gray) at +1.0 V on non-recessed Pt wire electrodes and recessed Pt foil electrodes. To record the normalized current increases, magnetic fields of 1 T were applied during chronoamperometry measurements for each solution. Significantly higher current increases were found in the non-recessed Pt wire electrode setup as compared to recessed Pt foil counterpart (n = 3 for FAD, ** $p = 0.0014 < 0.01$, n = 3 for AA, *** $p = 0.00027 < 0.001$, n = 3 for NADH, *** $p = 0.00031 < 0.001$).

5.6 Discussion and Conclusion

We explored the influence of externally applied magnetic fields on electrochemical reactions of multiple redox-cofactor solutions through a combined experimental and theoretical approach. The effects of magnetic fields on electrochemical reduction of a soluble cofactor FMN were assessed at various applied voltages, magnetic field magnitudes, and electrode configurations. We did not find any evidence that the observed magnetically-driven increases in FMN reduction currents were mediated by the interactions between the magnetic field and radical pair intermediates, as confirmed by control experiments including isotope-substitution, oxygen elimination, and the addition of a free radical quencher. Instead, we found that Lorentz force-induced convection is the dominant mechanism for magnetically driven current changes in FMN solutions. Similar magneto-hydrodynamic effects sensitive to the electrode configuration were identified in diffusion-limited, electrochemical reactions of other redox cofactor solutions. These findings suggest potential applications of magnetic fields to modulate electrochemical systems involving redox cofactor solutions, including batteries, fuel cells and electrochemical sensors. Furthermore, we envision that the experimental methodologies and theoretical model developed in this study can be extended to explore possible influence of the magnetic field on diverse electrochemical events, including radical pair-mediated, reaction-limited processes.

Chapter 6

Conclusions and Future Directions

6.1 Thesis Summary

To advance our understanding of chemical signal transduction in the nervous system and treat neurological disorders with chemotherapy, this thesis presents novel methodologies for in vivo chemical delivery based on nanomaterials chemistry, electrochemistry, and magnetism. My electrochemical and magnetochemical approaches enable 1) in situ generation and delivery of unstable and transient chemical signals and 2) remotely controlled delivery of chemical signals to specific neurons, which have not been achieved with conventional chemical delivery technologies for neuromodulation.

First, we propose an electrochemical strategy to synthesize and deliver transient and unstable chemical signals to targeted neural circuits. Rationally designed nanoscale electrocatalysts produce one of the transient chemical signals, NO, from benign precursors in the presence of modest electric fields. The NO release kinetics can be quantitatively controlled by varying the applied voltage and type of electrocatalyst. Electrochemically produced NO modulates diverse NO-dependent signaling pathways in a spatiotemporally controlled manner. This electrochemical system is implemented in an implantable microscale probe through multimaterial fiber drawing, allowing for the mechanistic studies of NO physiology in the mouse brain. We demonstrate that this electrochemical approach could be generalizable as a means of producing other unstable and transient chemical species in vivo. By introduc-

ing molecular electrocatalysts that generate CO, a gaseous and transient messenger molecule, from the biocompatible precursor, we develop an electrochemical system that affords the modulation of CO-mediated cell signaling at the microscale.

In the second part of this thesis, we focus on developing a magnetochemical approach for wireless delivery and control of chemical signals without tethered hardware. We design nanotransducers comprised of MNPs and degradable polymeric scaffolds to convert non-invasive magnetic field cues into protons. MNP heating under AMFs triggers a hydrolytic degradation of surrounding polymeric scaffolds, releasing protons into the extracellular space. Proton release kinetics can be tuned by altering the polymer chemistry or AMF stimulation parameters. Remotely controlled proton release from nanotransducers activates acid sensing ion channels and regulates proton-mediated respiratory behaviors in mice. We extend our magnetochemical approach to modulate chemical reactions involving cofactors, which mediate diverse enzymatic processes in the nervous system. By employing the flavin cofactor as a model system, we demonstrate that the reaction kinetics of redox cofactors can be controlled by external magnetic fields, suggesting potential applications of magnetic fields for the wireless modulation of redox chemistry in the brain.

We envision that our electrochemical and magnetochemical strategies to deliver chemical signals can facilitate mechanistic studies of the roles of these molecules and advance their therapeutic potential. In the following sections, we propose further steps to expand the approaches towards other chemical signals and discuss potential applications in neuroscience studies.

6.2 Outlook

6.2.1 Perspective on Electrochemical Systems

The electrochemical system presented in this thesis can be further expanded to produce other transient chemical species. For example, reaction oxygen species (superoxide, hydrogen peroxide) [221] and gaseous neurotransmitter (hydrogen sulfide) [231] can be generated via the following electrochemical reactions (Equation 6.1):

$$\begin{aligned} O_2 + e^- &\longleftrightarrow O_2^{\bullet -} \\ O_2 + 2e^- + 2H^+ &\longleftrightarrow H_2O_2 \\ H_2O_2 + 2e^- + 2H^+ &\longleftrightarrow 2H_2O \\ S + 2e^- + 2H^+ &\longleftrightarrow H_2S \\ SO_4^{2-} + 8e^- + 10H^+ &\longleftrightarrow H_2S + 4H_2O \end{aligned} \tag{6.1}$$

Furthermore, electrochemical reactions can be employed to regulate redox mediators (vitamins and their derivatives, metal ions, and other radicals), which play an important role in downstream in neuron signaling, according to the following reactions [232] (Equation 6.2):

$$\begin{aligned} FMN + 2e^- + 2H^+ &\longleftrightarrow FMNH_2 \\ NAD^+ + e^- + H^+ &\longleftrightarrow NADH \\ cyt(Fe^{3+}) + e^- &\longleftrightarrow cyt(Fe^{2+}) \\ RS^{\bullet} + e^- &\longrightarrow RS^- \\ GS^{\bullet} + e^- &\longrightarrow GS^- \end{aligned} \tag{6.2}$$

where NAD^+ and *cyt* are oxidized forms of nicotinamide adenine dinucleotide and cytochrome, respectively, and RS^- and $GS^{\bullet}$ are cysteine- and glutathione-thiyl radicals, respectively.

To realize these systems, rational design of electrocatalysts, precursors, starting compounds to generate chemical signals, and counter electrodes are necessary. First, it is important to develop electrocatalysts, which can generate or modulate targeted

chemical species with high selectivity. Undesirable side products could affect neuronal activity by changing the biochemical properties of ion channels or receptors. Second, the precursors should be biocompatible, biochemically stable, and electrochemically active at modest electric fields. The effects of precursors on neuronal activity should be rigorously characterized before designing the electrochemical systems. Finally, counter electrodes need to be improved to minimize the production of active chlorine species or hydrogen gas, which are released from chloride oxidation reaction or hydrogen evolution reaction.

6.2.2 Perspective on Magnetochemical Systems

Magnetic nanotransducers can be functionalized by using different types of thermosensitive polymers or phopholipids. Thermosensitive polymers, including poly(N-isopropylacrylamide), can reversibly change their structure around the lower critical solution temperature, and the transition temperatures of these polymers can be tuned within the physiological temperature range [233]. Similarly, phospholipids, such as dipalmitoylphosphatidylcholine, have shown to undergo phase transitions at a few degrees above normal physiological temperature ($\sim 41°C$). Based on these unique properties, thermosensitive polymers and phospholipids have been utilized as scaffolds for the temperature-sensitive drug release system [234]. Paired with ferrite magnetic nanoparticles, which generate heat under AMFs, these thermosensitive materials can be used to remotely deliver diverse chemical signals to neural circuits [235]. Furthermore, the latency between magnetic field application and the release of chemical signals from MNP-thermosensitive scaffolds can be controlled by tuning the phase transition temperatures of the organic scaffolds and MNP heating efficiency.

Magnetochemical approaches can be further expanded as a means of a multiplexed chemical release strategy. For example, by implementing different types of magnetic nanoparticles, which selectively dissipate heat under specific AMF conditions, magnetothermally multiplexed release of chemical signals may be achieved [236]. Alternatively, multiplexed chemical releases could be feasible by introducing nanotransducers that enable a conversion of magnetic field cues into different types of stimuli,

such as force and electric fields, through magnetomechanical and magnetoelectric effects [237, 238]. For example, anisotropic magnetic nanoparticles can exert torque on cellular membranes when exposed to slow AMFs, and local electric fields can be created upon application of magnetic fields by integrating magnetostrictive and ferroelectric materials [161]. Paired with mechanoresponsive or electroactive chemicals, force or electric fields generated by these types of magnetic nanotransducers could allow for the remote generation or regulation of chemical species. As magnetothermal, magnetomechanical, and magnetoelectric nanotransducers can be effective at specific magnetic field conditions, multiplexed chemical release systems based on these new types of nanotransducers could be designed in the future.

6.2.3 Potential Applications in Neuroscience and Biomedical Research

In this section, we propose potential applications of our electrochemical and magnetochemical strategies for neuroscience and biomedical research, especially focusing on the NO-generating electrochemical platform presented in Chapter 2 and the proton-releasing magnetomechanical system presented in Chapter 4.

NO-releasing electrocatalytic fibers can be adopted to understand NO physiology related to drug addiction. NO is one of a few messenger molecules mediating LTP of inhibitory GABAergic synapses in the VTA, and it has been reported that opioids, such as morphine, could block NO signaling and the LTP of GABA-releasing synapses in brain slices [73]. However, due to the limited tools for NO delivery, it has been difficult to study the effects of opioids on NO physiology in vivo. By delivering opioids through microfluidic channels and electrochemically producing NO in the VTA, our fibers could be useful to study the development of drug addiction in vivo.

Considering that NO is involved in physiological processes in organs beyond the brain, our NO probes can also be applied to other systems, including the gastrointestinal system. Previous studies based on genetic knock-out strategies proposed that NO produced by NO synthase regulates multiple physiological functions in the gastroin-

testinal system, such as motility and vascular function, and pathogenesis of digestive diseases [239]. Unfortunately, this strategy inevitably results in a global change in NO levels, affecting normal NO signaling processes in a non-specific manner. In this regard, our probes, capable of releasing NO in a spatially restricted manner, could be applied to systemically characterize the NO function in physiological and pathological processes within the gastrointestinal system.

The magnetic nanotransducers presented in Chapter 4 can also be employed to discover neural circuits that involve acid-sensing brain regions, such as the nucleus of the solitary tract, the dorsal raphe, the lateral hypothalamus, and the amygdala. It can yield insight into how these neural circuits regulate diverse behaviors in mice, including fear conditioning and respiratory response [176,240]. Our approaches do not require tethering of the animal subjects to the external hardware, such as cannulas and optical fibers, which limits animal behavior during systems neuroscience research and causes foreign-body response. Furthermore, these nanotransducers-based systems can be adopted as model platforms to understand pH-dependent cellular behavior, which is closely related to cancer cell biology and immune function [178, 241].

Bibliography

[1] Harvey Lodish, Arnold Berk, Chris A Kaiser, Chris Kaiser, Monty Krieger, Matthew P Scott, Anthony Bretscher, Hidde Ploegh, and Paul Matsudaira. *Molecular cell biology*. Macmillan, 2008.

[2] James A Frank, Marc-Joseph Antonini, and Polina Anikeeva. Next-generation interfaces for studying neural function. *Nature Biotechnology*, 37(9):1013–1023, 2019.

[3] M Zhuo, S A Small, E R Kandel, and R D Hawkins. Nitric oxide and carbon monoxide produce activity-dependent long-term synaptic enhancement in hippocampus. *Science*, 260(5116):1946–1950, 1993.

[4] Julie Lotharius and Patrik Brundin. Pathogenesis of parkinson's disease: dopamine, vesicles and α-synuclein. *Nature Reviews Neuroscience*, 3(12):932–942, 2002.

[5] S H Snyder. Brain peptides as neurotransmitters. *Science*, 209(4460):976 LP – 983, 8 1980.

[6] Theodore Holmes Bullock, Richard Orkand, and Alan Grinnell. *Introduction to nervous systems*. WH Freeman, 1977.

[7] Frode Fonnum. Glutamate: a neurotransmitter in mammalian brain. *Journal of neurochemistry*, 42(1):1–11, 1984.

[8] D A McCormick. GABA as an inhibitory neurotransmitter in human cerebral cortex. *Journal of Neurophysiology*, 62(5):1018–1027, 11 1989.

[9] Ami Citri and Robert C Malenka. Synaptic Plasticity: Multiple Forms, Functions, and Mechanisms. *Neuropsychopharmacology*, 33(1):18–41, 2008.

[10] Emily P Huang. Synaptic plasticity: A role for nitric oxide in LTP. *Current Biology*, 7(3):R141–R143, 3 1997.

[11] Gennaro Pagano, Flavia Niccolini, and Marios Politis. Imaging in Parkinson's disease. *Clinical Medicine*, 16(4):371 LP – 375, 8 2016.

[12] Pierre Blier and Mostafa El Mansari. Serotonin and beyond: therapeutics for major depression. *Philosophical Transactions of the Royal Society B: Biological Sciences*, 368(1615):20120536, 4 2013.

[13] Alfred G Gilman. Goodman and Gilman's the pharmacological basis of therapeutics. 1985.

[14] Georg C Terstappen, Axel H Meyer, Robert D Bell, and Wandong Zhang. Strategies for delivering therapeutics across the blood–brain barrier. *Nature Reviews Drug Discovery*, 20(5):362–383, 2021.

[15] Joo Yong Sim, Matthew P Haney, Sung Il Park, Jordan G McCall, and Jae-Woong Jeong. Microfluidic neural probes: in vivo tools for advancing neuroscience. *Lab on a Chip*, 17(8):1406–1435, 2017.

[16] Jae-Woong Jeong, Jordan G. McCall, Gunchul Shin, Yihui Zhang, Ream Al-Hasani, Minku Kim, Shuo Li, Joo Yong Sim, Kyung-In Jang, Yan Shi, Daniel Y. Hong, Yuhao Liu, Gavin P. Schmitz, Li Xia, Zhubin He, Paul Gamble, Wilson Z. Ray, Yonggang Huang, Michael R. Bruchas, and John A. Rogers. Wireless Optofluidic Systems for Programmable In Vivo Pharmacology and Optogenetics. *Cell*, 162(3):662–674, 2015.

[17] Andres Canales, Xiaoting Jia, Ulrich P Froriep, Ryan A Koppes, Christina M Tringides, Jennifer Selvidge, Chi Lu, Chong Hou, Lei Wei, Yoel Fink, and Polina Anikeeva. Multifunctional fibers for simultaneous optical, electrical and chemical interrogation of neural circuits in vivo. *Nature Biotechnology*, 33:277, 1 2015.

[18] Jeffrey S Kroin, Amjad Ali, Michelle York, and Richard D Penn. The distribution of medication along the spinal canal after chronic intrathecal administration. *Neurosurgery*, 33(2):226–230, 1993.

[19] Xiaowei Dong. Current Strategies for Brain Drug Delivery. *Theranostics*, 8(6):1481–1493, 2018.

[20] Jimin Park, Kyoungsuk Jin, Atharva Sahasrabudhe, Po-Han Chiang, Joseph H Maalouf, Florian Koehler, Dekel Rosenfeld, Siyuan Rao, Tomo Tanaka, Tural Khudiyev, Zachary J Schiffer, Yoel Fink, Ofer Yizhar, Karthish Manthiram, and Polina Anikeeva. In situ electrochemical generation of nitric oxide for neuronal modulation. *Nature Nanotechnology*, 15(8):690–697, 2020.

[21] Mark T Gladwin, Alan N Schechter, Daniel B Kim-Shapiro, Rakesh P Patel, Neil Hogg, Sruti Shiva, Richard O Cannon III, Malte Kelm, David A Wink, Michael Graham Espey, Edward H Oldfield, Ryszard M Pluta, Bruce A Freeman, Jack R Lancaster Jr, Martin Feelisch, and Jon O Lundberg. The emerging biology of the nitrite anion. *Nature Chemical Biology*, 1:308, 11 2005.

[22] Jon O. Lundberg, Eddie Weitzberg, and Mark T. Gladwin. The nitrate-nitrite-nitric oxide pathway in physiology and therapeutics. *Nature Reviews Drug Discovery*, 7(2):156–167, 2008.

[23] Kenyatta Cosby, Kristine S Partovi, Jack H Crawford, Rakesh P Patel, Christopher D Reiter, Sabrina Martyr, Benjamin K Yang, Myron A Waclawiw, Gloria Zalos, Xiuli Xu, Kris T Huang, Howard Shields, Daniel B Kim-Shapiro, Alan N Schechter, Richard O Cannon III, and Mark T Gladwin. Nitrite reduction to nitric oxide by deoxyhemoglobin vasodilates the human circulation. *Nature Medicine*, 9:1498, 11 2003.

[24] Hyekyoung Choi, Jae-Hyeon Ko, Yong-Hyun Kim, and Sohee Jeong. Steric-Hindrance-Driven Shape Transition in PbS Quantum Dots: Understanding Size-Dependent Stability. *Journal of the American Chemical Society*, 135(14):5278–5281, 4 2013.

[25] Louis J Ignarro. Nitric Oxide: A Unique Endogenous Signaling Molecule in Vascular Biology (Nobel Lecture). *Angewandte Chemie International Edition*, 38(13-14):1882–1892, 7 1999.

[26] R M J Palmer, A G Ferrige, and S Moncada. Nitric oxide release accounts for the biological activity of endothelium-derived relaxing factor. *Nature*, 327:524, 6 1987.

[27] S Moncada and E A Higgs. The discovery of nitric oxide and its role in vascular biology. *British Journal of Pharmacology*, 147(S1):S193–S201, 1 2006.

[28] Takashi Yoshida, Ryuji Inoue, Takashi Morii, Nobuaki Takahashi, Shinichiro Yamamoto, Yuji Hara, Makoto Tominaga, Shunichi Shimizu, Yoji Sato, and Yasuo Mori. Nitric oxide activates TRP channels by cysteine S-nitrosylation. *Nature Chemical Biology*, 2:596, 9 2006.

[29] Jonathan S Stamler. Redox signaling: Nitrosylation and related target interactions of nitric oxide. *Cell*, 78(6):931–936, 1994.

[30] Douglas T Hess, Akio Matsumoto, Sung-Oog Kim, Harvey E Marshall, and Jonathan S Stamler. Protein S-nitrosylation: purview and parameters. *Nature Reviews Molecular Cell Biology*, 6:150, 2 2005.

[31] J S Stamler, D I Simon, J A Osborne, M E Mullins, O Jaraki, T Michel, D J Singel, and J Loscalzo. S-nitrosylation of proteins with nitric oxide: synthesis and characterization of biologically active compounds. *Proceedings of the National Academy of Sciences*, 89(1):444 LP – 448, 1 1992.

[32] Samie R Jaffrey, Hediye Erdjument-Bromage, Christopher D Ferris, Paul Tempst, and Solomon H Snyder. Protein S-nitrosylation: a physiological signal for neuronal nitric oxide. *Nature Cell Biology*, 3:193, 1 2001.

[33] Sara Goldstein and Gidon Czapski. Kinetics of Nitric Oxide Autoxidation in Aqueous Solution in the Absence and Presence of Various Reductants. The Nature of the Oxidizing Intermediates. *Journal of the American Chemical Society*, 117(49):12078–12084, 1995.

[34] Sara Goldstein and Gidon Czapski. Mechanism of the Nitrosation of Thiols and Amines by Oxygenated •NO Solutions: the Nature of the Nitrosating Intermediates. *Journal of the American Chemical Society*, 118(14):3419–3425, 1 1996.

[35] Victor Rosca, Matteo Duca, Matheus T de Groot, and Marc T M Koper. Nitrogen Cycle Electrocatalysis. *Chemical Reviews*, 109(6):2209–2244, 6 2009.

[36] G E Dima, A C A de Vooys, and M T M Koper. Electrocatalytic reduction of nitrate at low concentration on coinage and transition-metal electrodes in acid solutions. *Journal of Electroanalytical Chemistry*, 554-555:15–23, 2003.

[37] Bruce A Averill. Dissimilatory Nitrite and Nitric Oxide Reductases. *Chemical Reviews*, 96(7):2951–2964, 1 1996.

[38] Helmut Beinert, Richard H Holm, and Eckard Münck. Iron-Sulfur Clusters: Nature's Modular, Multipurpose Structures. *Science*, 277(5326):653 LP – 659, 8 1997.

[39] Richard W Strange, Fraser E Dodd, Zelda H L Abraham, J Günter Grossmann, Thomas Brüser, Robert R Eady, Barry E Smith, and S Samar Hasnain. The substrate-binding site in Cu nitrite reductase and its similarity to Zn carbonic anhydrase. *Nature Structural Biology*, 2:287, 4 1995.

[40] Seongjun Park, Yuanyuan Guo, Xiaoting Jia, Han Kyoung Choe, Benjamin Grena, Jeewoo Kang, Jiyeon Park, Chi Lu, Andres Canales, Ritchie Chen, Yeong Shin Yim, Gloria B Choi, Yoel Fink, and Polina Anikeeva. One-step optogenetics with multifunctional flexible polymer fibers. *Nature Neuroscience*, 20:612, 2 2017.

[41] D S Bredt and S H Snyder. NITRIC OXIDE: A Physiologic Messenger Molecule. *Annual Review of Biochemistry*, 63(1):175–195, 6 1994.

[42] Asif K. Mustafa, Moataz M. Gadalla, and Solomon H. Snyder. Signaling by gasotransmitters. *Science Signaling*, 2(68), 2009.

[43] Vittorio Calabrese, Cesare Mancuso, Menotti Calvani, Enrico Rizzarelli, D Allan Butterfield, and Anna Maria Giuffrida Stella. Nitric oxide in the central nervous system: neuroprotection versus neurotoxicity. *Nature Reviews Neuroscience*, 8:766, 10 2007.

[44] Z Huang, P L Huang, N Panahian, T Dalkara, M C Fishman, and M A Moskowitz. Effects of cerebral ischemia in mice deficient in neuronal nitric oxide synthase. *Science*, 265(5180):1883 LP – 1885, 9 1994.

[45] Victor W T Liu and Paul L Huang. Cardiovascular roles of nitric oxide: A review of insights from nitric oxide synthase gene disrupted mice†. *Cardiovascular Research*, 77(1):19–29, 1 2008.

[46] Tazuka Yoshida, Volker Limmroth, Katsumi Irikura, and Michael A Moskowitz. The NOS Inhibitor, 7-Nitroindazole, Decreases Focal Infarct Volume but Not the Response to Topical Acetylcholine in Pial Vessels. *Journal of Cerebral Blood Flow & Metabolism*, 14(6):924–929, 11 1994.

[47] Peng George Wang, Ming Xian, Xiaoping Tang, Xuejun Wu, Zhong Wen, Tingwei Cai, and Adam J Janczuk. Nitric Oxide Donors: Chemical Activities and Biological Applications. *Chemical Reviews*, 102(4):1091–1134, 4 2002.

[48] Michele C Jen, María C Serrano, Robert van Lith, and Guillermo A Ameer. Polymer-Based Nitric Oxide Therapies: Recent Insights for Biomedical Applications. *Advanced Functional Materials*, 22(2):239–260, 1 2012.

[49] Hui Jing Xiang, Min Guo, and Jin Gang Liu. Transition-Metal Nitrosyls for Photocontrolled Nitric Oxide Delivery. *European Journal of Inorganic Chemistry*, 2017(12):1586–1595, 2017.

[50] M Feelisch. The use of nitric oxide donors in pharmacological studies. *Naunyn-Schmiedeberg's Archives of Pharmacology*, 358(1):113–122, 1998.

[51] M R Miller and I L Megson. Recent developments in nitric oxide donor drugs. *British Journal of Pharmacology*, 151(3):305–321, 6 2007.

[52] Effie Y Zhou, Hailey J Knox, Christopher J Reinhardt, Gina Partipilo, Mark J Nilges, and Jefferson Chan. Near-Infrared Photoactivatable Nitric Oxide Donors with Integrated Photoacoustic Monitoring. *Journal of the American Chemical Society*, 140(37):11686–11697, 9 2018.

[53] Dakota J Suchyta and Mark H Schoenfisch. Controlled Release of Nitric Oxide from Liposomes. *ACS Biomaterials Science & Engineering*, 3(9):2136–2143, 9 2017.

[54] Jörg Simon and Martin G. Klotz. Diversity and evolution of bioenergetic systems involved in microbial nitrogen compound transformations. *Biochimica et Biophysica Acta - Bioenergetics*, 1827(2):114–135, 2013.

[55] Oliver Einsle, Albrecht Messerschmidt, Petra Stach, Gleb P. Bourenkov, Hans D. Bartunik, Robert Huber, and Peter M.H. Kroneck. Structure of cytochrome c nitrite reductase. *Nature*, 400(6743):476–480, 1999.

[56] Elitza I. Tocheva, Federico I. Rosell, A. Grant Mauk, and Michael E.P. Murphy. Side-On Copper-Nitrosyl Coordination by Nitrite Reductase. *Science*, 304(5672):867–870, 2004.

[57] Victor Rosca, Matteo Duca, Matheus T. de Groot, and Marc T. M. Koper. ChemInform Abstract: Nitrogen Cycle Electrocatalysis. *ChemInform*, 40(36):2209–2244, 2009.

[58] Jin Joo, Hyon Bin Na, Taekyung Yu, Jung Ho Yu, Young Woon Kim, Fanxin Wu, Jin Z. Zhang, and Taeghwan Hyeon. Generalized and facile synthesis of semiconducting metal sulfide nanocrystals. *Journal of the American Chemical Society*, 125(36):11100–11105, 2003.

[59] R. Rao Gadde and Stanley Bruckenstein. The electroduction of nitrite in 0.1 M HClO4 at platinum. *Journal of Electroanalytical Chemistry*, 50(2):163–174, 1974.

[60] Westinghouse Savannah, River Company, and Savannah River. Electrochemical reduction of nitrates and nitrites in alkaline nuclear waste solutions. *Journal of Applied Electrochemistry*, 26:1–9, 1996.

[61] Joseph Jordan Allen J. Bard Roger Parsons. *Standard Potentials in Aqueous Solution*. 1985.

[62] Hirotatsu Kojima, Yasuteru Urano, Kazuya Kikuchi, Tsunehiko Higuchi, Yasunobu Hirata, and Tetsuo Nagano. Fluorescent Indicators for Imaging Nitric Oxide Production. *Angewandte Chemie International Edition*, 38(21):3209–3212, 11 1999.

[63] Mirjam Eberhardt, Maria Dux, Barbara Namer, Jan Miljkovic, Nada Cordasic, Christine Will, Tatjana I. Kichko, Jeanne De La Roche, Michael Fischer, Sebastián A. Suárez, Damian Bikiel, Karola Dorsch, Andreas Leffler, Alexandru Babes, Angelika Lampert, Jochen K. Lennerz, Johannes Jacobi, Marcelo A. Martí, Fabio Doctorovich, Edward D. Högestätt, Peter M. Zygmunt, Ivana Ivanovic-Burmazovic, Karl Messlinger, Peter Reeh, and Milos R. Filipovic. H2S and NO cooperatively regulate vascular tone by activating a neuroendocrine HNO-TRPA1-CGRP signalling pathway. *Nature Communications*, 5, 2014.

[64] Douglas D Thomas, Xiaoping Liu, Stephen P Kantrow, and Jack R Lancaster. The biological lifetime of nitric oxide: Implications for the perivascular dynamics of NO and O₂. *Proceedings of the National Academy of Sciences*, 98(1):355 LP – 360, 1 2001.

[65] Takashi Miyamoto, Adrienne E Dubin, Matt J Petrus, and Ardem Patapoutian. TRPV1 and TRPA1 Mediate Peripheral Nitric Oxide-Induced Nociception in Mice. *PLOS ONE*, 4(10):e7596, 10 2009.

[66] Kenneth J Valenzano, Elfrida R Grant, Gang Wu, Mohamed Hachicha, Lori Schmid, Laykea Tafesse, Qun Sun, Yakov Rotshteyn, Joseph Francis, James Limberis, Shiazah Malik, Edward R Whittemore, and Dianne Hodges. N-(4-Tertiarybutylphenyl)-4-(3-chloropyridin-2-yl)tetrahydropyrazine -1(2H)-carbox-amide (BCTC), a Novel, Orally Effective Vanilloid Receptor 1 Antagonist with Analgesic Properties: I. In Vitro Characterization . *Journal of Pharmacology and Experimental Therapeutics*, 306(1):377 LP – 386, 7 2003.

[67] Carlos Hermenegildo, Carmina Montoliu, Marta Llansola, María-Dolores Muñoz, José-María Gaztelu, María-Dolores Miñana, and Vicente Felipo. Chronic hyperammonemia impairs the glutamate–nitric oxide–cyclic GMP pathway in cerebellar neurons in culture and in the rat in vivo. *European Journal of Neuroscience*, 10(10):3201–3209, 10 1998.

[68] Neil Hardingham, James Dachtler, and Kevin Fox. The role of nitric oxide in pre-synaptic plasticity and homeostasis , 2013.

[69] Dimiter Stoychev, Achilleas Papoutsis, Alexandra Kelaidopoulou, Georgios Kokkinidis, and Alexander Milchev. Electrodeposition of platinum on metallic and nonmetallic substrates - Selection of experimental conditions. *Materials Chemistry and Physics*, 72(3):360–365, 2001.

[70] Stephan Lammel, Byung Kook Lim, Chen Ran, Kee Wui Huang, Michael J Betley, Kay M Tye, Karl Deisseroth, and Robert C Malenka. Input-specific control of reward and aversion in the ventral tegmental area. *Nature*, 491:212, 10 2012.

[71] Ritchie Chen, Gabriela Romero, Michael G Christiansen, Alan Mohr, and Polina Anikeeva. Wireless magnetothermal deep brain stimulation. *Science*, page 1261821, 3 2015.

[72] Lisa A. Gunaydin, Logan Grosenick, Joel C. Finkelstein, Isaac V. Kauvar, Lief E. Fenno, Avishek Adhikari, Stephan Lammel, Julie J. Mirzabekov, Raag D. Airan, Kelly A. Zalocusky, Kay M. Tye, Polina Anikeeva, Robert C. Malenka, and Karl Deisseroth. Natural Neural Projection Dynamics Underlying Social Behavior. *Cell*, 157(7):1535–1551, 2014.

[73] Fereshteh S Nugent, Esther C Penick, and Julie A Kauer. Opioids block long-term potentiation of inhibitory synapses. *Nature*, 446:1086, 4 2007.

[74] M M Iravani, K Kashefi, P Mander, S Rose, and P Jenner. Involvement of inducible nitric oxide synthase in inflammation-induced dopaminergic neurodegeneration. *Neuroscience*, 110(1):49–58, 2002.

[75] S M Sagar, F R Sharp, and T Curran. Expression of c-fos protein in brain: metabolic mapping at the cellular level. *Science*, 240(4857):1328 LP – 1331, 6 1988.

[76] Hiromu Monai, Masamichi Ohkura, Mika Tanaka, Yuki Oe, Ayumu Konno, Hirokazu Hirai, Katsuhiko Mikoshiba, Shigeyoshi Itohara, Junichi Nakai, Youichi Iwai, and Hajime Hirase. Calcium imaging reveals glial involvement in transcranial direct current stimulation-induced plasticity in mouse brain. *Nature Communications*, 7:11100, 3 2016.

[77] R F Furchgott and D Jothianandan. Endothelium-Dependent and -Independent Vasodilation Involving Cyclic GMP: Relaxation Induced by Nitric Oxide, Carbon Monoxide and Light. *Journal of Vascular Research*, 28(1-3):52–61, 1991.

[78] Jimin Park, Joy S Zeng, Atharva Sahasrabudhe, Kyoungsuk Jin, Yoel Fink, Karthish Manthiram, and Polina Anikeeva. Electrochemical Modulation of Carbon Monoxide-Mediated Cell Signaling. *Angewandte Chemie International Edition*, 60(37):20325–20330, 9 2021.

[79] Rern Jern Lim, Mingshi Xie, Mahasin Alam Sk, Jong-Min Lee, Adrian Fisher, Xin Wang, and Kok Hwa Lim. A review on the electrochemical reduction of CO2 in fuel cells, metal electrodes and molecular catalysts. *Catalysis Today*, 233:169–180, 2014.

[80] Stephanie Nitopi, Erlend Bertheussen, Soren B Scott, Xinyan Liu, Albert K Engstfeld, Sebastian Horch, Brian Seger, Ifan E L Stephens, Karen Chan, Christopher Hahn, Jens K Nørskov, Thomas F Jaramillo, and Ib Chorkendorff. Progress and Perspectives of Electrochemical CO2 Reduction on Copper in Aqueous Electrolyte. *Chemical Reviews*, 119(12):7610–7672, 6 2019.

[81] Bijandra Kumar, Joseph P Brian, Veerendra Atla, Sudesh Kumari, Kari A Bertram, Robert T White, and Joshua M Spurgeon. New trends in the development of heterogeneous catalysts for electrochemical CO2 reduction. *Catalysis Today*, 270:19–30, 2016.

[82] A Verma, D J Hirsch, C E Glatt, G V Ronnett, and S H Snyder. Carbon monoxide: a putative neural messenger. *Science*, 259(5093):381–384, 1993.

[83] Roberto Motterlini and Leo E Otterbein. The therapeutic potential of carbon monoxide. *Nature Reviews Drug Discovery*, 9:728, 9 2010.

[84] Tatsuya Ingi, Julia Cheng, and Gabriele V Ronnett. Carbon Monoxide: An Endogenous Modulator of the Nitric Oxide–Cyclic GMP Signaling System. *Neuron*, 16(4):835–842, 1996.

[85] Carlos C Romão, Walter A Blättler, João D Seixas, and Gonçalo J L Bernardes. Developing drug molecules for therapy with carbon monoxide. *Chem. Soc. Rev.*, 41(9):3571–3583, 2012.

[86] Leo E Otterbein, Fritz H Bach, Jawed Alam, Miguel Soares, Hong Tao Lu, Mark Wysk, Roger J Davis, Richard A Flavell, and Augustine M K Choi. Carbon monoxide has anti-inflammatory effects involving the mitogen-activated protein kinase pathway. *Nature Medicine*, 6(4):422–428, 2000.

[87] Elizabeth N Allred, Eugene R Bleecker, Bernard R Chaitman, Thomas E Dahms, Sidney O Gottlieb, Jack D Hackney, Marcello Pagano, Ronald H Selvester, Sandra M Walden, and Jane Warren. Short-Term Effects of Carbon Monoxide Exposure on the Exercise Performance of Subjects with Coronary Artery Disease. *New England Journal of Medicine*, 321(21):1426–1432, 1989.

[88] Jin Meng, Zhaokui Jin, Penghe Zhao, Bin Zhao, Mingjian Fan, and Qianjun He. A multistage assembly/disassembly strategy for tumor-targeted CO delivery. *Science Advances*, 6(20), 2020.

[89] Armin Ernst and Joseph D Zibrak. Carbon Monoxide Poisoning. *New England Journal of Medicine*, 339(22):1603–1608, 1998.

[90] Stefan H Heinemann, Toshinori Hoshi, Matthias Westerhausen, and Alexander Schiller. Carbon monoxide – physiology{,} detection and controlled release. *Chem. Commun.*, 50(28):3644–3660, 2014.

[91] Sandra García-Gallego and Gonçalo J L Bernardes. Carbon-Monoxide-Releasing Molecules for the Delivery of Therapeutic CO In Vivo. *Angewandte Chemie International Edition*, 53(37):9712–9721, 2014.

[92] Roberto Motterlini, James E Clark, Roberta Foresti, Padmini Sarathchandra, Brian E Mann, and Colin J Green. Carbon Monoxide-Releasing Molecules. *Circulation Research*, 90(2):e17–e24, 2002.

[93] James E Clark, Patrick Naughton, Sandra Shurey, Colin J Green, Tony R Johnson, Brian E Mann, Roberta Foresti, and Roberto Motterlini. Cardioprotective Actions by a Water-Soluble Carbon Monoxide–Releasing Molecule. *Circulation Research*, 93(2):e2–e8, 2003.

[94] Roberto Motterlini, Philip Sawle, Sandip Bains, Jehad Hammad, Roger Alberto, Roberta Foresti, and Colin J Green. CORM-A1: a new pharmacologically active carbon monoxide-releasing molecule. *The FASEB Journal*, 19(2):1–24, 2005.

[95] Roberta Foresti, Jehad Hammad, James E Clark, Tony R Johnson, Brian E Mann, Andreas Friebe, Colin J Green, and Roberto Motterlini. Vasoactive properties of CORM-3, a novel water-soluble carbon monoxide-releasing molecule. *British Journal of Pharmacology*, 142(3):453–460, 2004.

[96] Xing Zhang, Zishan Wu, Xiao Zhang, Liewu Li, Yanyan Li, Haomin Xu, Xiaoxiao Li, Xiaolu Yu, Zisheng Zhang, Yongye Liang, and Hailiang Wang. Highly selective and active CO2 reduction electrocatalysts based on cobalt phthalocyanine/carbon nanotube hybrid structures. *Nature Communications*, 8(1):14675, 2017.

[97] Joy S Zeng, Nathan Corbin, Kindle Williams, and Karthish Manthiram. Kinetic Analysis on the Role of Bicarbonate in Carbon Dioxide Electroreduction at Immobilized Cobalt Phthalocyanine. *ACS Catalysis*, 10(7):4326–4336, 4 2020.

[98] Minghui Zhu, Ruquan Ye, Kyoungsuk Jin, Nikifar Lazouski, and Karthish Manthiram. Elucidating the Reactivity and Mechanism of CO2 Electroreduction at Highly Dispersed Cobalt Phthalocyanine. *ACS Energy Letters*, 3(6):1381–1386, 6 2018.

[99] Marco Dunwell, Qi Lu, Jeffrey M Heyes, Jonathan Rosen, Jingguang G Chen, Yushan Yan, Feng Jiao, and Bingjun Xu. The Central Role of Bicarbonate in the Electrochemical Reduction of Carbon Dioxide on Gold. *Journal of the American Chemical Society*, 139(10):3774–3783, 3 2017.

[100] Anna Wuttig, Youngmin Yoon, Jaeyune Ryu, and Yogesh Surendranath. Bicarbonate Is Not a General Acid in Au-Catalyzed CO2 Electroreduction. *Journal of the American Chemical Society*, 139(47):17109–17113, 11 2017.

[101] Tatsuya Ingi, George Chiang, and Gabriele V Ronnett. The Regulation of Heme Turnover and Carbon Monoxide Biosynthesis in Cultured Primary Rat Olfactory Receptor Neurons. *Journal of Neuroscience*, 16(18):5621–5628, 1996.

[102] Randa Zakhary, Kenneth D Poss, Samie R Jaffrey, Christopher D Ferris, Susumu Tonegawa, and Solomon H Snyder. Targeted gene deletion of heme oxygenase 2 reveals neural role for carbon monoxide. *Proceedings of the National Academy of Sciences*, 94(26):14848–14853, 1997.

[103] V G Kharitonov, V S Sharma, R B Pilz, D Magde, and D Koesling. Basis of guanylate cyclase activation by carbon monoxide. *Proceedings of the National Academy of Sciences*, 92(7):2568–2571, 1995.

[104] Scott J Parkinson, Aleksandar Jovanovic, Sofija Jovanovic, Frank Wagner, Andre Terzic, and Scott A Waldman. Regulation of Nitric Oxide-Responsive Recombinant Soluble Guanylyl Cyclase by Calcium. *Biochemistry*, 38(20):6441–6448, 5 1999.

[105] Wolfgang A Buechler, Masaki Nakane, and Ferid Murad. Expression of soluble guanylate cyclase activity requires both enzyme subunits. *Biochemical and Biophysical Research Communications*, 174(1):351–357, 1991.

[106] J P YOU, Q WANG, W ZHANG, I JANSEN-OLESEN, O B PAULSON, N A LASSEN, and L EDVINSSON. Hypercapnic vasodilatation in isolated rat basilar arteries is exerted via low pH and does not involve nitric oxide synthase stimulation or cyclic GMP production. *Acta Physiologica Scandinavica*, 152(4):391–397, 1994.

[107] Antonia Marazioti, Mariarosaria Bucci, Ciro Coletta, Valentina Vellecco, Padmamalini Baskaran, Csaba Szabó, Giuseppe Cirino, Ana Rita Marques, Bruno Guerreiro, Ana M L Gonçalves, João D Seixas, Annie Beuve, Carlos C Romão, and Andreas Papapetropoulos. Inhibition of Nitric Oxide–Stimulated Vasorelaxation by Carbon Monoxide-Releasing Molecules. *Arteriosclerosis, Thrombosis, and Vascular Biology*, 31(11):2570–2576, 2011.

[108] Mayumi Kajimura, Ryo Fukuda, Ryon M Bateman, Takehiro Yamamoto, and Makoto Suematsu. Interactions of Multiple Gas-Transducing Systems: Hallmarks and Uncertainties of CO, NO, and H2S Gas Biology. *Antioxidants & Redox Signaling*, 13(2):157–192, 2010.

[109] Mayumi Kajimura, Masaru Shimoyama, Shingo Tsuyama, Tsuneharu Suzuki, Shunji Kozaki, Shigeo Takenaka, Kazuo Tsubota, Yoshihisa Oguchi, and Makoto Suematsu. Visualization of gaseous monoxide reception by soluble guanylate cyclase in the rat retina. *The FASEB Journal*, 17(3):1–23, 2003.

[110] Christian Thorup, Caroline L Jones, Steven S Gross, Leon C Moore, and Michael S Goligorsky. Carbon monoxide induces vasodilation and nitric oxide release but suppresses endothelial NOS. *American Journal of Physiology-Renal Physiology*, 277(6):F882–F889, 1999.

[111] Giovanni Scapagnini, Velia D'Agata, Vittorio Calabrese, Alessia Pascale, Claudia Colombrita, Daniel Alkon, and Sebastiano Cavallaro. Gene expression profiles of heme oxygenase isoforms in the rat brain. *Brain Research*, 954(1):51–59, 2002.

[112] Claude A Piantadosi, Jing Zhang, Edward D Levin, Rodney J Folz, and Donald E Schmechel. Apoptosis and Delayed Neuronal Damage after Carbon Monoxide Poisoning in the Rat. *Experimental Neurology*, 147(1):103–114, 1997.

[113] Ya-Ping Tang, Yoshiharu Murata, Takashi Nagaya, Yukihiro Noda, Hisao Seo, and Toshitaka Nabeshima. NGFI-B, c-fos, and c-jun mRNA Expression in Mouse Brain after Acute Carbon Monoxide Intoxication. *Journal of Cerebral Blood Flow & Metabolism*, 17(7):771–780, 1997.

[114] K R Gee, K A Brown, W-N.U. Chen, J Bishop-Stewart, D Gray, and I Johnson. Chemical and physiological characterization of fluo-4 Ca2+-indicator dyes. *Cell Calcium*, 27(2):97–106, 2000.

[115] William J Wilkinson and Paul J Kemp. Carbon monoxide: an emerging regulator of ion channels. *The Journal of Physiology*, 589(13):3055–3062, 2011.

[116] C Peers, J P Boyle, J L Scragg, M L Dallas, M M Al-Owais, N T Hettiarachichi, J Elies, E Johnson, N Gamper, and D S Steele. Diverse mechanisms underlying the regulation of ion channels by carbon monoxide. *British Journal of Pharmacology*, 172(6):1546–1556, 2015.

[117] Inja Lim, Simon J Gibbons, Gregory L Lyford, Steven M Miller, Peter R Strege, Michael G Sarr, Suvro Chatterjee, Joseph H Szurszewski, Vijay H Shah, and Gianrico Farrugia. Carbon monoxide activates human intestinal smooth muscle L-type Ca2+ channels through a nitric oxide-dependent mechanism. *American Journal of Physiology-Gastrointestinal and Liver Physiology*, 288(1):G7–G14, 2005.

[118] António F Ambrósio, Ana P Silva, João O Malva, Patrıcio Soares-da Silva, Arsélio P Carvalho, and Caetana M Carvalho. Carbamazepine inhibits L-type Ca2+ channels in cultured rat hippocampal neurons stimulated with glutamate receptor agonists. *Neuropharmacology*, 38(9):1349–1359, 1999.

[119] Shogo Matsuda, Kazuki Harada, Motoki Ito, Mai Takizawa, Devina Wongso, Takashi Tsuboi, and Tetsuya Kitaguchi. Generation of a cGMP Indicator with an Expanded Dynamic Range by Optimization of Amino Acid Linkers between a Fluorescent Protein and PDE5α. *ACS Sensors*, 2(1):46–51, 1 2017.

[120] Jimin Park, Anthony Tabet, Junsang Moon, Po-Han Chiang, Florian Koehler, Atharva Sahasrabudhe, and Polina Anikeeva. Remotely Controlled Proton Generation for Neuromodulation. *Nano Letters*, 20(9):6535–6541, 9 2020.

[121] Kumaresh S Soppimath, Tejraj M Aminabhavi, Anandrao R Kulkarni, and Walter E Rudzinski. Biodegradable polymeric nanoparticles as drug delivery devices. *Journal of Controlled Release*, 70(1):1–20, 2001.

[122] Lisa E Freed, Gordana Vunjak-Novakovic, Robert J Biron, Dana B Eagles, Daniel C Lesnoy, Sandra K Barlow, and Robert Langer. Biodegradable Polymer Scaffolds for Tissue Engineering. *Bio/Technology*, 12:689, 7 1994.

[123] Hirenkumar K Makadia and Steven J Siegel. Poly Lactic-co-Glycolic Acid (PLGA) as Biodegradable Controlled Drug Delivery Carrier, 2011.

[124] Neeraj Kumar, Robert S Langer, and Abraham J Domb. Polyanhydrides: an overview. *Advanced Drug Delivery Reviews*, 54(7):889–910, 2002.

[125] Friederike von Burkersroda, Luise Schedl, and Achim Göpferich. Why degradable polymers undergo surface erosion or bulk erosion. *Biomaterials*, 23(21):4221–4231, 2002.

[126] I Grizzi, H Garreau, S Li, and M Vert. Hydrolytic degradation of devices based on poly(dl-lactic acid) size-dependence. *Biomaterials*, 16(4):305–311, 1995.

[127] C M Agrawal, D Huang, J P Schmitz, and K A Athanasiou. Elevated Temperature Degradation of a 50:50 Copolymer of PLA-PGA. *Tissue Engineering*, 3(4):345–352, 12 1997.

[128] Banu S Zolnik, Pauline E Leary, and Diane J Burgess. Elevated temperature accelerated release testing of PLGA microspheres. *Journal of Controlled Release*, 112(3):293–300, 2006.

[129] P B Rim and K M O'Connor. Kinetics of hydrolysis of poly(α-olefin-co-maleic anhydride). *Journal of Applied Polymer Science*, 32(4):4679–4688, 9 1986.

[130] D C Jiles and D L Atherton. Theory of ferromagnetic hysteresis. *Journal of Magnetism and Magnetic Materials*, 61(1):48–60, 1986.

[131] W Wernsdorfer, E Bonet Orozco, K Hasselbach, A Benoit, B Barbara, N Demoncy, A Loiseau, H Pascard, and D Mailly. Experimental Evidence of the N{\textbackslash}'eel-Brown Model of Magnetization Reversal. *Physical Review Letters*, 78(9):1791–1794, 1997.

[132] Masashi Tachiki. Origin of the Magnetic Anisotropy Energy of Cobalt Ferrite. *Progress of Theoretical Physics*, 23(6):1055–1072, 6 1960.

[133] N A Usov and J M Barandiarán. Magnetic nanoparticles with combined anisotropy. *Journal of Applied Physics*, 112(5):53915, 9 2012.

[134] R Yanes, O Chubykalo-Fesenko, H Kachkachi, D A Garanin, R Evans, and R W Chantrell. Effective anisotropies and energy barriers of magnetic nanoparticles with N{\textbackslash}'eel surface anisotropy. *Physical Review B*, 76(6):64416, 2007.

[135] C Tannous Gieraltowski and J. The Stoner–Wohlfarth model of ferromagnetism. *European Journal of Physics*, 29(3):475, 2008.

[136] J Carrey, B Mehdaoui, and M Respaud. Simple models for dynamic hysteresis loop calculations of magnetic single-domain nanoparticles: Application to magnetic hyperthermia optimization. *Journal of Applied Physics*, 109(8):83921, 4 2011.

[137] William Fuller Brown. Thermal Fluctuations of a Single-Domain Particle. *Physical Review*, 130(5):1677–1686, 6 1963.

[138] Rudolf Hergt Röder, Silvio Dutz, and Michael. Effects of size distribution on hysteresis losses of magnetic nanoparticles for hyperthermia. *Journal of Physics: Condensed Matter*, 20(38):385214, 2008.

[139] Ritchie Chen, Michael G Christiansen, and Polina Anikeeva. Maximizing Hysteretic Losses in Magnetic Ferrite Nanoparticles via Model-Driven Synthesis and Materials Optimization. *ACS Nano*, 7(10):8990–9000, 10 2013.

[140] M L Hans and A M Lowman. Biodegradable nanoparticles for drug delivery and targeting. *Current Opinion in Solid State and Materials Science*, 6(4):319–327, 2002.

[141] David Julian McClements. Nanoemulsions versus microemulsions: terminology, differences, and similarities. *Soft Matter*, 8(6):1719–1729, 2012.

[142] Iosif Daniel Rosca, Fumio Watari, and Motohiro Uo. Microparticle formation and its mechanism in single and double emulsion solvent evaporation. *Journal of Controlled Release*, 99(2):271–280, 2004.

[143] Fong-Yu Cheng, Saprina Ping-Hsien Wang, Chio-Hao Su, Tsung-Liu Tsai, Ping-Ching Wu, Dar-Bin Shieh, Jyh-Horng Chen, Patrick Ching-Ho Hsieh, and Chen-Sheng Yeh. Stabilizer-free poly(lactide-co-glycolide) nanoparticles for multimodal biomedical probes. *Biomaterials*, 29(13):2104–2112, 2008.

[144] J Kim, J.E. Lee, S.H. Lee, J.H. Yu, J.H. Lee, T.G. Park, and T Hyeon. Designed Fabrication of a Multifunctional Polymer Nanomedical Platform for Simultaneous Cancer- Targeted Imaging and Magnetically Guided Drug Delivery. *Advanced Materials*, 20(3):478–483, 2 2008.

[145] MITCHELL CHESLER. Regulation and Modulation of pH in the Brain. *Physiological Reviews*, 83(4):1183–1221, 2003.

[146] Ian F Tannock and Daniela Rotin. Acid pH in Tumors and Its Potential for Therapeutic Exploitation. *Cancer Research*, 49(16):4373–4384, 1989.

[147] Stefanie Kohse, Antje Neubauer, Alexandra Pazidis, Stefan Lochbrunner, and Udo Kragl. Photoswitching of Enzyme Activity by Laser-Induced pH-Jump. *Journal of the American Chemical Society*, 135(25):9407–9411, 6 2013.

[148] Paul Saftig and Judith Klumperman. Lysosome biogenesis and lysosomal membrane proteins: trafficking meets function. *Nature Reviews Molecular Cell Biology*, 10:623, 8 2009.

[149] Zhi-Gang Xiong, Giuseppe Pignataro, Minghua Li, Su-youne Chang, and Roger P Simon. Acid-sensing ion channels (ASICs) as pharmacological targets for neurodegenerative diseases. *Current Opinion in Pharmacology*, 8(1):25–32, 2008.

[150] Olena Yermolaieva, A Soren Leonard, Mikael K Schnizler, Francois M Abboud, and Michael J Welsh. Extracellular acidosis increases neuronal cell calcium by activating acid-sensing ion channel 1a. *Proceedings of the National Academy of Sciences of the United States of America*, 101(17):6752 LP – 6757, 4 2004.

[151] John A Wemmie, Rebecca J Taugher, and Collin J Kreple. Acid-sensing ion channels in pain and disease. *Nature Reviews Neuroscience*, 14:461, 6 2013.

[152] Jayasankar Jasti, Hiroyasu Furukawa, Eric B Gonzales, and Eric Gouaux. Structure of acid-sensing ion channel 1 at 1.9 Åresolution and low pH. *Nature*, 449:316, 2007.

[153] John A Wemmie, Jianguo Chen, Candice C Askwith, Alesia M Hruska-Hageman, Margaret P Price, Brian C Nolan, Patrick G Yoder, Ejvis Lamani, Toshinori Hoshi, John H Freeman, and Michael J Welsh. The Acid-Activated Ion Channel ASIC Contributes to Synaptic Plasticity, Learning, and Memory. *Neuron*, 34(3):463–477, 2002.

[154] Yongmei Chen and Raymond A Swanson. Astrocytes and Brain Injury. *Journal of Cerebral Blood Flow & Metabolism*, 23(2):137–149, 2 2003.

[155] O Kempski, F Staub, M Jansen, F Schödel, and A Baethmann. Glial swelling during extracellular acidosis in vitro. *Stroke*, 19(3):385–392, 3 1988.

[156] Adam E Ziemann, Mikael K Schnizler, Gregory W Albert, Meryl A Severson, Matthew A Howard III, Michael J Welsh, and John A Wemmie. Seizure termination by acidosis depends on ASIC1a. *Nature Neuroscience*, 11(7):816–822, 2008.

[157] Adam E Ziemann, Jason E Allen, Nader S Dahdaleh, Iuliia I Drebot, Matthew W Coryell, Amanda M Wunsch, Cynthia M Lynch, Frank M Faraci, Matthew A Howard, Michael J Welsh, and John A Wemmie. The Amygdala Is a

Chemosensor that Detects Carbon Dioxide and Acidosis to Elicit Fear Behavior. *Cell*, 139(5):1012–1021, 2009.

[158] Shinya Ugawa, Takashi Ueda, Yusuke Ishida, Makoto Nishigaki, Yasuhiro Shibata, and Shoichi Shimada. Amiloride-blockable acid-sensing ion channels are leading acid sensors expressed in human nociceptors. *The Journal of Clinical Investigation*, 110(8):1185–1190, 2002.

[159] Yingxin Deng, Takeo Miyake, Scott Keene, Erik E Josberger, and Marco Rolandi. Proton mediated control of biochemical reactions with bioelectronic pH modulation. *Scientific Reports*, 6(1):24080, 2016.

[160] Erik E Josberger, Pegah Hassanzadeh, Yingxin Deng, Joel Sohn, Michael J Rego, Chris T Amemiya, and Marco Rolandi. Proton conductivity in ampullae of Lorenzini jelly. *Science Advances*, 2(5), 2016.

[161] Ritchie Chen, Andres Canales, and Polina Anikeeva. Neural recording and modulation technologies. *Nature Reviews Materials*, 2:16093, 1 2017.

[162] Rahul Munshi, Shahnaz M Qadri, Qian Zhang, Idoia Castellanos Rubio, Pablo del Pino, and Arnd Pralle. Magnetothermal genetic deep brain stimulation of motor behaviors in awake, freely moving mice. *eLife*, 6:e27069, 8 2017.

[163] Sarah A Stanley, Jennifer E Gagner, Shadi Damanpour, Mitsukuni Yoshida, Jonathan S Dordick, and Jeffrey M Friedman. Radio-Wave Heating of Iron Oxide Nanoparticles Can Regulate Plasma Glucose in Mice. *Science*, 336(6081):604 LP – 608, 5 2012.

[164] Dekel Rosenfeld, Alexander W Senko, Junsang Moon, Isabel Yick, Georgios Varnavides, Danijela Gregureć, Florian Koehler, Po-Han Chiang, Michael G Christiansen, Lisa Y Maeng, Alik S Widge, and Polina Anikeeva. Transgene-free remote magnetothermal regulation of adrenal hormones. *Science Advances*, 6(15), 2020.

[165] Juyao Dong and Jeffrey I Zink. Taking the Temperature of the Interiors of Magnetically Heated Nanoparticles. *ACS Nano*, 8(5):5199–5207, 5 2014.

[166] Abraham J Domb and Raphael Nudelman. In vivo and in vitro elimination of aliphatic polyanhydrides. *Biomaterials*, 16(4):319–323, 1995.

[167] Z X Meng, Y S Wang, C Ma, W Zheng, L Li, and Y F Zheng. Electrospinning of PLGA/gelatin randomly-oriented and aligned nanofibers as potential scaffold in tissue engineering. *Materials Science and Engineering: C*, 30(8):1204–1210, 2010.

[168] Rudolf Hergt and Silvio Dutz. Magnetic particle hyperthermia—biophysical limitations of a visionary tumour therapy. *Journal of Magnetism and Magnetic Materials*, 311(1):187–192, 2007.

[169] Gabriela Romero, Michael G Christiansen, Ligia Stocche Barbosa, Francisco Garcia, and Polina Anikeeva. Localized Excitation of Neural Activity via Rapid Magnetothermal Drug Release. *Advanced Functional Materials*, 26(35):6471–6478, 9 2016.

[170] K J Buckler and R D Vaughan-Jones. Application of a new pH-sensitive fluoroprobe (carboxy-SNARF-1) for intracellular pH measurement in small, isolated cells. *Pflügers Archiv*, 417(2):234–239, 1990.

[171] Anne Baron, Rainer Waldmann, and Michel Lazdunski. ASIC-like, proton-activated currents in rat hippocampal neurons. *The Journal of Physiology*, 539(2):485–494, 2002.

[172] Zhi-Gang Xiong, Xiao-Man Zhu, Xiang-Ping Chu, Manabu Minami, Jessica Hey, Wen-Li Wei, John F MacDonald, John A Wemmie, Margaret P Price, Michael J Welsh, and Roger P Simon. Neuroprotection in Ischemia: Blocking Calcium-Permeable Acid-Sensing Ion Channels. *Cell*, 118(6):687–698, 2004.

[173] Jennifer Kim and Barry Connors. High temperatures alter physiological properties of pyramidal cells and inhibitory interneurons in hippocampus. *Frontiers in Cellular Neuroscience*, 6:27, 2012.

[174] John A Wemmie, Candice C Askwith, Ejvis Lamani, Martin D Cassell, John H Freeman, and Michael J Welsh. Acid-Sensing Ion Channel 1 Is Localized in Brain Regions with High Synaptic Density and Contributes to Fear Conditioning. *The Journal of Neuroscience*, 23(13):5496 LP – 5502, 7 2003.

[175] Patrice G. Guyenet and Douglas A. Bayliss. Neural Control of Breathing and CO2 Homeostasis. *Neuron*, 87(5):946–961, 2015.

[176] Natasha N Kumar, Ana Velic, Jorge Soliz, Yingtang Shi, Keyong Li, Sheng Wang, Janelle L Weaver, Josh Sen, Stephen B G Abbott, Roman M Lazarenko, Marie-Gabrielle Ludwig, Edward Perez-Reyes, Nilufar Mohebbi, Carla Bettoni, Max Gassmann, Thomas Suply, Klaus Seuwen, Patrice G Guyenet, Carsten A Wagner, and Douglas A Bayliss. Regulation of breathing by CO₂ requires the proton-activated receptor GPR4 in retrotrapezoid nucleus neurons. *Science*, 348(6240):1255 LP – 1260, 6 2015.

[177] Mateusz L Donten, Shabir Hassan, Alexander Popp, Jonathan Halter, Karin Hauser, and Peter Hamm. pH-Jump Induced Leucine Zipper Folding beyond the Diffusion Limit. *The Journal of Physical Chemistry B*, 119(4):1425–1432, 1 2015.

[178] Anne Lardner. The effects of extracellular pH on immune function. *Journal of Leukocyte Biology*, 69(4):522–530, 2001.

[179] Jimin Park, Florian Koehler, Georgios Varnavides, Marc-Joseph Antonini, and Polina Anikeeva. Influence of Magnetic Fields on Electrochemical Reactions of Redox Cofactor Solutions. *Angewandte Chemie International Edition*, 60:18295–18302, 2021.

[180] Ulrich E Steiner and Thomas Ulrich. Magnetic field effects in chemical kinetics and related phenomena. *Chemical Reviews*, 89(1):51–147, 1989.

[181] Nicholas J Turro and Bernhard Kraeutler. Magnetic field and magnetic isotope effects in organic photochemical reactions. A novel probe of reaction mechanisms and a method for enrichment of magnetic isotopes. *Accounts of Chemical Research*, 13(10):369–377, 1980.

[182] Eric Hontz, Wendi Chang, Daniel N Congreve, Vladimir Bulović, Marc A Baldo, and Troy Van Voorhis. The Role of Electron–Hole Separation in Thermally Activated Delayed Fluorescence in Donor–Acceptor Blends. *The Journal of Physical Chemistry C*, 119(45):25591–25597, 11 2015.

[183] P J Hore and Henrik Mouritsen. The Radical-Pair Mechanism of Magnetoreception. *Annual Review of Biophysics*, 45(1):299–344, 7 2016.

[184] Daniel R Kattnig, Emrys W Evans, Victoire Déjean, Charlotte A Dodson, Mark I Wallace, Stuart R Mackenzie, Christiane R Timmel, and P J Hore. Chemical amplification of magnetic field effects relevant to avian magnetoreception. *Nature Chemistry*, 8:384, 2 2016.

[185] Masaaki Murakami, Kiminori Maeda, and Tatsuo Arai. Dynamics of Intramolecular Electron Transfer Reaction of FAD Studied by Magnetic Field Effects on Transient Absorption Spectra. *The Journal of Physical Chemistry A*, 109(26):5793–5800, 7 2005.

[186] Yoshio Sakaguchi, Hisaharu Hayashi, and Saburo Nagakura. Classification of the External Magnetic Field Effects on the Photodecomposition Reaction of Dibenzoyl Peroxide. *Bulletin of the Chemical Society of Japan*, 53(1):39–42, 1 1980.

[187] Christopher T Rodgers and P J Hore. Chemical magnetoreception in birds: The radical pair mechanism. *Proceedings of the National Academy of Sciences*, 106(2):353–360, 2009.

[188] Kiminori Maeda, Kevin B Henbest, Filippo Cintolesi, Ilya Kuprov, Christopher T Rodgers, Paul A Liddell, Devens Gust, Christiane R Timmel, and P J Hore. Chemical compass model of avian magnetoreception. *Nature*, 453:387, 4 2008.

[189] Kiminori Maeda, Alexander J Robinson, Kevin B Henbest, Hannah J Hogben, Till Biskup, Margaret Ahmad, Erik Schleicher, Stefan Weber, Christiane R

Timmel, and P J Hore. Magnetically sensitive light-induced reactions in cryptochrome are consistent with its proposed role as a magnetoreceptor. *Proceedings of the National Academy of Sciences*, 109(13):4774 LP – 4779, 3 2012.

[190] Alpha A. Lee, Jason C.S. Lau, Hannah J. Hogben, Till Biskup, Daniel R. Kattnig, and P.J. Hore. Alternative radical pairs for cryptochrome-based magnetoreception. *Journal of The Royal Society Interface*, 11(95):20131063, 6 2014.

[191] Jeffrey Green and Mark S Paget. Bacterial redox sensors. *Nature Reviews Microbiology*, 2(12):954–966, 2004.

[192] Judith P Klinman and David Mu. QUINOENZYMES IN BIOLOGY. *Annual Review of Biochemistry*, 63(1):299–344, 1994.

[193] Christopher Walsh. Flavin coenzymes: at the crossroads of biological redox chemistry. *Accounts of Chemical Research*, 13(5):148–155, 5 1980.

[194] W J H van Berkel, N M Kamerbeek, and M W Fraaije. Flavoprotein monooxygenases, a diverse class of oxidative biocatalysts. *Journal of Biotechnology*, 124(4):670–689, 2006.

[195] Yaming Yu, Björn Heidel, Tamara Lourdes Parapugna, Sabine Wenderhold-Reeb, Bo Song, Holger Schönherr, Martin Grininger, and Gilbert Nöll. The Flavoprotein Dodecin as a Redox Probe for Electron Transfer through DNA. *Angewandte Chemie International Edition*, 52(18):4950–4953, 2013.

[196] Akihiro Orita, Michael G Verde, Masanori Sakai, and Ying Shirley Meng. A biomimetic redox flow battery based on flavin mononucleotide. *Nature Communications*, 7(1):13230, 2016.

[197] James A Cracknell, Kylie A Vincent, and Fraser A Armstrong. Enzymes as Working or Inspirational Electrocatalysts for Fuel Cells and Electrolysis. *Chemical Reviews*, 108(7):2439–2461, 7 2008.

[198] Eugenii Katz, Oleg Lioubashevski, and Itamar Willner. Magnetic Field Effects on Bioelectrocatalytic Reactions of Surface-Confined Enzyme Systems: Enhanced Performance of Biofuel Cells. *Journal of the American Chemical Society*, 127(11):3979–3988, 3 2005.

[199] Serena L J Tan, Jia Min Kan, and Richard D Webster. Differences in Proton-Coupled Electron-Transfer Reactions of Flavin Mononucleotide (FMN) and Flavin Adenine Dinucleotide (FAD) between Buffered and Unbuffered Aqueous Solutions. *The Journal of Physical Chemistry B*, 117(44):13755–13766, 11 2013.

[200] Serena L J Tan, Maria L Novianti, and Richard D Webster. Effects of Low to Intermediate Water Concentrations on Proton-Coupled Electron Transfer (PCET) Reactions of Flavins in Aprotic Solvents and a Comparison with

the PCET Reactions of Quinones. *The Journal of Physical Chemistry B*, 119(44):14053–14064, 11 2015.

[201] Yanlan Hui, Elaine Lay Khim Chng, Cheryl Yi Lin Chng, Hwee Ling Poh, and Richard D Webster. Hydrogen-Bonding Interactions between Water and the One- and Two-Electron-Reduced Forms of Vitamin K1: Applying Quinone Electrochemistry To Determine the Moisture Content of Non-Aqueous Solvents. *Journal of the American Chemical Society*, 131(4):1523–1534, 2 2009.

[202] Allen J Bard and Larry R Faulkner. Fundamentals and applications. *Electrochemical Methods*, 2(482):580–632, 2001.

[203] Amélie Forget, Benoît Limoges, and Véronique Balland. Efficient Chemisorption of Organophosphorous Redox Probes on Indium Tin Oxide Surfaces under Mild Conditions. *Langmuir*, 31(6):1931–1940, 2 2015.

[204] D Sen, K M Isaac, N Leventis, and I Fritsch. Investigation of transient redox electrochemical MHD using numerical simulations. *International Journal of Heat and Mass Transfer*, 54(25):5368–5378, 2011.

[205] Shizhi Qian and Haim H Bau. Magnetohydrodynamic flow of RedOx electrolyte. *Physics of Fluids*, 17(6):67105, 2005.

[206] Hussameddine Kabbani, Aihua Wang, Xiaobing Luo, and Shizhi Qian. Modeling RedOx-based magnetohydrodynamics in three-dimensional microfluidic channels. *Physics of Fluids*, 19(8):83604, 2007.

[207] Lorena M A Monzon and J M D Coey. Magnetic fields in electrochemistry: The Lorentz force. A mini-review. *Electrochemistry Communications*, 42:38–41, 2014.

[208] A Bund, S Koehler, H H Kuehnlein, and W Plieth. Magnetic field effects in electrochemical reactions. *Electrochimica Acta*, 49(1):147–152, 2003.

[209] Jakub Adam Koza, Sascha Mühlenhoff, Piotr Żabiński, Petr A Nikrityuk, Kerstin Eckert, Margitta Uhlemann, Annett Gebert, Tom Weier, Ludwig Schultz, and Stefan Odenbach. Hydrogen evolution under the influence of a magnetic field. *Electrochimica Acta*, 56(6):2665–2675, 2011.

[210] Kristina Tschulik, Jakub Adam Koza, Margitta Uhlemann, Annett Gebert, and Ludwig Schultz. Magnetoelectrochemical Surface Structuring: Electrodeposition of Structured Metallic Layers in Magnetic Gradient Fields. *ECS Transactions*, 25(41):149–155, 2019.

[211] Jakub Koza, Margitta Uhlemann, Annett Gebert, and Ludwig Schultz. The effect of magnetic fields on the electrodeposition of iron. *Journal of Solid State Electrochemistry*, 12(2):181–192, 2008.

[212] Jakub Adam Koza, Sascha Mühlenhoff, Margitta Uhlemann, Kerstin Eckert, Annett Gebert, and Ludwig Schultz. Desorption of hydrogen from an electrode surface under influence of an external magnetic field – In-situ microscopic observations. *Electrochemistry Communications*, 11(2):425–429, 2009.

[213] Haiping Pan, Yan Shen, Jiashun Duan, Kai Lu, and Bin Hu. Spin-dependent deprotonation induced giant magnetocurrent in electrochemical cells. *Physical Chemistry Chemical Physics*, 18(15):9897–9901, 2016.

[214] Thomas C Player and P J Hore. Source of magnetic field effects on the electrocatalytic reduction of CO2. *The Journal of Chemical Physics*, 153(8):84303, 2020.

[215] Serena L J Tan and Richard D Webster. Electrochemically Induced Chemically Reversible Proton-Coupled Electron Transfer Reactions of Riboflavin (Vitamin B2). *Journal of the American Chemical Society*, 134(13):5954–5964, 4 2012.

[216] L Wilmer Anderson, Francis M Pipkin, and James C Baird. Hyperfine Structure of Hydrogen, Deuterium, and Tritium. *Phys. Rev.*, 120(4):1279–1289, 11 1960.

[217] Kyoungsuk Jin, Joseph H Maalouf, Nikifar Lazouski, Nathan Corbin, Dengtao Yang, and Karthish Manthiram. Epoxidation of Cyclooctene Using Water as the Oxygen Atom Source at Manganese Oxide Electrocatalysts. *Journal of the American Chemical Society*, 141(15):6413–6418, 4 2019.

[218] Hannah J Hogben, Olga Efimova, Nicola Wagner-Rundell, Christiane R Timmel, and P J Hore. Possible involvement of superoxide and dioxygen with cryptochrome in avian magnetoreception: Origin of Zeeman resonances observed by in vivo EPR spectroscopy. *Chemical Physics Letters*, 480(1):118–122, 2009.

[219] Ilia A Solov'yov and Klaus Schulten. Magnetoreception through Cryptochrome May Involve Superoxide. *Biophysical Journal*, 96(12):4804–4813, 2009.

[220] Min-hua Shao, Ping Liu, and Radoslav R Adzic. Superoxide Anion is the Intermediate in the Oxygen Reduction Reaction on Platinum Electrodes. *Journal of the American Chemical Society*, 128(23):7408–7409, 6 2006.

[221] Jimin Park, Ping Du, Jin-Kyung Jeon, Gun Hyuk Jang, Mintai Peter Hwang, Hyung-Seop Han, Kwideok Park, Kwan Hyi Lee, Jee-Wook Lee, Hojeong Jeon, Yu-Chan Kim, Jong Woong Park, Hyun-Kwang Seok, and Myoung-Ryul Ok. Magnesium Corrosion Triggered Spontaneous Generation of H2O2 on Oxidized Titanium for Promoting Angiogenesis. *Angewandte Chemie International Edition*, 54(49):14753–14757, 2015.

[222] Jimin Park, Hyunseon Seo, Hae Won Hwang, Jonghoon Choi, Kyeongsoo Kim, Goeen Jeong, Eun Shil Kim, Hyung-Seop Han, Yeon-Wook Jung, Youngmin Seo, Hojeong Jeon, Hyun-Kwang Seok, Yu-Chan Kim, and Myoung-Ryul Ok. Interface Engineering of Fully Metallic Stents Enabling Controllable H2O2 Generation for Antirestenosis. *Langmuir*, 35(10):3634–3642, 3 2019.

[223] Jimin Park, Gun Hyuk Jang, Yeon Wook Jung, Hyunseon Seo, Hyung-Seop Han, Joonho Lee, Youngmin Seo, Hojeong Jeon, Myoung-Ryul Ok, Pil-Ryung Cha, Hyun-Kwang Seok, Kwan Hyi Lee, and Yu-Chan Kim. Tailoring H2O2 generation kinetics with magnesium alloys for efficient disinfection on titanium surface. *Scientific Reports*, 10(1):6536, 2020.

[224] Thomas C Player and P J Hore. Viability of superoxide-containing radical pairs as magnetoreceptors. *The Journal of Chemical Physics*, 151(22):225101, 2019.

[225] Marta E Alberto, Nino Russo, Andre Grand, and Annia Galano. A physicochemical examination of the free radical scavenging activity of Trolox: mechanism{,} kinetics and influence of the environment. *Phys. Chem. Chem. Phys.*, 15(13):4642–4650, 2013.

[226] Jakub Adam Koza, Margitta Uhlemann, Annett Gebert, and Ludwig Schultz. Desorption of hydrogen from the electrode surface under influence of an external magnetic field. *Electrochemistry Communications*, 10(9):1330–1333, 2008.

[227] C Cierpka, T Weier, G Gerbeth, M Uhlemann, and K Eckert. Copper deposition and dissolution in seemingly parallel electric and magnetic fields: Lorentz force distributions and flow configurations. *Journal of Solid State Electrochemistry*, 11(6):687–701, 2007.

[228] Jakub Adam Koza, Margitta Uhlemann, Annett Gebert, and Ludwig Schultz. The effect of magnetic fields on the electrodeposition of CoFe alloys. *Electrochimica Acta*, 53(16):5344–5353, 2008.

[229] Tata N Rao, I Yagi, T Miwa, D A Tryk, and A Fujishima. Electrochemical Oxidation of NADH at Highly Boron-Doped Diamond Electrodes. *Analytical Chemistry*, 71(13):2506–2511, 7 1999.

[230] Pantelis Karabinas and Dimitrios Jannakoudakis. Kinetic parameters and mechanism of the electrochemical oxidation of L-ascorbic acid on platinum electrodes in acid solutions. *Journal of Electroanalytical Chemistry and Interfacial Electrochemistry*, 160(1):159–167, 1984.

[231] Bo Barker Jørgensen, Alyssa J Findlay, and André Pellerin. The Biogeochemical Sulfur Cycle of Marine Sediments. *Frontiers in Microbiology*, 10:849, 2019.

[232] Andrew W Munro, Michael A Noble, Laura Robledo, Simon N Daff, and Stephen K Chapman. Determination of the Redox Properties of Human NADPH-Cytochrome P450 Reductase. *Biochemistry*, 40(7):1956–1963, 2 2001.

[233] Kenji Kono. Thermosensitive polymer-modified liposomes. *Advanced Drug Delivery Reviews*, 53(3):307–319, 2001.

[234] Milton B Yatvin, John N Weinstein, Warren H Dennis, and Robert Blumenthal. Design of Liposomes for Enhanced Local Release of Drugs by Hyperthermia. *Science*, 202(4374):1290–1293, 1978.

[235] Lin-Ai Tai, Pi-Ju Tsai, Yu-Chao Wang, Yu-Jing Wang, Leu-Wei Lo, and Chung-Shi Yang. Thermosensitive liposomes entrapping iron oxide nanoparticles for controllable drug release. *Nanotechnology*, 20(13):135101, 3 2009.

[236] Junsang Moon, Michael G Christiansen, Siyuan Rao, Colin Marcus, David C Bono, Dekel Rosenfeld, Danijela Gregurec, Georgios Varnavides, Po-Han Chiang, Seongjun Park, and Polina Anikeeva. Magnetothermal Multiplexing for Selective Remote Control of Cell Signaling. *Advanced Functional Materials*, n/a(n/a):2000577.

[237] Danijela Gregurec, Alexander W Senko, Andrey Chuvilin, Pooja D Reddy, Ashwin Sankararaman, Dekel Rosenfeld, Po-Han Chiang, Francisco Garcia, Ian Tafel, Georgios Varnavides, Eugenia Ciocan, and Polina Anikeeva. Magnetic Vortex Nanodiscs Enable Remote Magnetomechanical Neural Stimulation. *ACS Nano*, 14(7):8036–8045, 7 2020.

[238] Amanda Singer, Shayok Dutta, Eric Lewis, Ziying Chen, Joshua C Chen, Nishant Verma, Benjamin Avants, Ariel K Feldman, John O'Malley, Michael Beierlein, Caleb Kemere, and Jacob T Robinson. Magnetoelectric Materials for Miniature, Wireless Neural Stimulation at Therapeutic Frequencies. *Neuron*, 107(4):631–643, 2020.

[239] Vijay Shah, Greg Lyford, Greg Gores, and Gianrico Farrugia. Nitric oxide in gastrointestinal health and disease. *Gastroenterology*, 126(3):903–913, 2004.

[240] Matthew W Coryell, Adam E Ziemann, Patricia J Westmoreland, Jill M Haenfler, Zlatan Kurjakovic, Xiang-ming Zha, Margaret Price, Mikael K Schnizler, and John A Wemmie. Targeting ASIC1a Reduces Innate Fear and Alters Neuronal Activity in the Fear Circuit. *Biological Psychiatry*, 62(10):1140–1148, 2007.

[241] Bradley A Webb, Michael Chimenti, Matthew P Jacobson, and Diane L Barber. Dysregulated pH: a perfect storm for cancer progression. *Nature Reviews Cancer*, 11(9):671–677, 2011.